Synthesis of Janus Nanoparticles using a Packed Column and their Applications

by

Alan Michael Hanley

A Dissertation submitted to the Graduate Faculty of
Auburn University
in partial fulfillment of the
requirements for the Degree of
Doctor of Philosophy

Auburn, Alabama
August 4, 2018

Keywords: Janus nanoparticles, nanoparticle synthesis, emulsion

Approved by

Allan E. David, John W. Brown Assistant Professor of Chemical Engineering
W. Robert Ashurst, Uthlaut Family Associate Professor of Chemical Engineering
James Radich, Assistant Professor of Chemical Engineering
Robert D. Arnold, Associate Professor of Drug Discovery and Development

Abstract

Janus nanoparticles, nanoparticles with two regions of differing properties, have been of interest to researchers for the last 30 years. Differing surface regions of Janus nanoparticles allows for self-assembly into larger structures, giving these nanoparticles potential applications in coatings, targeted drug delivery, and emulsion stability to name a few. Three main challenges exist when developing Janus nanoparticles: size control, scalability of the synthesis method, and versatility of the method. Versatility refers to the ability to make different Janus nanoparticles without changing the synthesis method. Even with increased interest into Janus nanoparticles, synthesis methods that overcome all three challenges are scarce. Considering the large number of possible applications, it is crucial that new synthesis methods are developed that can overcome these challenges.

In this work, a novel synthesis method was presented that produces Janus nanoparticles in a packed column. Nanoparticles were masked onto the column's packing material and selectively modified with different compounds to developed dual-sided nanoparticles. This method allowed development of multiple anisotropic Janus nanoparticle configurations without making changes to the synthesis method or equipment. Nanoparticles were characterized using dynamic light scattering, Fourier-transform infrared spectroscopy, and fluorescent spectroscopy. Fluorescent optical microscopy and transmission electron microscopy were utilized to visualize these nanoparticles and confirmed the existence of two different surface modifications based on the location of different fluorescent dyes or location of nanostructures of varied size..

Self-assembling abilities and potential applications for Janus nanoparticles were also examined. The effect of Janus nanoparticles on interfacial tension of an immiscible fluid interface was investigated, and self-assembled monolayers of Janus nanoparticles were formed on hydrophobic surfaces and examined using optical microscopy. Results showed that Janus nanoparticles reduced interfacial tension between immiscible fluids and uniformly assembled on hydrophobic surfaces, further confirming the creation of two-sided nanoparticles. With regards to potential applications, investigation into the use of Janus nanoparticles for improved emulsion

stability and pore size control was done using liquid-liquid and liquid-gas interfaces. Finally, stationary phase surface area was increased to determine if this method can produce larger quantities of Janus nanoparticles as the first step to determining scalability. Initial results from scaled-up packed column synthesis runs looked promising and indicated that the packed column method has the potential to be scaled-up to produce nanoparticles at industrial level quantities.

Acknowledgments

First and foremost, I need to thank all of my family members for their love and constant support during my graduate school career. To my parents, Tom and Norma, my siblings, Jeff, Drew, and Caitlin, and my sister-in-law Chandra, you are the most important people in the world to me, and I could not have done this without you. The five years I've spent on this project have had many ups and downs, and I will forever appreciate how you all helped me celebrate the highs and ride out the lows.

This work would not have been possible without the guidance of my advisor, Dr. Allan E. David. Thank you for taking a chance on me and giving me control of a project that is clearly important to you, as well as helping me every step of the way. Thank you to all the members of the David Lab: past members Dr. Young Suk Choi, Dr. Alex Kelly, Hunter Rogers, and Chelsea Harris, and present members Dr. Tareq Anani, Dr. Xin Fan, Dr. Barry Yeh, Dr. Prachi Sangle, Richard Cullum, Ricky Whitener, Marjan Azadi, Braden Hahn, Nayer Sultana, and our horde of undergrads. Special recognition needs to be given to Dr. Young Suk Choi, for constantly donating her time to help me with my work despite her busy schedule.

To all my friends: Auburn Chem E OG, the Louisville Crew, the Trinity in New York and Fort Lauderdale, and everyone else, I could not have chosen a better group of people. Thank you for your friendship and your support.

Special recognition needs to be given to Dr. Michael E. Miller, who educated me on the operation of the Transmission Electron Microscope, as well as Dr. Vitaly Vodyanoy and Oleg

Pustovyy, who examined my samples using their advanced optical microscope. The images yielded from these techniques were invaluable to my research.

I would like to thank the Chemical Engineering Department at the University of Louisville where I got my start, specifically Dr. Gerold Willing, who advised my research during my time at Louisville. Without the foundation that you helped me build, I would not be where I am today.

Finally, I would like to thank the Chemical Engineering Department here at Auburn University. You have cultivated a much stronger and more capable engineer than I ever thought I could become, and any success I achieve in the future can undoubtedly be linked to the effort you put into me.

Table of Contents

List of Figures

List of Tables

Chapter 1: Introduction to Nanoparticles and Janus Nanoparticles

1.1: Nanoparticles and Nanotechnology

Researchers have been investigating nanotechnology since the 1970's.[1] One area of nanotechnology investigates nanoparticles, including synthesis of nano-scale materials, examination of nanoparticle properties, and characterization of nanoparticle assemblies.[2,3] The most attractive property of nanoparticles is there high surface area-volume ratio.[4,5] Due to the high ratio, nanoparticles have more atoms positioned on the surface making them more reactive than bulk scale materials.[6–10] Interest in nanoparticles and nanotechnology is still growing, as shown by an increase in grants for nano-scale research and publications involving nanotechnology (see Figure 1.1):

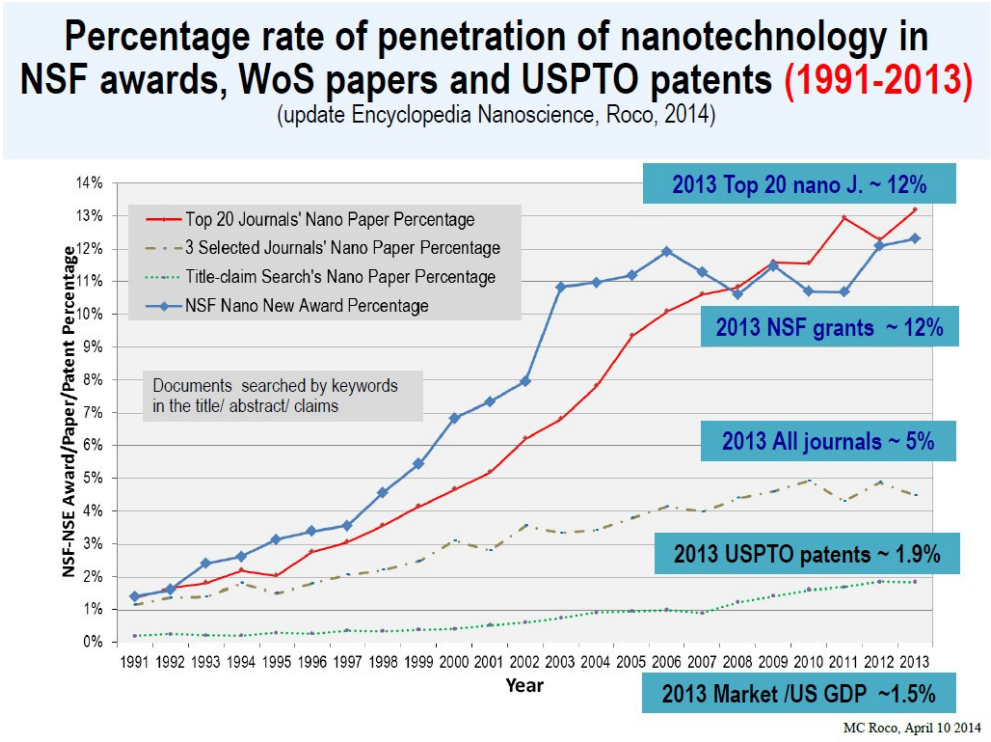

Figure 1.1: Trends since 1990 for nanotechnological research in top 20 journals (red), selected journal papers (gray), other papers (green), and NSF grant awards (blue)[11]

Nanoparticles and nanomaterials have already been utilized in numerous applications including consumer products and construction materials.[12] Titanium oxide and/or zinc oxide nanoparticles are added to sunscreen to improve protection from UVA rays.[13] Carbon nanotubes are utilized to produce composite materials for the construction of airplanes, wind turbines, and numerous consumer products.[14–16] Successful application of nanomaterials has led to research into more advanced nanomaterial applications, including but not limited to targeted drug delivery vehicles capable of delivery multiple drugs, protective coatings resistant to water molecules and/or bacteria cells, and nanoelectronics devices to increase computer processing power and improve memory storage devices.[17–21] With these application in mind, a sector of nanomaterials research has developed to investigate the synthesis of "smarter" nanomaterials with controllable and tunable properties.

1.2: Janus Nanoparticles

Anisotropic nanoparticles called "Janus" nanoparticles (JNPs) have been investigated for over 30 years.[22] Named for the two-faced Roman god Janus, JNPs consist of two or more differing surface regions which results in unique properties, most notably the ability to self-assemble.[23] Driven by the energy of the system[24], self-assembly has been investigated using numerous materials, such as the assembly of organothiols onto gold nanoparticles[25], assembly of surfactant like peptides in selected solvents[26], and the assembly of nanoparticles by means of hydrogen bonding[27]. Researchers have further investigated this phenomenon by examining the parameters that govern self-assembly, tuning them to control the spacing and size of the assembled structures.[28] By altering the structure and/or surface regions of JNPs, assemblies including spherical micelles, cylindrical micelles, inverted micelles, liposomes, flexible monolayers, and planar monolayers can be created.[18,24] This point is illustrated in Figure 1.2:

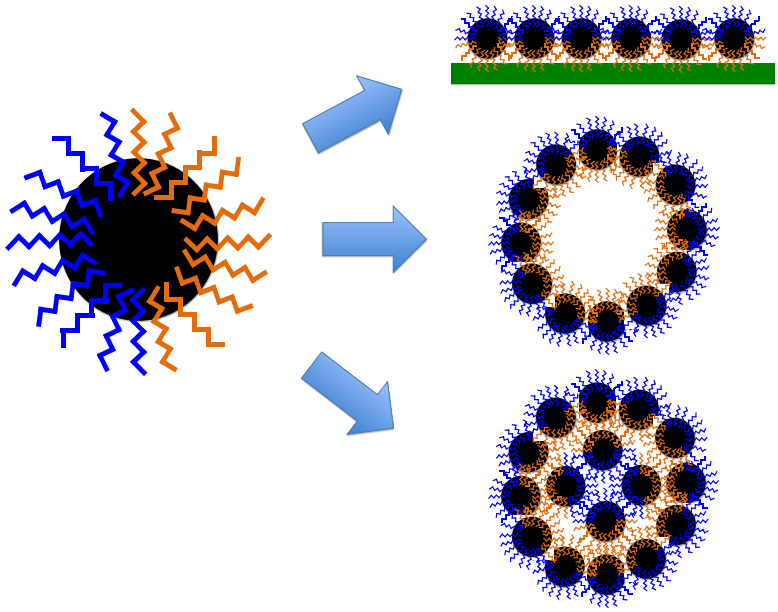

Figure 1.2 Illustration of JNPs and self-assembled structures. The core nanoparticle is represented in black; the surface compounds in blue and orange. Different compounds are attached to opposing sides of the nanoparticle creating an anisotropic JNP.

Possible applications for JNPs include but are not limited to protective coatings, drug delivery vehicles, and emulsion stabilizers.[18] Water resistant coatings for fabrics have been formed using JNPs with regions of hydrophobicity and opposing regions that bond to textiles.[29] Antimicrobial coatings have been developed using partially metallic Janus nanorods composed of iron oxide or silver.[30] Drug delivery vehicles to target cancer cells and concurrently release drug payloads have been designed on JNP platforms; some of the vehicles can carry multiple drugs due to their two-sided strucutre.[20,31,32] JNPs have also been shown to control droplet size in emulsions and improve emulsion stability.[33,34] Outside of these applications, JNPs have been utilized as bio-recognition signaling devices, improved catalyst materials, and ultra-thin display screens.[35–37]

There are numerous challenges with JNPs research; the most notable are controlling the size range of JNPs, total JNP yield, and producing versatile synthesis methods. For example, a "perfect" JNP synthesis method will produce large quantities of monodispersed JNPs; this method would also allow for changes to the JNP materials (nanoparticles, surface coatings, etc.) without major changes to the method; this allows for synthesis of multiple JNP configurations for different

applications from one method. Due to the relative infancy of this field, most published literature does not address all three challenges; most current publications focus on a proof-of-concept method and a potential application.

1.3: Synthesis Methods for Janus Nanoparticles

1.3.1: Masking Method

The masking method was one of the first strategies utilized to produce JNPs.[19] Previously, this method was used to produce anisotropic particles above the nanoscale; the same methodology was used to developed nanoscale particles.[38] JNPs are creating by modifying one hemisphere/region of a nanoparticle surface while preventing that modification on the opposing hemisphere/region. Opposing regions are separated by suspending nanoparticles at phase interfaces or between immiscible liquids.[39,40] This allows for size control of the final JNPs and overcomes one of the three mains challenges.

There are two popular strategies for solid-liquid masking in published literature: flat plate masking and spherical masking. Sardar et al. were able to produce JNPs by masking nanoparticles on a flat plate in 2007. A silanized glass surface was used to stabilize gold nanoparticles so they could be partially reacted with 11-mercapto-1-undecanol, a hydrocarbon chain with a reactive thiol group. Sonicating the plate in a solution of either 16-mercaptohexadecanoic or mercaptoethylamine released the nanoparticles from the slide and allowed the unmodified side to reacted with different molecules.[41] Figure 2.1 (a) shows an illustration of Sardar et al.'s synthesis process. This method produced 2 monodispersed samples of JNPs with different configurations; it is possible that additional JNP configurations could have been prepared using this method. However, preparing large quantities of JNPs using flat plate masking requires large volume reactors and makes scalability more challenging (total JNP yield is not discussed in this publication).

Spherical masking was achieved by Li et al. in 2013 by masking 15 nm silica nanoparticles around 500 nm silica nanoparticles in a liquid suspension.[42] Li's research group used a copper mediated click reaction[43] to produce JNPs with a polymer region.[42] While the compounds are different from the previously discussed flat-plate masking method , the order of actions is the same;

mask nanoparticles onto a functionalized surface, attach a compound to the exposed nanoparticle surface, and sonicate to release. Figure 1.3 (b) shows an illustration of Li et al.'s process. Masking again produces monodispersed JNPs; usage of a spherical masking surface increases the ratio JNP production area to total reactor volume when compared to flat-plate masking (note that total JNP yield is not addressed in this publication). However, only one JNP configuration is discussed and the method relies on the copper mediated click reaction to attach nanoparticles to the masking surface. This is another example of a publication that overcomes only two main challenges with JNP production.

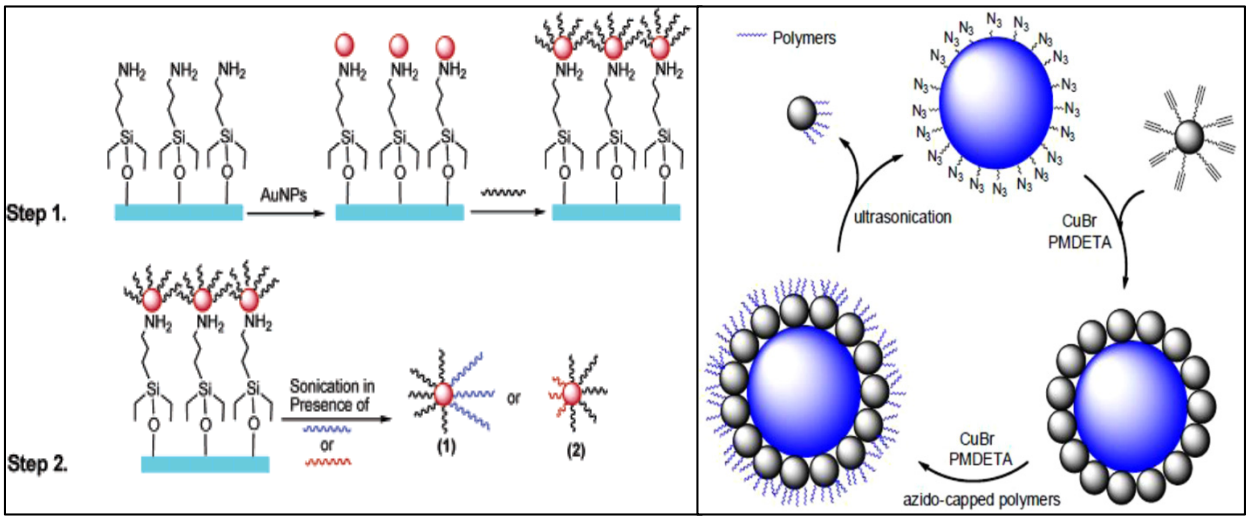

Figure 1.3 (a) Illustration of flat plate masking method used by Sardar et al.[41] (Reprinted with permission from Sardar et al. Copyright 2007, American Chemical Society.) (b) Illustration of spherical masking method used by Li et al.[42] (Reprinted with permission from J. Li et al. Copyright 2013, American Chemical Society.)

Researchers have also used wax-in-water emulsions as a medium for synthesizing JNPs. Nanoparticles are used to stabilize emulsions[44]; once the wax solidifies, regions of the nanoparticles are selectively modified. Perro et al used this strategy to produce silica JNPs[45]; Figure 1.4 shows an illustration of this process. Silica nanoparticles ranging in size from 100-800 nm in diameter were masked onto wax droplets and selectively modified with aminopropyltriethoxysilane.[45] Large quantities of JNPs were yielded (roughly 0.5 grams/batch)

and the publication reports that their method could be scaled-up to meet an industrial demand.[45] This method also has potential to produce multiple JNP configurations; if nanoparticles can be absorbed onto wax droplets, surface compounds are interchangeable if the reaction chemistry is consistent. The publication discusses two configurations, both using a silica nanoparticle, but it can be inferred that other nanoparticles could be utilized. Perro's work is a rare example of a JNP method that addresses all three major challenges.

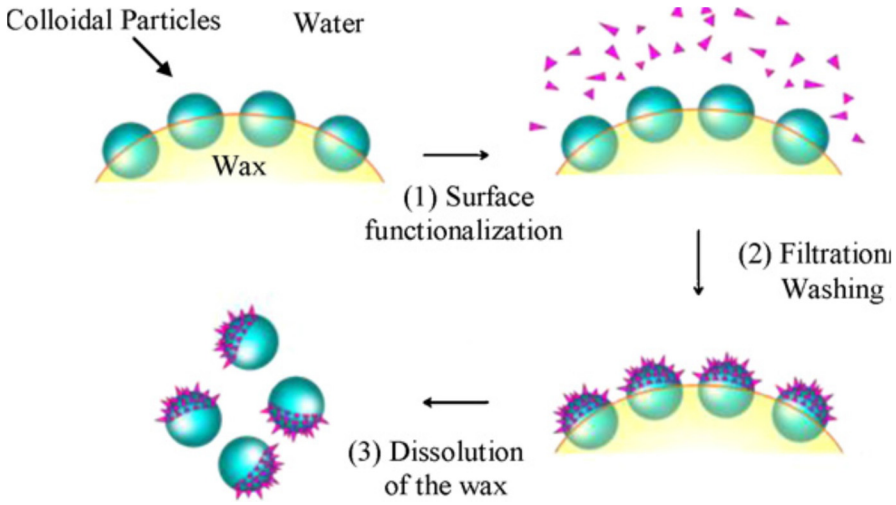

Figure 1.4 Illustration of wax-in-water masking method used by Perro et al.[45] Reprinted with permission from Perro et al. Copyright 2009, Elsevier.

Gu et al. were able to create JNPs via liquid-liquid masking by partially coating iron oxide nanoparticles with silver nanoparticles using an emulsion. Iron oxide nanoparticles in the presence of aqueous and organic solvents were sonicated to create an emulsion; iron oxide nanoparticles assembled around microdroplets of organic solvent, exposing a region for silver nanoparticles to form a covalent bond.[46] An illustration of this process is shown in Figure 1.5. A similar process was done by Glaser et al to create iron oxide JNPs with a partial coating of gold nanoparticles.[47] Again, JNPs of controlled size are synthesized due to the nature of the masking method. While Perro's work showed that emulsified environments have potential scalability and can produce different JNP configurations, neither of these challenges are addressed in Gu or Glaser's publications.

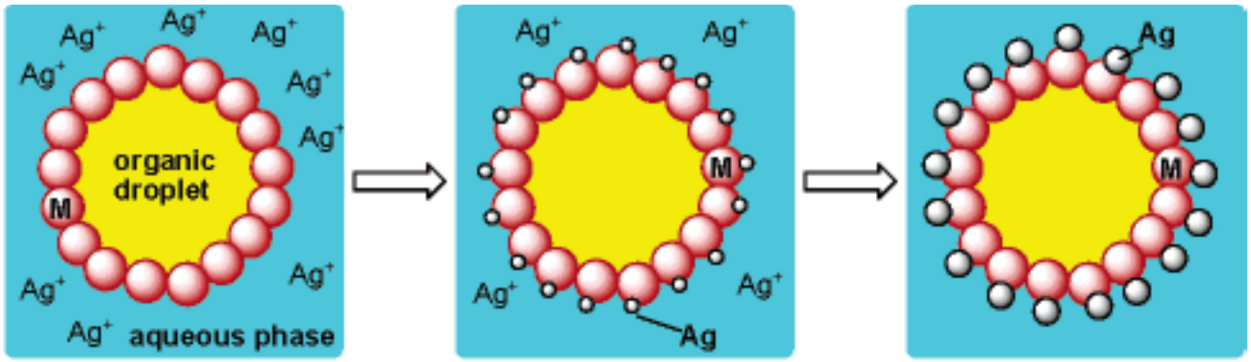

Figure 1.5: Illustration of synthesis method for iron oxide core JNP with a partial gold coating at the liquid-liquid interface. Adapted with permission from Gu et al. Copyright 2005, American Chemical Society

Finally, synthesis of JNPs at the gas-liquid interface was achieved by Pradhan et al.[40] Using a Langmuir-Blodgett trough[48], Pradhan et al formed a monolayer of functionalized gold nanoparticles at the air-water interface. At high surface pressure, ligand intercalation between the nanoparticles significantly limited nanoparticle mobility; this allowed for functionalization of nanoparticle regions in the liquid phase.[40] While successful, this publication only addresses one of the challenges (size control) of JNP synthesis. Figure 1.6 shows an illustration of this process:

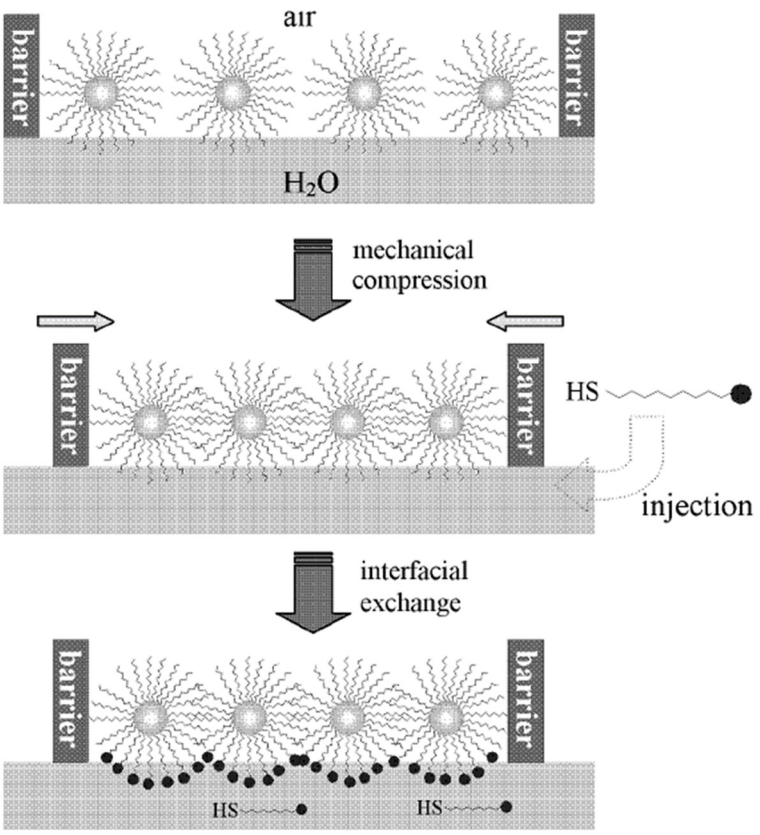

Figure 1.6 Illustration of JNPs formed at the gas-liquid interface by Pradhan et.al.[40] Reprinted with the permission of Pradhan et al., 2007, with the permission of John Wiley and Sons, Inc.

1.3.2: Block-Copolymers

Block co-polymers can be used to produce JNPs by controlled assembly of polymer chains.[19] Both triblock copolymers of ABC design (three different monomers)[49] and diblock copolymers (two different monomers) have been utilized to create JNPs[50]. Self-assembly of block co-polymers into JNPs can be achieved by controlling the monomer weight ratios, temperature, pH, solvents, and other factors.[19,51] Erhardt et al. created JNPs from the triblock copolymer polystyrene-b-polybutadiene-b-poly(methyl methacrylate).[52] The block copolymers were assembled into a bulk phase by solution casting; this process created compact regions of polybutadiene within the cast. The cast was then crosslinked causing the polybutadiene chains to bond, then finally dissolved in a solvent to release the particles.[52] An illustration of this procedure is shown in Figure 1.7:

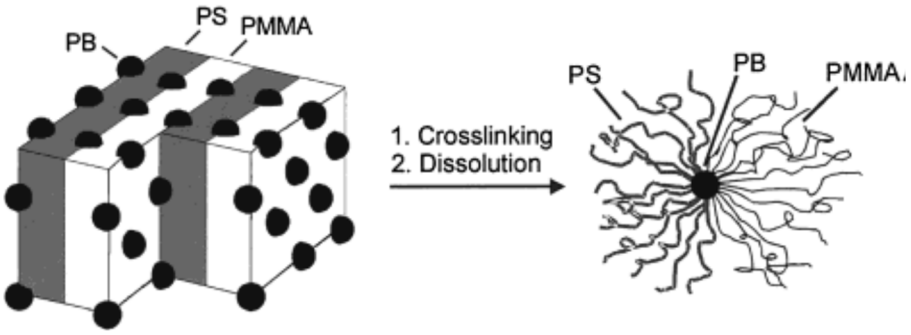

Figure 1.7 Illustration of JNPs formed from triblock copolymers by Erhardt et al.[52] Reprinted with permission from Erhardt et al. Copyright 2001, American Chemical Society.

Poggi et al synthesized JNPs using a thin film composed of diblock copolymers. Polystyrene-b-poly(4-vinylpyridine) was formed into a 20-50 nm thin film. Forming of the film caused an organized assembly of the polymers with exposed regions of poly(4-vinylpyridine) (Figure 1.8, top left). Using a two-step reaction, poly(4-vinylpyridine) molecules were crosslinked and then bonded to polyethylene glycol (PEG). Upon dissolving the film, poly(4-vinylpyridine) core nanoparticles with regions of PEG and polystyrene were developed; JNPs had a hydrodynamic diameter of 55 nm.[50] An illustration of this process is shown in Figure 1.8:

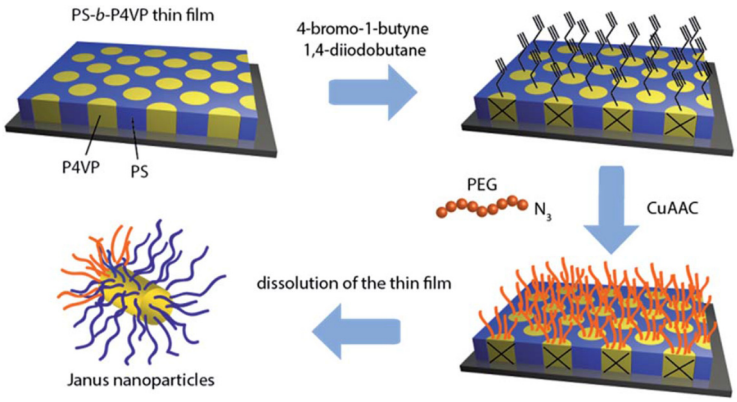

Figure 1.8: Illustration of synthesis method for JNPs using a thin film composed of diblock copolymers and PEG. Reproduced from Poggi et al. with permission from The Royal Society of Chemistry.

Fu et al. produced JNP composed of titania and gold using a diblock copolymer as a stabilizer. This method is a combination of the masking method and the block co-polymer method: while co-polymers are utilized, they are not part of the final JNP structure. Polystyrene-b-poly(ethylene oxide) was used to stabilize chloroauric acid in a micelle. Titania sol-gel precursor was added to bond to the exposed areas of chloroauric acid and the mixture was formed into a thin film. Dried films were exposed to UV light, reducing the chloroauric acid to gold and removing the polymers; JNPs with diameters ranging from 12-22 nm were produced.[53] An illustration of this strategy is shown in Figure 1.9:

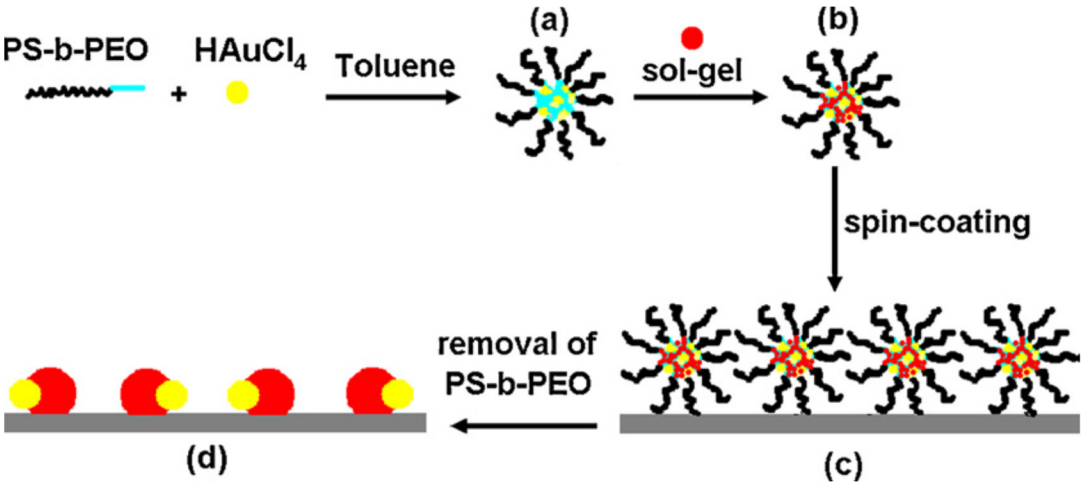

Figure 1.9 Illustration of formation of gold/titania Janus nanostructures using micelles stabilized by diblock copolymer. Reprinted with permission from Fu et al., 2011, with permission from Elsevier.

From the work presented in this section, block-copolymers can be used to produce monodispersed JNPs. However, due to the need for block-copolymers with well understood geometry, versatility of JNP configurations is limited when compared to the masking method. Scalability of these methods is not addressed in the aforementioned publications, indicating that block-copolymer methods are inferior to masking methods when attempting to overcome this challenge.

1.3.3: Phase Separation

The phase separation method involves combining two or more incompatible components into one nanostructure; once forced together, the components will separate and form an anisotropic nanoparticle. This method is utilized when working with inorganic materials, nanocrystals, and polymers (polymers are the most popular in literature).[18,54] Phase separation is commonly done in an emulsified environment or by co-jetting of incompatible compounds, but not limited to these methods.[18,19] Saito et al. were able to synthesize JNPs composed of polystyrene (PS) and poly(methyl methacrylate) (PMMA) using phase separation in an emulsified environment. After preparing a water-toluene emulsion with both polymers, the toluene was removed by evaporation, forcing the development of side-segregated nanoparticles of PS and PMMA. The research team concluded that the type/concentration of surfactant used in the emulsion determined the final structure of the JNPs.[55] Figure 1.10 shows some of the developed structures depending on the surfactant concentration.

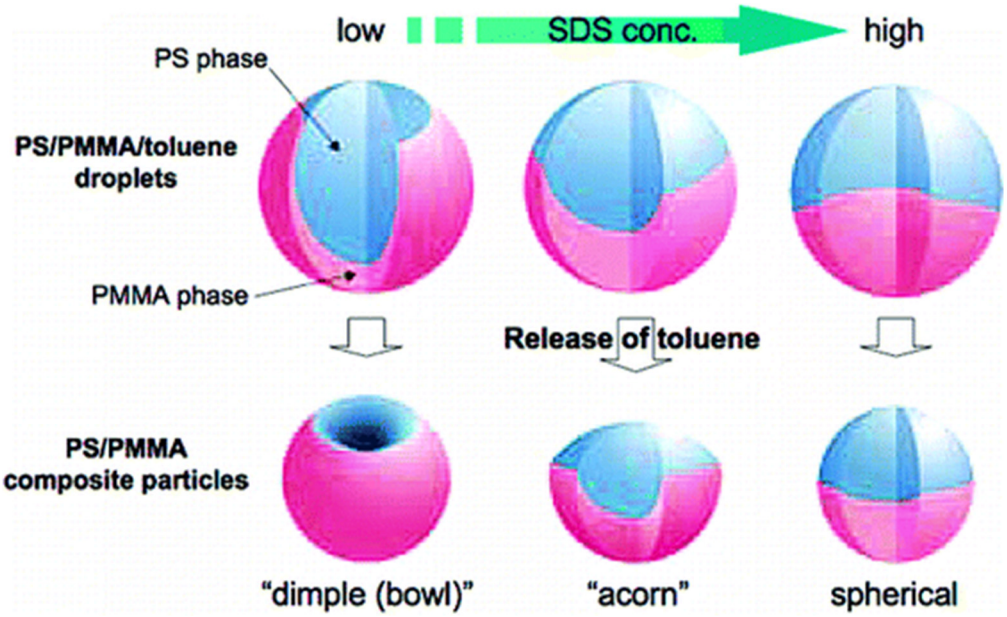

Figure 1.10 Illustrations of structures developed by Saito et al. as the concentration of surfactant was altered in emulsions. The image on the far right shows the final spherical JNP structure.[55] Reprinted with the permission of Saito et al. Copyright 2006, American Chemical Society.

Co-jetting involves the flow of two or more immiscible polymeric fluids through a small nozzle.[56] In electrohydrodynamic co-jetting, an electric field is applied to the fluids after exiting the nozzle forming a thin thread of mixed fluid (Taylor cone).[57] The thread breaks into droplets and the solvent readily evaporates, yielding two-sided polymeric nanoparticles.[56,58] Figure 1.11 shows an illustration and photograph of an electrohydrodynamic co-jetting system and confocal microscope images of the resulting JNPs. Co-jetting has also been shown to create JNPs by using sheer force of a flowing liquid instead of an electric field. Xie et al. developed a co-jetting apparatus that combined immiscible fluids into a flowing solvent stream containing surfactant compounds.[20] The sheer force from the stream on the surfactant material forced the immiscible liquids into nano-droplets which solidify into JNPs due to nanoprecipitation.[20,59,60] JNPs with hydrodynamic diameters averaging 305 nm were produced; the author notes that this process is potentially scalable.[20] An illustration of the apparatus used by Xie et al. is shown in Figure 1.12:

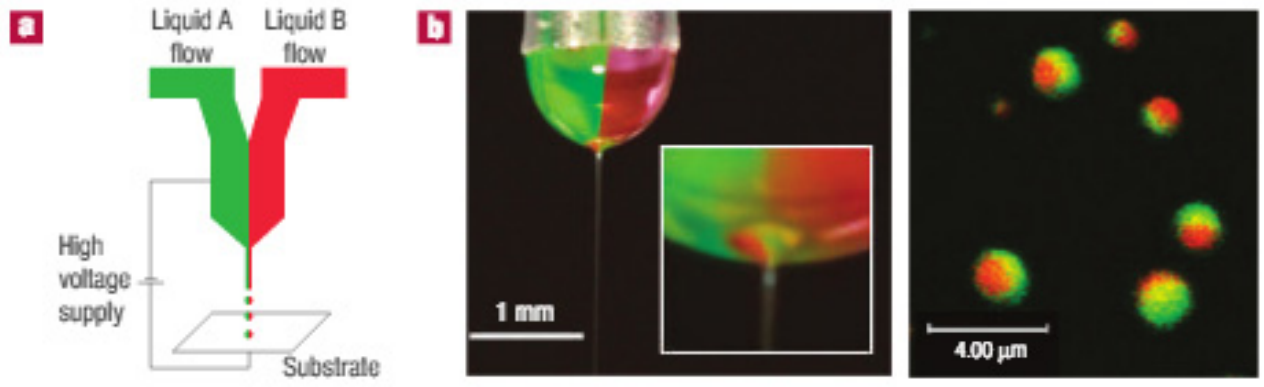

Figure 1.11 (from left to right): Illustration of an electrohydrodynamic co-jetting system; photograph of an electrohydrodynamic co-jetting system; Confocal microscope images of JNPs synthesized via electrohydrodynamic co-jetting[56]. Reprinted with permission from Xie et al. Copyright 2012, American Chemical Society.

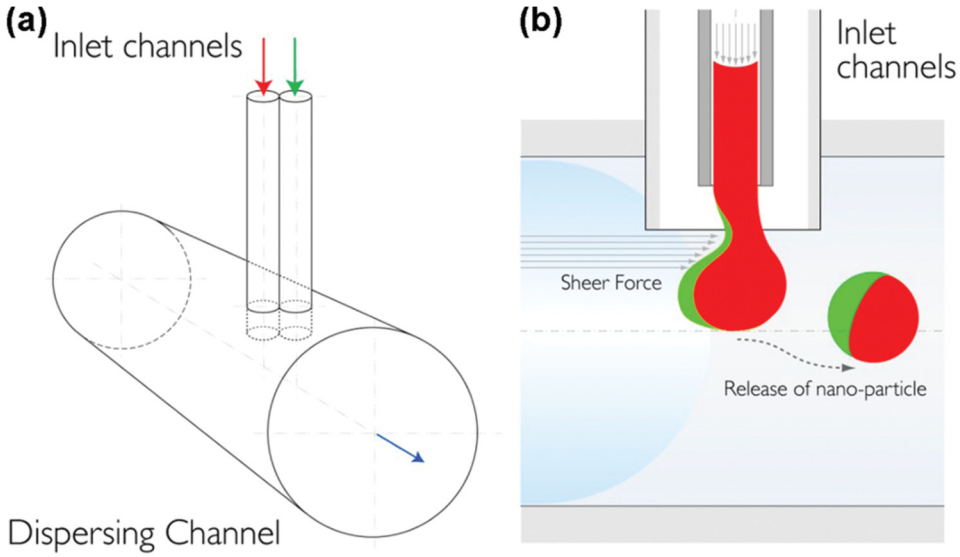

Figure 1.12 Illustration of the co-jetting apparatus used by Xie et al. that utilized a flowing dispersing channel.[20] Reprinted with permission from Xie et al. Copyright 2012, American Chemical Society.

Additional phase separation methods include flame synthesis[61] and one-pot synthesis[62]. Gu et al were able to synthesize JNPs consisting of cadmium sulfide (CdS) and iron-platinum (FePt) nanoparticles via a one-pot synthesis.[62] FePt nanoparticles were coated with sulfur and reacted with additional compounds to create a shell-core structure of CdS (shell) and FePt (core). When the temperature was increased to 280°C, CdS transitioned from amorphous to a crystalline state and experienced dewetting (removal of a thin liquid film around the substrate[63]), which led to the formation of a FePt-CdS heterodimers.[62] Figure 1.13 shows and illustration of this process:

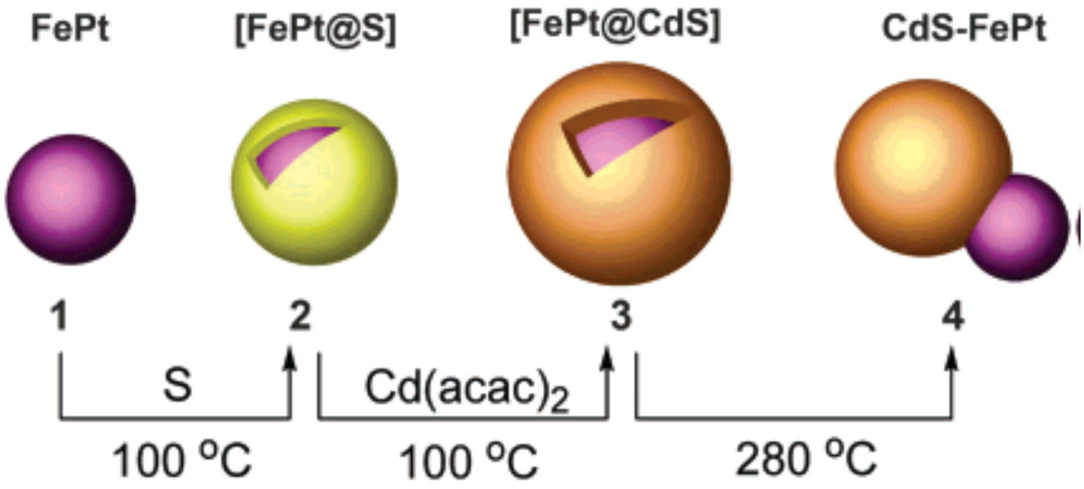

Figure 1.13 Illustration of the process used by Gu et al. to create JNPs using a one-pot synthesis method.[62] Reprinted with permission from Gu et al. Copyright 2004, American Chemical Society.

While JNPs produced by phase-separation methods show size control and the potential for scalability, few publications address all three of the major challenges with JNP production. To the best of the author's knowledge, Perro et al. has prepared the only publication that addresses all three challenges. From this review, further investigation into versatile and scalable JNP synthesis methods needs to be conducted.

Chapter 2: Producing Iron Oxide JNPs using Spherical Masking in a Packed Column

2.1: Introduction

2.1.1 Packed Column Method

The packed column synthesis method uses stationary phase materials from a chromatography column as a reactive surface (or masking surface) for JNP production. Two different hydrophobic stationary phases were used for this project: silica particles with diameters between 62-70 μm (further referred to as "C_{18} particles"), and borosilicate glass beads with diameters between 900-1100 μm (further referenced as "C_{18} beads"). Both materials have hydrophobic surface coatings of octadecatrimethoxysilane. Columns with C_{18} particles and C_{18} beads are shown in Figure 2.1, and an illustration of the surface of the C_{18} particles and/or C_{18} beads is shown in Figure 2.2:

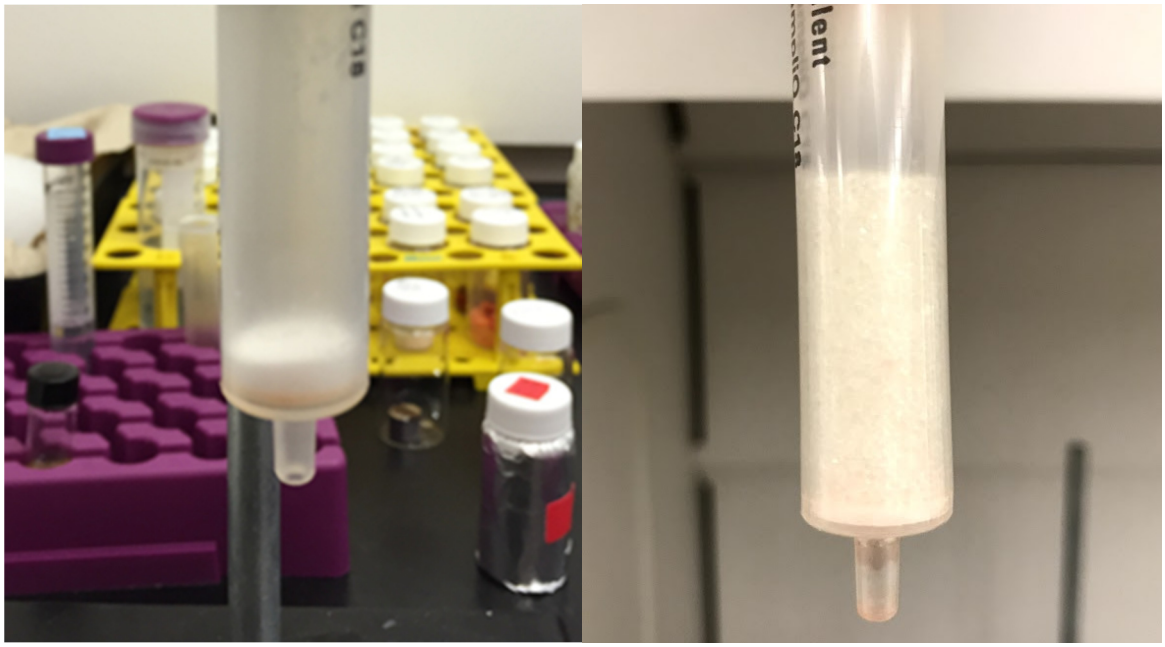

Figure 2.1: Photos of columns containing C_{18} particles (left) and C_{18} beads (right)

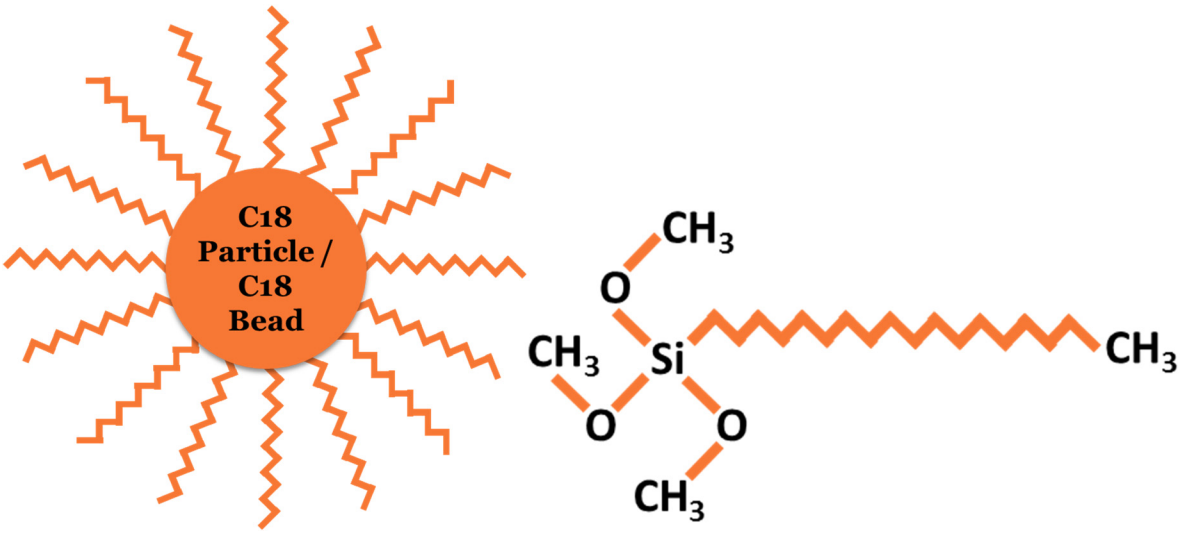

Figure 2.2: Illustration of C_{18} particles and/or C_{18} beads surface (left). The core material is coated with octadecatrimethoxysilane (right), which bonds to the particle/bead surface via its silane head group

JNP synthesis begins by coating the stationary phase with molecules (M1) containing a hydrophobic tail. M1 molecules adsorb to the stationary phase, aligning their hydrophobic tail groups with the hydrophobic tail groups of octadecatrimethoxysilane. M1 must also contain a reactive headgroup to bond to a nanoparticle surface; for our experiments, amphiphilic aminated molecules oleylamine ($C_{18}H_{37}N$) and stearylamine ($C_{18}H_{39}N$) were utilized. Amine reaction chemistry is well studied and amines react with numerous functional groups including aldehydes and ketones.[64,65] Intermolecular forces between hydrocarbon chains stabilize M1 molecules on the stationary phase surface and exposed reactive head groups; M1 will be the first surface coating for the JNPs. Excess M1 molecules are washed from the column before the next synthesis step; this prevents M1 molecules from bonding top the opposing side of the nanoparticles. Additional information on the interaction between the stationary phase and the M1 compounds can be found in Section 2.1.2.

The second stes to this synthesis method reacts the M1 headgroups to a nanoparticle surface. Due to the size difference between the stationary phase material and the nanoparticles (between 200x – 55,000x larger depending on stationary phase material and nanoparticle size), the geometry of the stationary phase is essentially a flat surface with respect to a single nanoparticle.

This leads to only one side of the nanoparticle reacting with the exposed M1 molecules. After washing unreacted nanoparticles from the column, nanoparticles are stabilized on the stationary phase surface by the adsorbed M1 molecules. The final step involves reacting a second compound (M2) to the exposed nanoparticle region (region that faces away from the stationary phase surface). A solvent in which both M1 and M2 molecules are soluble is passed through the column to release the finished JNPs. Figure 2.3 shows an illustration of this synthesis using a carboxyl coated nanoparticle, an aminated M1 compound, and a M2 molecule of aminated polyethylene glycol (mPEG-NH_2).

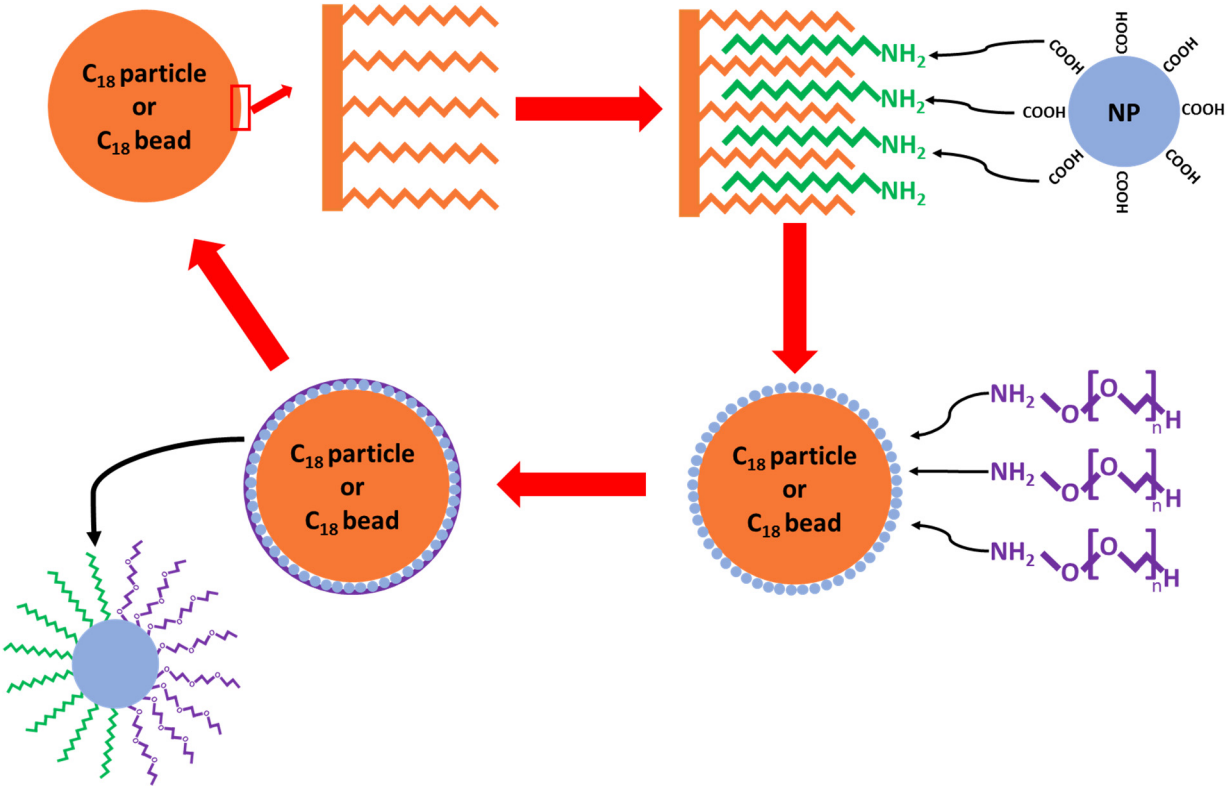

Figure 2.3: Illustration of packed column synthesis method. (Top left) Stationary phase material (orange) is coated with M1 molecules (green); (Top right) Carboxyl coated nanoparticles are reacted to the M1 headgroups; (Bottom right) M2 molecules (purple) are reacted to the exposed surface of the nanoparticles; (Bottom left) JNPs are eluted from the stationary phase material; stationary phase material is ready for next JNP synthesis.

2.1.2: Principles of Reverse Phase Chromatography and their Relation to the Packed Column Method

Chromatography has been used since the 1900's for separating components in liquid mixtures.[66] Molecules (analytes)[67] dissolved in a solvent (mobile phase) are passed through a column of solid material (stationary phase).[66] Greater affinity of analytes to the stationary phase will lead to increased interaction between the two; greater interactions will cause analytes to remain in the column longer in a continuous flow system.[68] In normal and reverse phase chromatography, strength of stationary phase-analyte interactions is based on polarity of the mobile phase molecules, polarity of the analyte, and analyte affinity to the mobile phase.[69–71] The work presented in this dissertation uses a reverse phase chromatography (RPC) stationary phase. RPC stationary phases are composed of hydrophobic materials giving them high affinity to hydrophobic/non-polar compounds.[69,70]

The packed column method relies on the stationary phase's ability to retain hydrophobic molecules. The retention factor, k, for RPC columns is determined by counting the number of column volumes required to remove all molecules from the column.[72] Since there are not databases for the retention factors of different hydrophobic molecules, properties of the analyte molecules can be used to determine molecules with greater retention factors. For RPC, retention time is increased as polarity is reduced and the number of carbon atoms is increased. Retention time is further increased if carbon chains are unbranched and saturated.[73]

Parameters for selecting M1 compounds include carbon chain length, water-solubility (and concurrently polarity), and reactivity of head groups to the nanoparticle surface. For this strategy, M1 compounds must be non-polar, have amine head groups, and have carbon tail groups to work with the RPC stationary phase and selected nanoparticles. For experiments in this work, carbon tail length was limited to 18 carbon atoms; using shorter carbon chains reduces the magnitude of Van der Waals interactions between M1 molecules and the stationary phase.[74,75] After reaction of nanoparticles to M1 molecules (Figure 2.3, step 2), cumulative Van der Waals interactions between M1 molecules and the stationary phase will stabilize nanoparticles on the stationary phase.[76] Flow of the mobile phase around the stationary phase material will produce drag force[77] on the nanoparticles. Increased carbon tail length (above 18 carbons) positions adsorbed nanoparticles in an area of higher velocity fluid flow[77], and therefore would increase the drag force

on said nanoparticle. While M1 molecules with 18 carbons were used exclusively for this work, M1 molecules with longer or shorter carbon tails can still adsorb to the stationary phase material.

2.2: Iron Oxide Core JNPs

The first potential JNP configuration (referred to as OLE-CAION-PEG) utilized a citric acid coated iron oxide nanoparticle (CAIONs), oleylamine as the M1 molecule, and mPEG-NH_2 (PEG molecule with an amine group) as the M2 molecule. Investigation into iron oxide core JNPs had two goals: prove the packed column method could produce JNPs and examine self-assembly of said JNPs. Synthesis began by preparing oleic acid coated iron oxide nanoparticles (OAIONs), followed by a ligand exchange to replace oleic acid with citric acid forming CAIONs. Isotropic control particles (CPs) were also prepared for comparison to JNPs and will be explained in detail in the following section. All nanoparticles were examined using Dynamic Light Scattering (DLS) and Fourier-transform Infrared Spectroscopy (FTIR).

Based on literature that was followed to prepare OAIONs and CAIONs, solubility parameters for both nanoparticles as well as oleylamine (hydrophobic) and PEG (hydrophilic) were all know. It was proposed that by reacting oleylamine and mPEG-NH_2 to opposing regions of CAIONs that nanoparticles would become amphiphilic and react to immiscible liquid interfaces as surfactant molecules do. Studies have shown that amphiphilic materials (e.g. surfactant molecules) reduce the interfacial tension between immiscible liquids when adsorbed to the liquid-liquid interface.[78] It was also proposed that amphiphilic nanoparticles would have a greater effect on the interfacial tension than equal concentrations of isotropic nanoparticles. To test this hypothesis, nanoparticles were added to 50/50 hexane-water mixtures to examine differences at the hexane-water interface in the presence of different nanoparticles.

2.2.1: Reaction Chemistry

Iron oxide nanoparticles were bonded to M1/M2 molecules using carboxyl-amine (via NHS/EDC activation) reactions. This reaction is shown in detail in Figure 2.4:

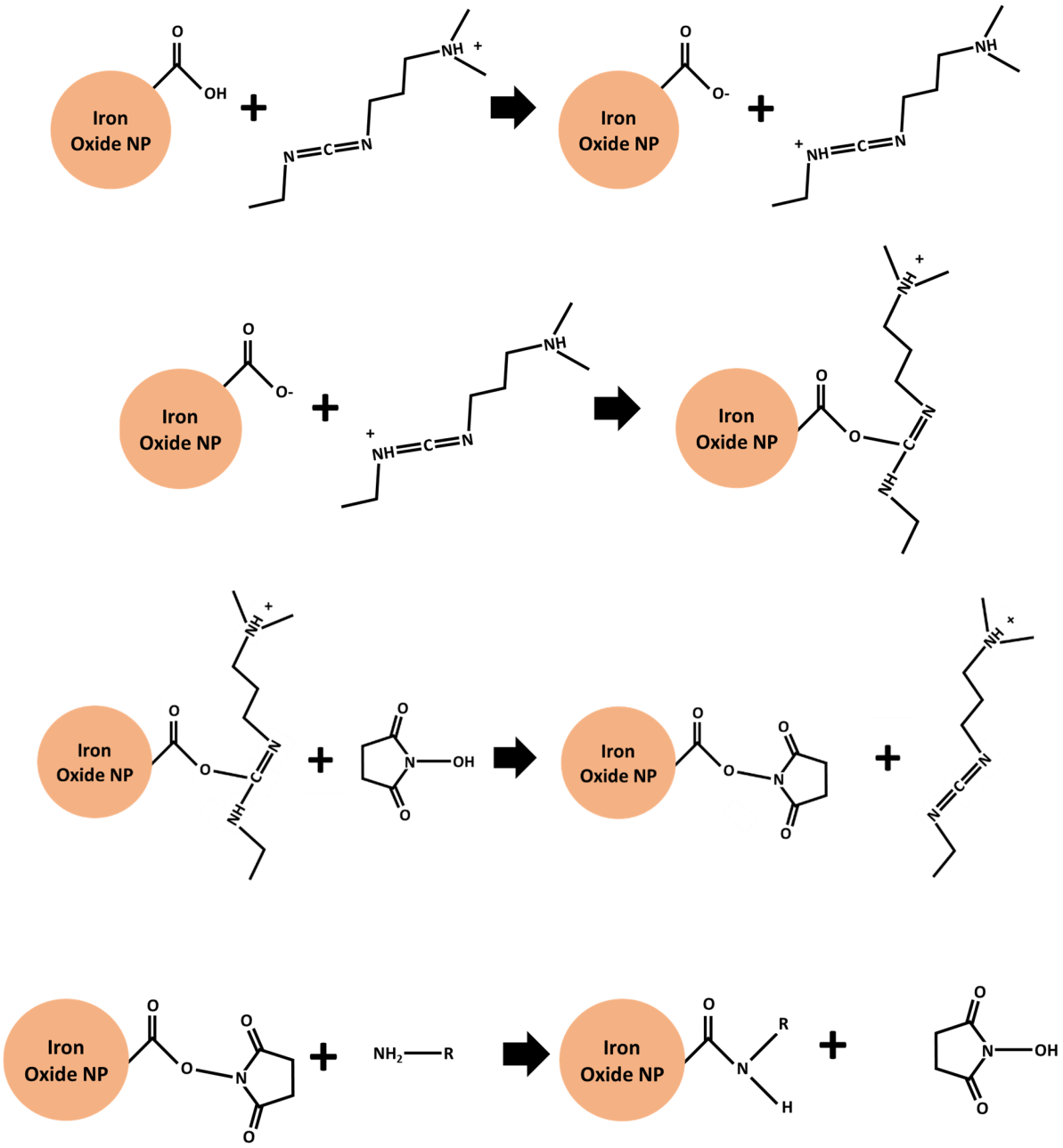

Figure 2.4: Carboxyl-amine reaction. (top to bottom) Step 1: carboxy group (weak acid) protonates carbodiimide group on EDC and forms a carboxylate anion. Step 2: carboxylate anion nucleophile reacts with carbodiimide forming O-acylisourea intermediate. Step 3: carboxylic oxygen separates from O-acylisourea leaving group and bonds with NHS. Step 4: Amine nucleophile forces NHS to break carboxylic oxygen. Carboxyl-amine bond is formed.[79]

2.2.2: Materials/Equipment

For OAION synthesis, iron(III) acetylacetonate (iron (III) acac) ($Fe(C_5H_7O_2)_3$) was obtained from Alfa Aesar. Tetradecanediol ($CH_3(CH_2)_{11}CH(OH)CH_2OH_2$) was obtained from Tokyo Chemical Industry (TCI). Oleylamine ($C_{18}H_{35}NH_2$) was obtained from Alfa Aesar. Oleic Acid ($C_{18}H_{34}O_2$, 90%) was obtained from TCI. Ethyl Ether ($(C_2H_5)_2O$) was obtained from The British Drug Houses Chemicals (BDH). For CAION synthesis, citric acid monohydrate ($C_6H_8O_7$) was obtained from Amresco. Dimethylformamide (DMF) (C_3H_7NO) was obtained from Amresco. 1,2-Dichlorobenzene (DCB) ($C_6H_4Cl_2$, 99%) was obtained from Acros. 1.0 M sodium hydroxide (NaOH) was made from sodium chloride (NaCl) from Amresco and ultrapure water. For OLE-CAION-PEG synthesis, C_{18} Spherical Silica Gel was obtained from Sorbtech. 1-ethyl-3-(dimethylaminopropyl)carbodiimide (EDC) ($C_8H_{17}N_3$) was obtained from Alfa Aesar. N-hydroxysuccinimide (NHS) ($C_4H_5NO_3$, 98%) was obtained from TCI. mPEG-NH_2 (MW 5000) was obtained from NANOCS. Additional solvents include chloroform ($CHCl_3$), hexane (C_6H_{14}), acetone (C_3H_6O), and methanol (CH_4O) were obtained from BDH. Ethyl Acetate ($C_4H_8O_2$, 99%) was obtained from Alfa Aesar. Ethanol (C_2H_6O) (200 proof) was obtained from EMD. HEPES ($C_8H_{18}N_2O_4S$) was obtained from Alfa Aesar.

Ultrapure water was obtained using an ELGA PURELAB Flex water purification system. Temperature cycles were controlled with a J KEM Scientific Gemini Dual Channel Controller. DLS measurements were performed with a Malvern ZetaSizer Nano-ZS. FT-IR measurements were performed with a Nicolet IR-100. Solvent evaporation was done in a Heidolph Hei-VAP Value "The Collegiate" rotary evaporator (further referred to as "rotovap").

2.2.3: Synthesizing OAIONs

OAIONs were synthesized via thermal decomposition following the method development by Sun et al.[80] Iron (III) acac, tetradecanediol, oleic acid, oleylamine, and benzyl ether were combined in a 100 mL 3 neck round bottom flask; the flask was equipped with a condenser, a temperature probe, and a nitrogen line to blanket the reaction. The three-neck flask was insulated and placed in a heating mantel; the apparatus was heated following the temperature cycle in Table

2.1 and stirred with a magnetic stir rod. Figure 2.5 shows a photograph of the equipment set-up for this synthesis.

Table 2.1 Heating Cycle for Synthesizing OAIONs

Step	Starting Temp (°C)	Final Temp (°C)	Hold Time (hours)
1	0	100	1
2	100	200	2
3	200	240	1
4	250	25	Cool down

Figure 2.5: Setup of reaction vessel for synthesizing OAIONs

After the heating cycle, the reaction apparatus was dismantled, and the remaining solution was removed and mixed with methanol and allowed to magnetically separate overnight. The solvent was removed, and the nanoparticles were washed three times in a 4:1 methanol/hexane mixture using magnetic separation. Nanoparticles were stored in hexane.

2.2.4 Converting OAIONs to CAIONs

The oleic acid coating on OAIONs was replaced with citric acid via ligand exchange following the work of Hatakeyama et al.[81] In a 100 mL round bottom flask, dry OAIONs were combined with citric acid in a 6:5 citric acid to OAIONs ratio by weight. DCB, DMF and a magnetic stir rod were added to the flask; the temperature probe was inserted, and the flask was sealed. The mixture is run through the heating cycle described in Table 2.2.

Table 2.2 Heating Cycle for Synthesizing CAIONs

Step	Starting Temp (°C)	Final Temp (°C)	Hold Time (hrs)
1	25	120	4
2	120	80	1
3	80	25	Cool down

After the Step 1 of the cycle, 2 mL of 1.0 M NaOH was added to the mixture. Once the temperature cycle was completed and the mixture had cooled to room temperature, the nanoparticles were removed from the solvent via magnetic separation. Nanoparticles were washed multiple times in acetone, ethyl acetate, and methanol using magnetic separation. After washing, the nanoparticles were stored in DI water.[81]

2.2.5: Synthesizing Iron Oxide Nanoparticles with oleylamine/mPEG-NH_2 coatings (OLE-CAION-PEG)

A 6 mL column was loaded with 500 mg of C_{18} particles. 10.0% oleylamine in ethanol by volume was added to the column (sealed) and allowed to adsorb to C_{18} particles for 15 minutes.

The solution was then drained and the column was washed with a 10.0% methanol/water solution and then with water. CAIONs in 20 mM HEPES (pH: 7.5) buffer were prepared for amine reaction with NHS and EDC, then added to the column (sealed) and allowed 2 hours to react. The column was then drained and washed with water. mPEG-NH_2 was dissolved in 20 mM HEPES buffer and added to the column; 4 hours of reaction time was allowed. The column was then drained and washed with water. Nanoparticles were eluted from the column in chloroform. Chloroform was removed from the nanoparticles using rotary evaporation; nanoparticles were resuspended in methanol and washed 3 times using magnetic separation. Functionalized nanoparticles were stored in chloroform; an illustration of OLE-CAION-PEG is shown in Figure 2.6; note that the nanoparticle and surface compounds in Figure 2.6 are not to scale.

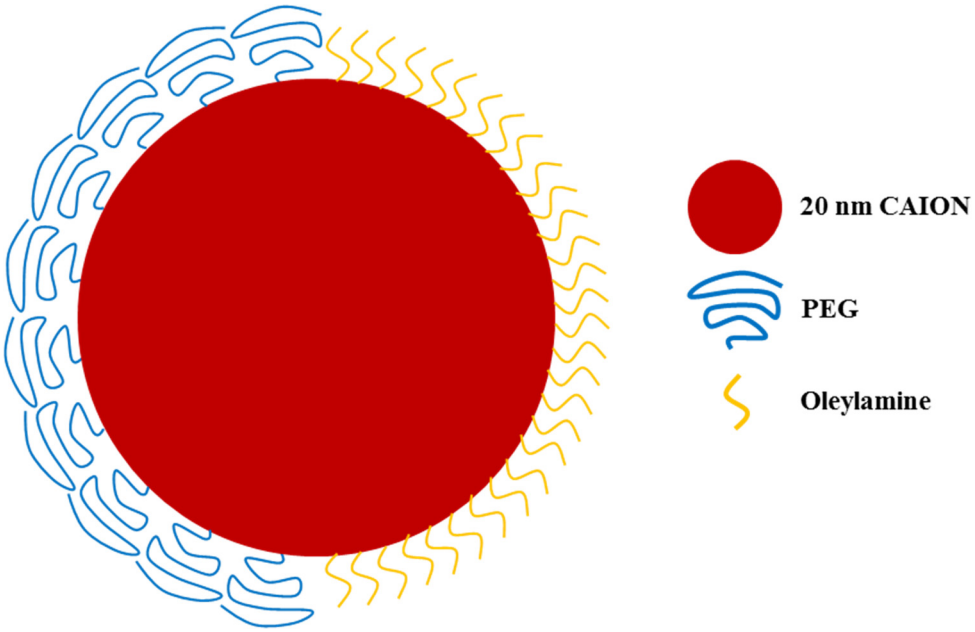

Figure 2.6: Illustration of OLE-CAION-PEG: iron oxide nanoparticle with surface regions of oleylamine (yellow) and PEG (blue)

2.2.6: Synthesizing Iron Oxide CPs

PEGylated CAIONs: NHS and EDC were added to 20 nm CAIONs in 20 mM HEPES buffer. Nanoparticles were allowed to react with NHS/EDC for 15 minutes, then mPEG-NH_2 (MW 5000) was added to the mixture and allowed to react for 4 hours. The PEGylated nanoparticles were washed 3 times in water using magnetic separation and stored in water.

OA coated CAIONs: A 6 mL column was loaded with 500 mg of C_{18} particles. 10.0% oleylamine in ethanol was added to the column (sealed) and allowed to adsorb to C_{18} particles for 15 minutes. The solution was drained and the column was washed with a 10.0% methanol/water solution and then with water. CAIONs in 20 mM HEPES buffer were prepared for amine reaction with NHS and EDC, then added to the column (sealed) and allowed 2 hours to react. The column was drained and washed with water. A second solution of NHS/EDC in 20mM HEPES buffer was added to the column and allowed to react for 15 minutes. The column is drained and 10.0% oleylamine in ethanol was added to the column and allowed to react for 2 hours. Nanoparticles were eluted from the column using ethanol, then washed in ethanol three times using magnetic separation. Functionalized nanoparticles were stored in ethanol.

2.3: Results and Discussion

Average hydrodynamic diameter and hydrodynamic diameter range of OAIONs, CAIONs, and OLE-CAION-PEG was measured using the DLS.[82] DLS measurements were taken to confirm consistency of the hydrodynamic diameter range for nanoparticles after each reaction. As shown in Figure 2.7, all samples show a size range between 10 - 25 nm and an average size between 14 - 18 nm; this indicates that no aggregation has occurred.

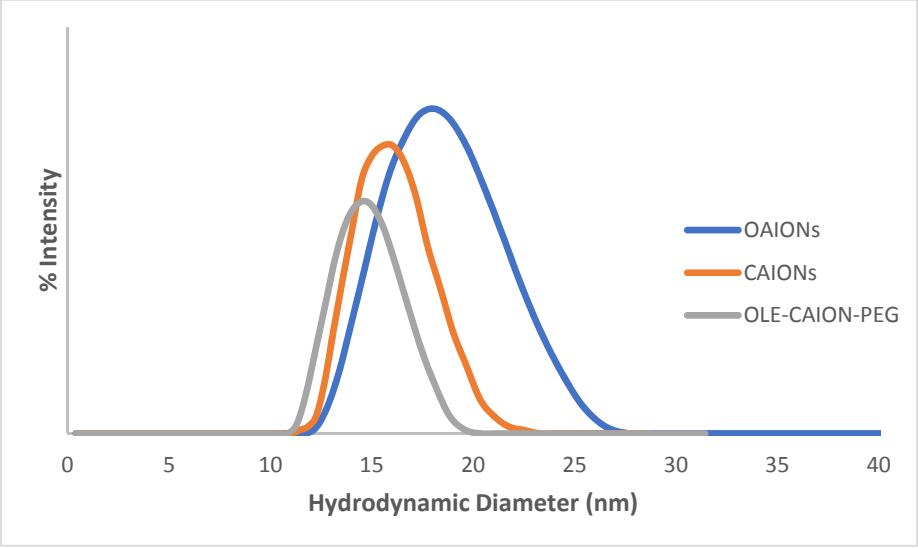

Figure 2.7: Graph showing range of hydrodynamic diameters of OAIONs in hexane (blue), CAIONS in water (orange), and OLE-CAION-PEG in chloroform (gray) measured by DLS

Reaction of M1 and M2 molecules to the nanoparticle surface was confirmed using FTIR; spectrums for each sample are shown in Figure 2.8. Peaks from 1000-1100 cm^{-1}, indicative of carbon-oxygen bond stretching, and from 2900-3000 cm^{-1}, indicative of methylene bond stretching, are seen in all samples due to unreacted citric acid groups. Methylene peaks (2900-3000 cm^{-1}) are more intense in the presence of oleylamine and PEG; the carbon-oxygen peak (1000-1100 cm^{-1}) is more intense in the presence of PEG.[83–86] Examination of peak locations and comparison of peak intensities in Figure 2.8 indicate effective bonding of oleylamine and/or PEG to the CAION surface.

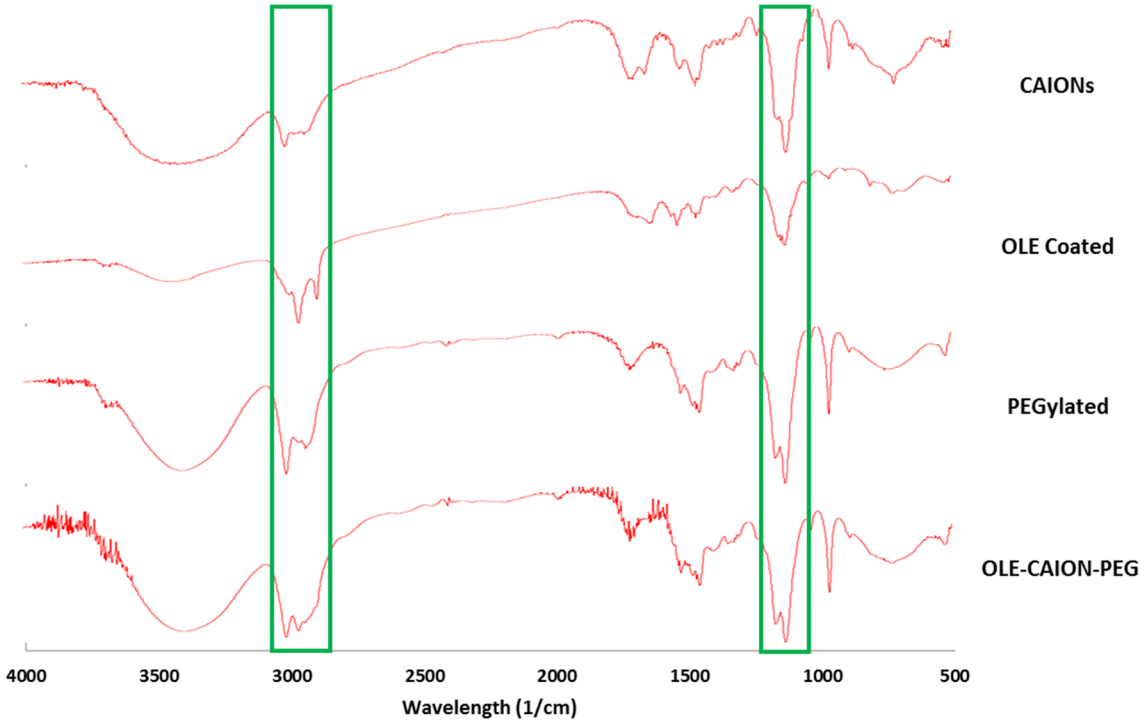

Figure 2.8: FTIR Spectrums (wavelength vs % transmittance) for unreacted CAIONs, PEGylated CAIONs, OLE coated CAIONs, and OLE-CAION-PEG.

To examine nanoparticle self-assembly, OAIONs, CAIONs, and OLE-CAION-PEG were dried and resuspended (individually) in 50/50 hexane/water mixture. A photograph of these vials is shown in Figure 2.9:

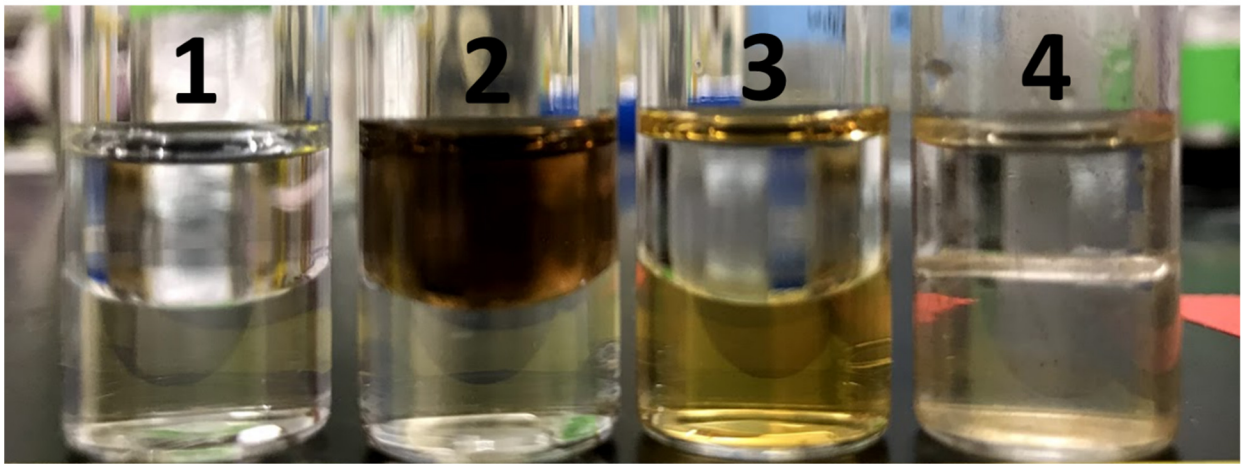

Figure 2.9: (from left to right) 50% hexane/water mixture with (1) no nanoparticles, (2) OAIONs, (3) CAIONs, and (4) OLE-CAION-PEGs

From Figure 2.9, vial 1 contains no nanoparticles, hydrophobic OAIONs partition into the hexane phase in vial 2, and hydrophilic CAIONs partition into the water phase in vial 3. OLE-CAION-PEG nanoparticles in vial 4 were not visible in either solvent; there was also a visible difference between the menisci formed in vials 1-3 and the meniscus in vial 4. Average contact angles between the glass surface and the fluid interface (Θ) through the water are shown in Figure 2.10. T-tests and Anova tests were performed to determine significant or insignificant differences between average contact angles between vials 1-4. The t-test and Anova test both compare the mean values from data sets to determine significant or insignificant difference between the means.[87,88] T-tests are used to compare two data sets; 6 t-tests (specifically two-sample t-tests assuming unequal variance) were performed to determined significance or insignificance between all vials (1 vs. 2, 1 vs. 3, etc.). Anova tests can determine significanct or insignificant difference between more than 2 data sets[88]; Anova tests were performed on vials 1-3 and vials 1-4 to confirm results from t-tests. P-values (probability values) are determined from each statistical test; p-values less than 0.05 indicate a significant difference between mean values in the compared data sets.[89]

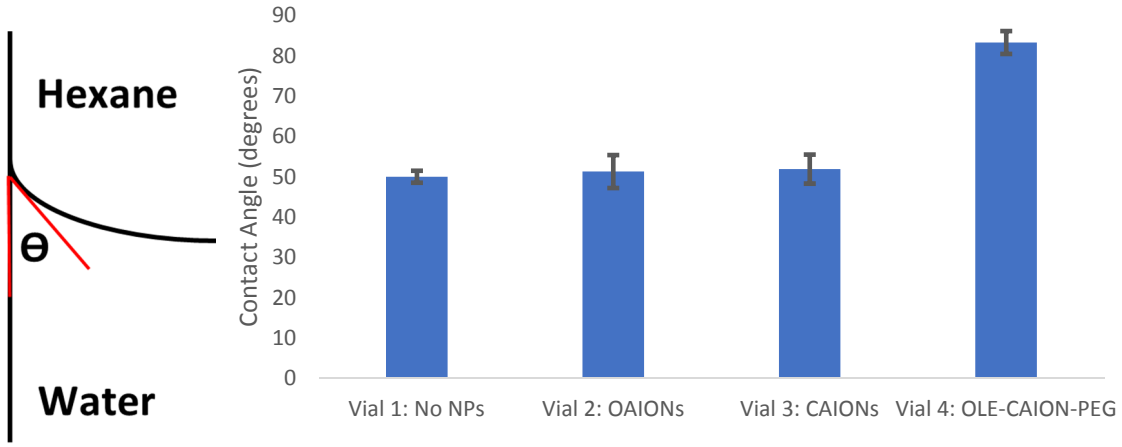

Figure 2.10: (left) Illustration indicating angle Θ at the hexane/water interface. (right) Average contact angles between glass vial and hexane/water interface through the water region.

Significant difference was determined between vial 4 and all other vials; p values from t-tests for vial 1 vs. 4, 2 vs. 4, and 3 vs. 4 were $2.2*10^{-14}$, $7.0*10^{-13}$, and $7.6*10^{-14}$, respectively. P values from t-tests comparing vials 1 vs. 2, 1 vs. 3, and 2 vs. 3were all greater than 0.05, indicating no significant differences between vials 1-3. Anova tests confirmed these results; p-value for the test on vials 1-3 was 0.42 and p-value for the test on vials 1-4 was $1.8*10^{-24}$.

Menisci are formed when adhesive forces, attractive forces between unlike molecules, are stronger or weaker than cohesive forces, attractive forces between like molecules.[90] Meniscus shape is also influenced by interfacial tension at either the gas-liquid or liquid-liquid interface.[91] Interfacial tension between hexane and water (γ) in the vials shown in Figure 2.9 can be calculated by combining equations for the effective interfacial energy (E) and the definition of interfacial tension shown by Du et. al and Zhang et. al:

$$E = \gamma_{hw} A + N_s \Delta E_{ad} \quad (1)$$

where γ_{hw} is the interfacial tension between hexane and water (no adsorbed nanoparticles), A is the interfacial area, N_s is the number of adsorbed nanoparticles at the liquid-liquid interface, and ΔE_{ad} is the change in free energy per nanoparticle adsorbed to the liquid-liquid interface.[78,92] ΔE_{ad} is defined as:

$$\Delta E_{ad} = -\pi R^2 \gamma_{hw} (1 - \cos(\theta_{hw}))^2 \quad (2)$$

where R is the nanoparticle radius and Θ_{hw} is the hexane-water contact angle measured through the water phase.[78,92] Interfacial tension is defined as surface energy per unit area[93–95]; an expression can be developed for the interfacial tension of the nanoparticle-covered interface (γ):

$$\gamma = \frac{E}{A} = \gamma_{hw} + \frac{N_s \Delta E_{ad}}{A} \quad (3)$$

By combining equations 2 and 3, interfacial tension of the nanoparticle-covered interface (γ) is related to the hexane-water contact angle (Θ_{hw}):[78,92]

$$\gamma = \gamma_{hw}[1 - \phi(1 - \cos(\theta_{hw}))^2] \quad (4)$$

$$\phi = \frac{N_s \pi R^2}{A} \quad (5)$$

Two assumptions need to be made to calculate interfacial tension using these equations: the first assumption neglects the effects of interactions between nanoparticles. In reality, intermolecular forces between suspended nanoparticles and nanoparticles assembled at the interface will affect the formation of a nanoparticle layer.[78] To the author's knowledge, there is not a model to quantify how much the nanoparticle-nanoparticle forces will affect the interfacial tension, and equation 5 gives the best estimate. The second assumption involves the number of nanoparticles assembled at the liquid-liquid interface, N_s. From Figure 2.9, nanoparticles in vials 2 and 3 are partitioned in the hexane phase and water phase, respectively, and nanoparticles in vial 4 are not seen in either fluid and are assumed to be adsorbed to the hexane-water interface. Since the number of nanoparticles at the interface in vials 2, 3, and 4 cannot be quantified, interfacial tension in each vial was calculated with ϕ values of 0.25, 0.5, and 0.9069. These values represent a 25%, 50%, and 90.69% nanoparticle coverage of the liquid-liquid interface, respectively. A monolayer of spheres covering 100% of the liquid-liquid interface is physically impossible; 90.69% of the surface is the maximum that can be covered.[96] Vial 1 does not contain nanoparticles, hence the value for ϕ is 0 and the interfacial tension γ is 51.1 mN/m for all sample sets. Values for interfacial tension are shown in Figure 2.11. T-tests and Anova tests were run between vials 2-4 at each coverage percentage; p-values from t-tests are shown in Table 2.3.

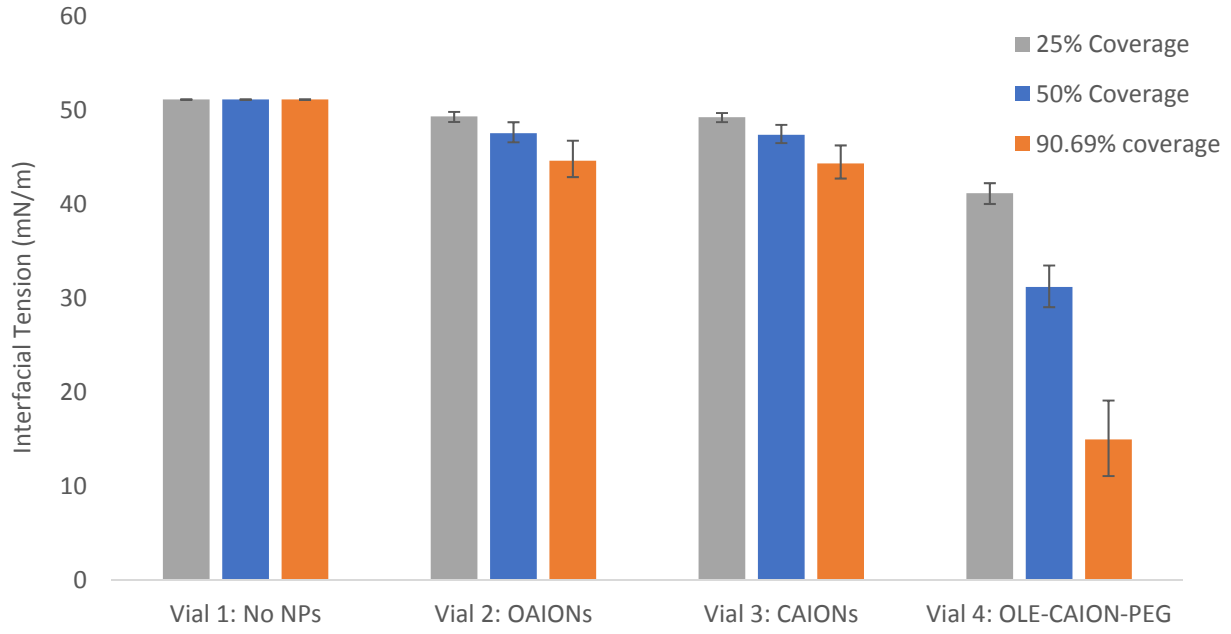

Figure 2.11: Bar graph showing the interfacial tension (γ) for vials shown in Figure 2.9 at ϕ=0.25 (gray), ϕ=0.50 (blue), ϕ=0.9069 (orange).

Table 2.3: P-values from Comparison of Interfacial Tensions Values

First Data Set	Second Data Set	Φ	P value
Vial 2 - OAIONs	Vial 3 - CAIONS	0.25	7.2E-01
Vial 2 - OAIONs	Vial 4 - OLE-CAION-PEG	0.25	2.3E-13
Vial 3 - CAIONS	Vial 4 - OLE-CAION-PEG	0.25	6.9E-12
Vial 2 - OAIONs	Vial 3 - CAIONS	0.50	8.5E-01
Vial 2 - OAIONs	Vial 4 - OLE-CAION-PEG	0.50	3.5E-11
Vial 3 - CAIONS	Vial 4 - OLE-CAION-PEG	0.50	6.9E-11
Vial 2 - OAIONs	Vial 3 - CAIONS	1.00	7.2E-01
Vial 2 - OAIONs	Vial 4 - OLE-CAION-PEG	1.00	3.3E-12
Vial 3 - CAIONS	Vial 4 - OLE-CAION-PEG	1.00	4.9E-12

Figure 2.11 shows significantly lower interfacial tension in vial 4 then in vials 1-3 for all ϕ values and no significant difference between vials 1, 2, and 3 (significant differences confirmed by p-values in Table 2.3). Anova tests confirmed t-test results; Anova test p-values on vials 2-3 at all ϕ values were greater than 0.05, and p-values on vials 2-4 were all less than 0.05. Glaser et al. also examined the interfacial tension of hexane and water in the presence of isotropic and anisotropic

nanoparticles. They determined that anisotropic amphiphilic nanoparticles caused a greater reduction in the interfacial tension than isotropic nanoparticles, consistent with the results presented in Figure 2.11. There is also a significant difference between the interfacial tension for vial 1 vs. vial 2 and vial 1 vs. vial 3. Research into nanoparticle suspensions have shown that cohesive force between solvent molecules increases in the presence of nanoparticles.[93,97] Increase in cohesive force leads to a shorter, flatter meniscus, and thusly a larger contact angle Θ which will reduce the value for interfacial tension when calculated using the aforementioned equations. Studies have also shown that isotropic nanoparticles can assemble at the liquid-liquid interface and reduce the overall interfacial tension;[78,92] it is possible that OAIONs and/or CAIONs are both suspending in hexane or water, respectively, and also assembling at the interface. Table 2.4 compares % reductions in interfacial tension between isotropic and anisotropic nanoparticles from this work and from published literature.

Table 2.4: Comparison of % Reduction in Interfacial Tension for Nanoparticle coated Liquid-Liquid Interfaces

Author	Zhang et al.	Zhang et al.	Glaser et al.	This Work	This Work	Glaser et al.	This Work
NP Type	Hydrophobic Silica (Isotropic)	Hydrophilic Silica (Isotropic)	Hydrophilic Iron Oxide (Isotropic)	OAION	CAION	Anisotropic Iron Oxide / Gold	OLE-CAION-PEG
Solvent 1	Hexadecane	Hexadecane	Hexane	Hexane	Hexane	Hexane	Hexane
Solvent 2	Water	Water	Water	Water	Water	Water	Water
Initial γ (mN/m)	53.5	53.5	51.1	51.1	51.1	51.1	51.1
Final γ (mN/m)	49	45.3	34.5	44	44	18	11
% Reduction in γ	8.4%	15.3%	32.5%	13.9%	13.9%	64.8%	78.5%

NOTE: Columns in green indicate studies done with isotropic nanoparticles; orange indicates studies done with anisotropic nanoparticles

2.4: Summary

Evidence of regionally specific surface modifications for OLE-CAION-PEG nanoparticles was developed from these experiments. DLS analysis of OAIONs, CAIONS, and OLE-CAION-PEG nanoparticles shows that monodisperse nanoparticle samples can be developed from each reaction. FTIR analysis confirms the presence of oleylamine and PEG on the surface of OLE-CAION-PEG as well as on the CPs. Exposing OAIONs, CAIONS, and OLE-CAION-PEG to a 50/50 hexane-water environment shows that OLE-CAION-PEG nanoparticles have a different effect on the liquid-liquid interface that is not seen in the other samples likely due to nanoparticle assembly at the interface. Interfacial tension between hexane and water was measured at 3 different nanoparticle coverage percentages; all calculations showed significantly lower interfacial tension in samples containing OLE-CAION-PEG nanoparticles. This reduction in interfacial tension further indicates OLE-CAION-PEG nanoparticle assembly at the hexane-water interface and thusly the creation of amphiphilic two-sided nanoparticles. In Chapter 3, 20 nm iron oxide nanoparticles are replaced with 300 nm silica nanoparticles in all experiments. Nanoparticles in Chapter 3 were examined using optical and electron microscopy to further investigate nanoparticle surface modifications to verify the findings discussed in Chapter 2.

Chapter 3: Producing Silica JNPs using Spherical Masking in a Packed Column

3.1: Introduction

Investigation into formation of Janus nanoparticles transitioned from utilizing 10-20 nm iron oxide nanoparticles to 300 nm silica nanoparticles. While nanoparticles are examined using a transmission electron microscope (TEM) or scanning electron microscope (SEM), larger diameter silica allows for visualization of surface modifications with certain nanoscale materials. This point will be proven later in this Chapter. Figure 3.1 shows TEM images of 20 nm iron oxide nanoparticles and 300 nm silica nanoparticles. In this chapter, 8 silica nanoparticle configurations were prepared using the packed column method to selectively modify the nanoparticle surface with long chain hydrophobic molecules, PEG molecules, iron oxide nanoparticles, and/or fluorescent dyes.

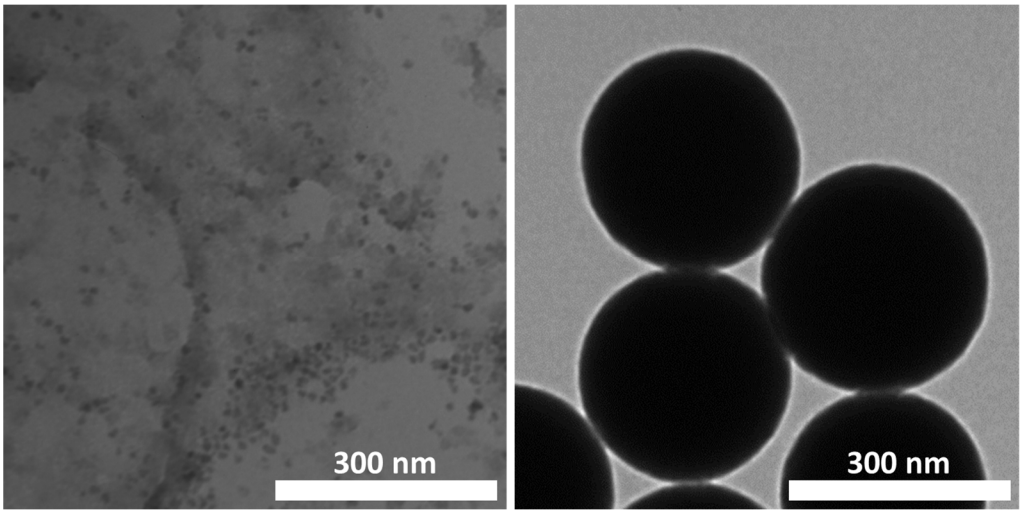

Figure 3.1: (left) TEM images of 20 nm iron oxide nanoparticles; (right) TEM images of 300 nm silica nanoparticles

Concurrently with investigation into silica nanoparticles, changes to the synthesis method were made to improve JNP synthesis conditions. The iron oxide configuration (OLE-CAION-PEG) and the first 3 silica configurations were produced using C_{18} particles and oleylamine as the M1 compound. For all configurations to follow, oleylamine was replaced with stearylamine. Stearylamine has a nearly identical atomic structure as oleylamine, but is completely saturated. The straight chain hydrophobic tail on stearylamine will increasing packing density on M1 compounds on the stationary phase surface, providing a more uniform and complete coating of the stationary phase surface when compared to the bent chain of oleylamine;[98] this concept is shown graphically in Figure 3.2. Note that Figure 3.2 shows an ideal condition for adsorption of molecules to the functionalized surface; hydrophobic groups on the stationary phase surface will not have identical orientation on actual C_{18} particles. C_{18} particles (62-75 μm diameter) were replaced with C_{18} beads (900-1100 μm diameter) to alleviate issues during nanoparticle masking. While measures were taken to completely coat the stationary phase with M1 molecules, packed columns likely had surface area without adsorbed molecules. With hydrophobic surface area exposed on the stationary phase, washing steps involving aqueous solutions required more than gravitational force to pass through the column. This increase in pressure drop can cause liquid channeling as well as greater flow at the walls of the column compared to flow through the packing material[99–101], and can lead to improperly formed JNPs. Details on the design and production of C_{18} beads is given in section 3.2.1.

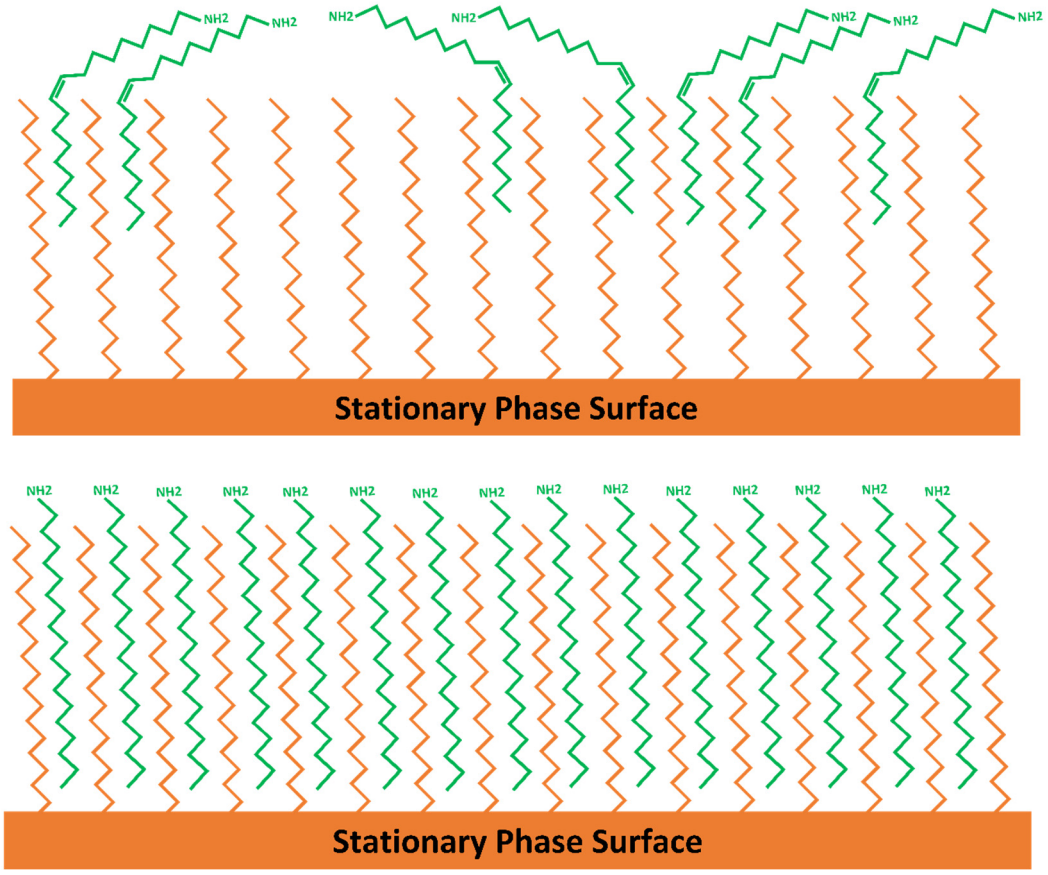

Figure 3.2: (top) Illustration of the stationary phase surface coated with oleylamine. Due to oleylamine's kinked geometry, coatings on the stationary phase surface can be incomplete; (bottom) illustration of stationary phase surface coated with stearylamine. Stearylamine's straight geometry provides a more uniform coating on the stationary phase surface.

3.2: Silica JNPs

3.2.1: Reaction Chemistry

Two reaction chemistries were used to bond M1/M2 molecules and/or crosslinkers to silica nanoparticles: aldehyde-amine and isothiocyanate-amine. These reactions are shown in detail in Figures 3.3 and 3.4:

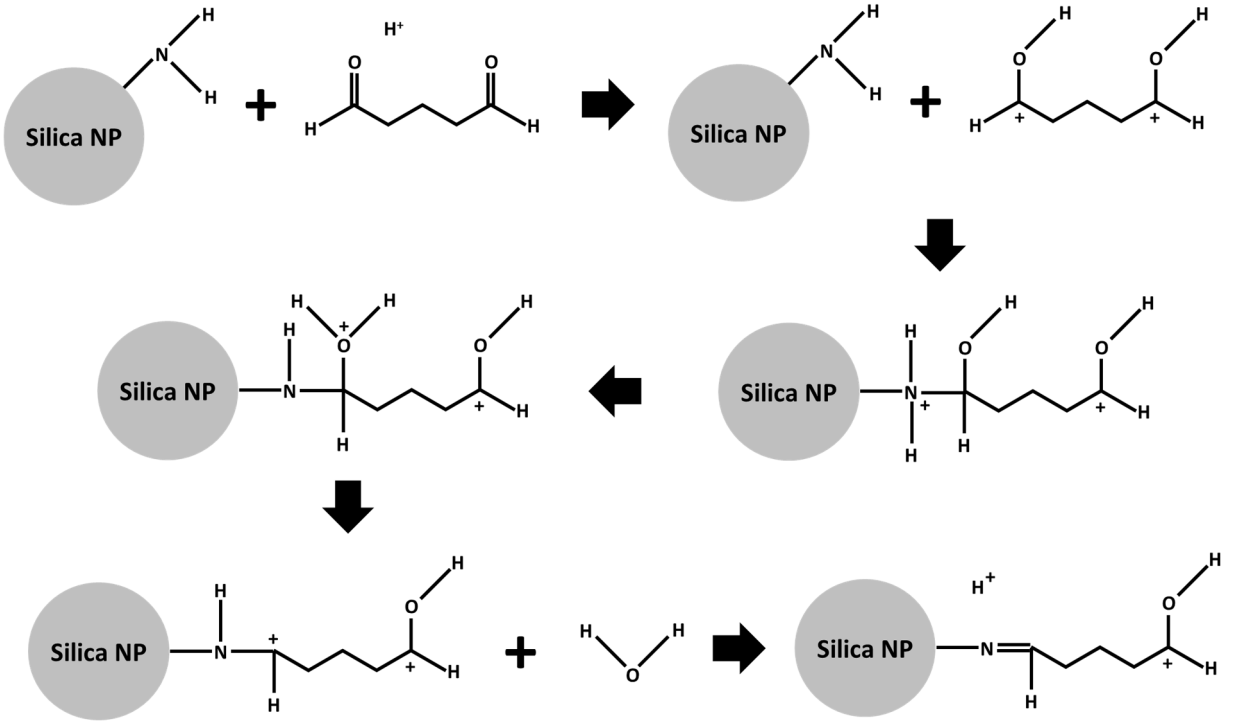

Figure 3.3: Aldehyde-amine reaction: amine nucleophile bonds to carbon on aldehyde group. Proton transfers from amine nitrogen to aldehyde oxygen forming water. Deprotonation of aldehyde carbon forms a Schiff base[102] and competes the reaction[103]

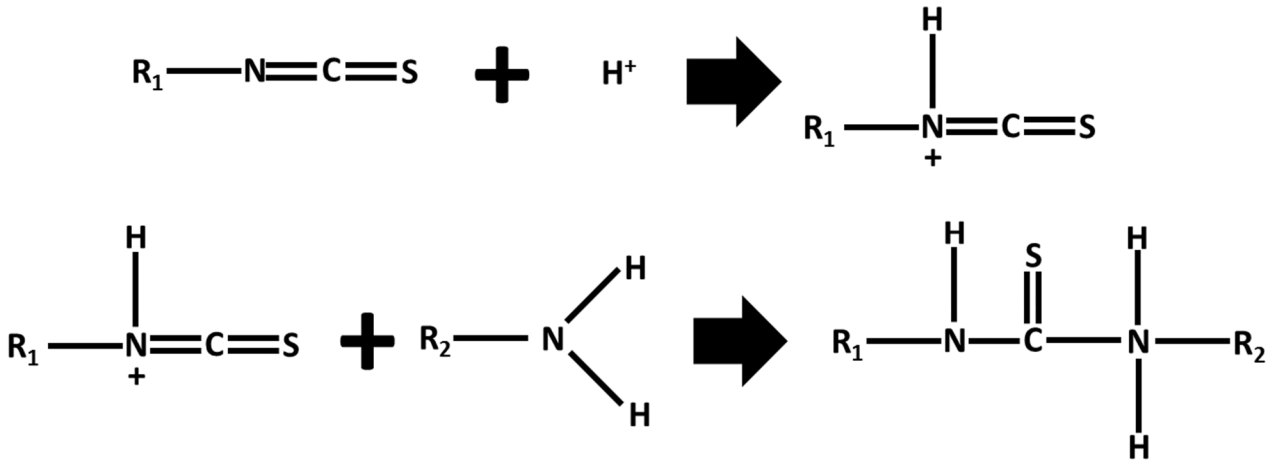

Figure 3.4: Isothiocyanate-amine reaction; step 1: protonation of isothiocyanate nitrogen due to acidic environment. Step 2: Amine nucleophile breaks carbon-nitrogen double bond to bond to isothiocyanate carbon. Isothiocyanate-amine bond formed[104]

3.2.2: Materials/Equipment

300 nm silica nanoparticles were obtained from NanoComposix. Oleylamine ($C_{18}H_{35}NH_2$) was obtained from Alfa Aesar. 1.0 M sodium hydroxide (NaOH) was made from sodium chloride (NaCl) from Amresco and ultrapure water. Octadecatrimethoxysilane ($C_{21}H_{46}O_3Si$) was obtained from TCI. Toluene (C_7H_8) was obtained from BDH. C_{18} Spherical Silica Gel was obtained from Sorbtech. mPEG-NH_2 (MW 5000), mPEG-NHS (MW 5000 and 20000), and FITC-PEG-NHS (MW 5000) were obtained from NANOCS. Glutaraldehyde ($CH_2(CH_2CHO_2)_2$) was obtained Amresco. Fluorescein isothiocyanate (FITC) ($C_{21}H_{11}NO_5S$) was obtained from Alfa Aesar. Rhodamine B isothiolcyanate (RHOB) ($C_{29}H_{30}ClN_3O_3S$) was obtained from Alfa Aesar. HEPES ($C_8H_{18}N_2O_4S$) was obtained from Alfa Aesar. Additional materials are noted in Chapter 2, section 2.2.2.

An EVOS AMG optical fluorescent microscope was used for bright field and fluorescent imaging. An Olympus BX51 optical microscope with a dark-field condenser was used for dark-field imaging. A Zeiss EM 10A/B Hi-RES Transmission Electron Microscope was used for imaging. Additional equipment is previously noted in Chapter 2, section 2.2.2.

3.2.3: Synthesizing two-sided silica nanoparticles in a C_{18} Particle Packed Column

A 6 mL column was loaded with 500 mgs of C_{18} particles. 10.0% oleylamine (M1 compound) in ethanol by volume was added to the column (sealed) and allowed to adsorb to the stationary phase for 15 minutes. The solution was then drained and the column was washed with a 10.0% methanol/water solution and then with water. 25.0% glutaraldehyde in 20 mM HEPES buffer by volume was added to the column (sealed) and allowed to react for 1 hour, followed by a water washing step. 300 nm silica nanoparticles were added to the column (sealed) and allowed to react for 1 hour, followed by a water washing step. 3 different M2 compounds were used to produce 3 different configurations: CAIONs in 20 mM HEPES buffer (pH: 7.5) followed by mPEG-NH_2 (MW 5000) in equal parts DMSO and 20 mM HEPES buffer (pH: 7.5), mPEG-NH_2 (MW 5000) in equal parts DMSO and 20 mM HEPES buffer (pH: 7.5), and FITC in ethanol. Reaction times for M2 compounds varied from 2-12 hours depending on the molecule. The column was then drained and washed with water. Nanoparticles were eluted from the column in

chloroform. Solvent was removed from the nanoparticles using a rotary evaporator; nanoparticles were resuspended in hexane and washed using centrifugation. Functionalized nanoparticles were stored in chloroform. Table 3.1 gives the names and structures of each configuration; illustrations of each configuration are shown in Figures 3.5-3.7. Note that the nanoparticle and surface compounds in Figures 3.5-3.7 are not to scale.

Table 3.1: Descriptions of Silica Nanoparticle Configurations Prepared in a C_{18} Particle Packed Column

Name	M1 Compound	Crosslinker	NP	M2 Compound	Additional M2 Compound
OLE-Si-CAION+PEG	Oleylamine	Glutaraldehyde	Silica	CAION	mPEG-NH_2
OLE-Si-PEG	Oleylamine	Glutaraldehyde	Silica	mPEG-NHS	--------
OLE-Si-FITC	Oleylamine	Glutaraldehyde	Silica	FITC	--------

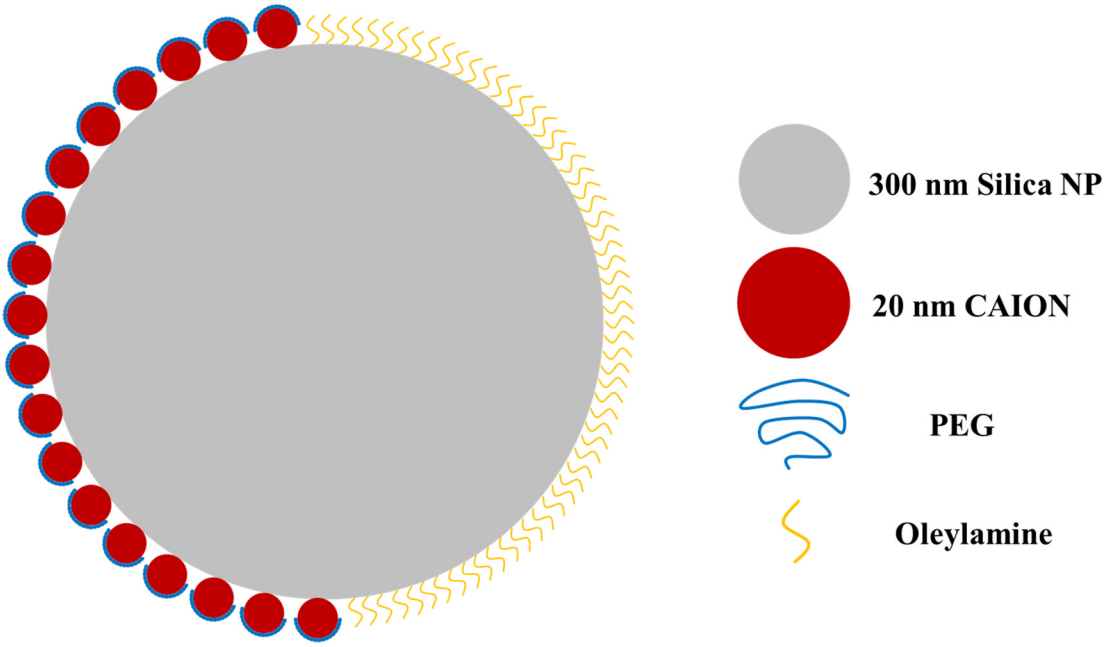

Figure 3.5: Illustration of OLE-Si-CAION+PEG: silica core with regions composed of oleylamine and CA-MNP / mPEG-NH_2

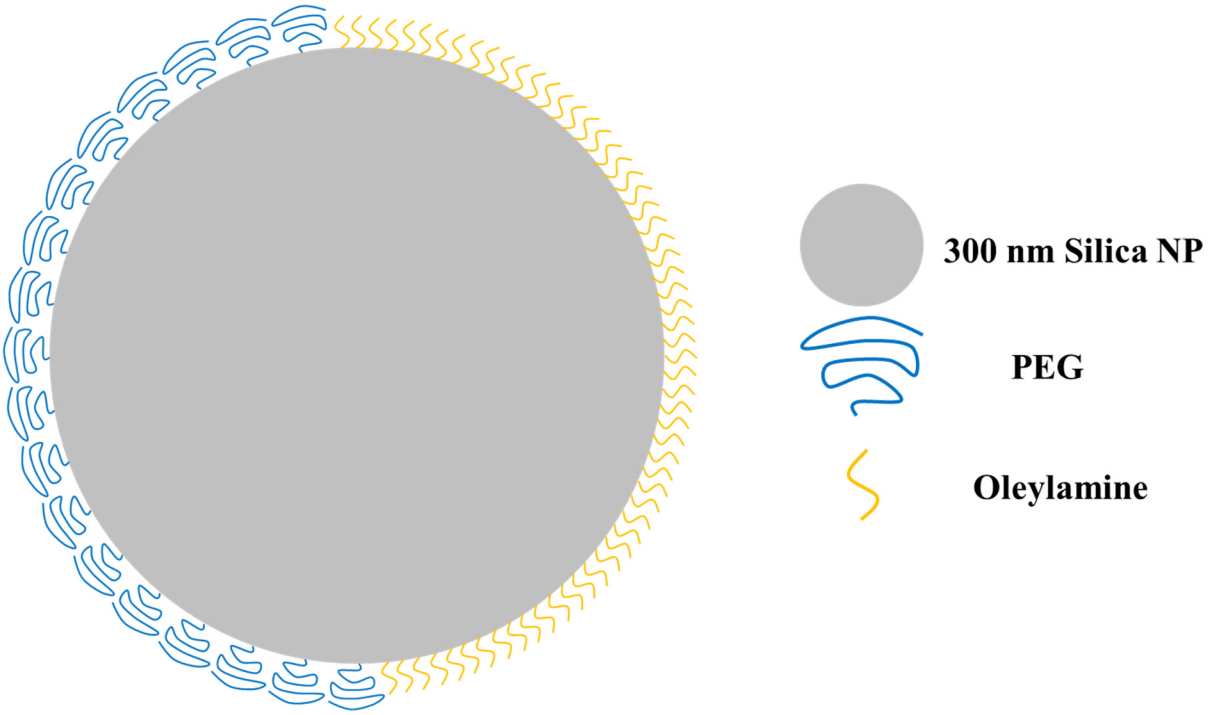

Figure 3.6: Illustration of OLE-Si-PEG: silica core with regions composed of oleylamine and mPEG-NHS

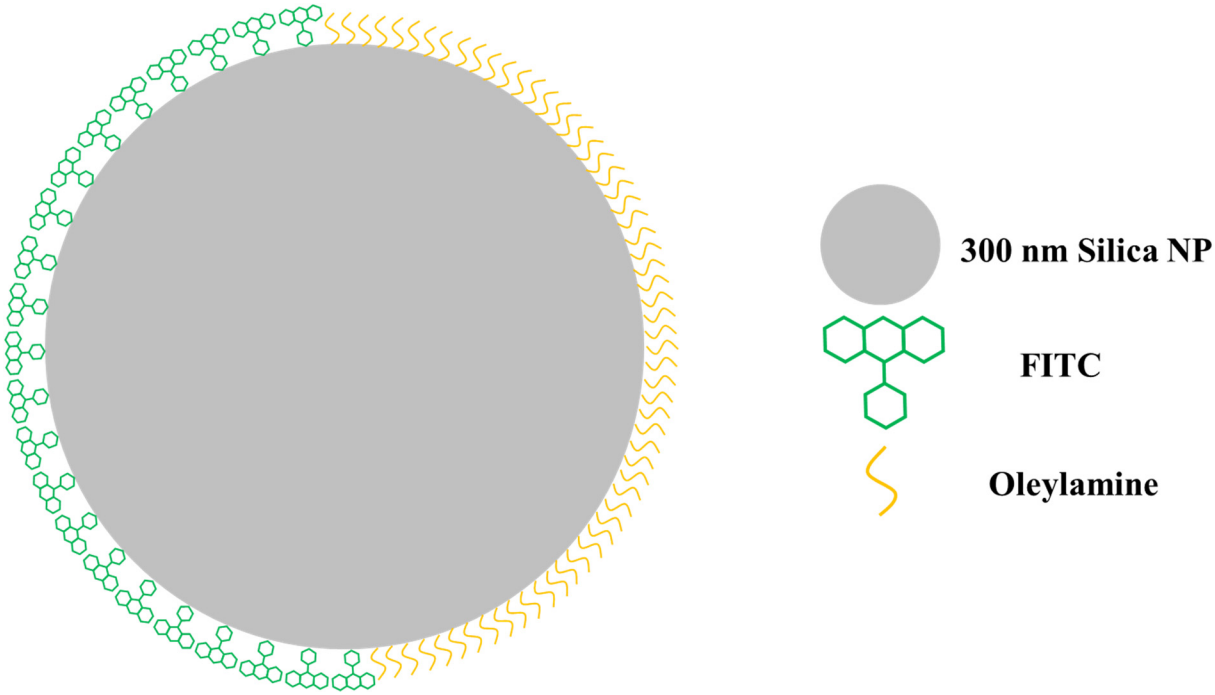

Figure 3.7: Illustration of OLE-Si-FITC: silica core with regions composed of oleylamine and FITC

3.2.4: Synthesizing two-sided silica nanoparticles in a C_{18} Bead Packed Column

A 6 mL column was loaded with 5 grams of C_{18} beads. 10.0% stearylamine in ethanol by volume was added to the column (sealed) and allowed adsorb to the stationary phase for 15 minutes. The solution was drained and the column was washed with a 10.0% methanol/water solution and then with water. 25.0% glutaraldehyde in 20 mM HEPES buffer (pH: 7.5) by volume was added to the column (sealed) and allowed to react for 1 hour, followed by a water washing step. 300 nm silica nanoparticles were added to the column (sealed) and allowed to react for 1 hour, followed by a water washing step. mPEG-NHS (MW 5000) was dissolved in equal parts DMSO and 20 mM HEPES buffer and added to the column; 4 hours of reaction time was allowed followed by a water washing step. 4 silica configurations were prepared by reacting FITC and/or RHOB to the nanoparticles. SA+FITC-Si-PEG+FITC, SA+RHOB-Si-PEG+RHOB, SA+FITC+RHOB-Si-PEG+FITC+RHOB configurations were eluted from the column using chloroform and reacted with dye molecules for 12 hours. SA+RHOB-Si-PEG+FITC nanoparticles were reacted with FITC in ethanol while adsorbed to the stationary phase material for 12 hours. The column was washed with water, nanoparticles were eluted using chloroform, and reacted with RHOB for 12 hours. Solvent was removed from the all nanoparticle samples using a rotary evaporator; nanoparticles were resuspended in ethanol and washed using centrifugation. Functionalized nanoparticles were stored in chloroform. Table 3.2 gives the names and structures of each configuration; illustrations of each configuration are shown in Figures 3.8-3.12:

Table 3.2: Descriptions of Silica Nanoparticle Configurations Prepared in a C_{18} Bead Packed Column

Name	M1 Compound	Additional M1 Compound	Crosslinker	NP	M2 Compound	Additional M2 Compound
SA-Si-PEG	Stearylamine	--------	Glutaraldehyde	Silica	mPEG-NHS	--------
SA+FITC-Si-PEG+FITC	Stearylamine	FITC	Glutaraldehyde	Silica	mPEG-NHS	FITC
SA+RHOB-Si-PEG+RHOB	Stearylamine	RHOB	Glutaraldehyde	Silica	RHOB	RHOB
SA+FITC+RHOB-Si-PEG+FITC+RHOB	Stearylamine	FITC/RHOB	Glutaraldehyde	Silica	mPEG-NHS	FITC/RHOB
SA+RHOB-Si-PEG+FITC	Stearylamine	RHOB	Glutaraldehyde	Silica	mPEG-NHS	FITC

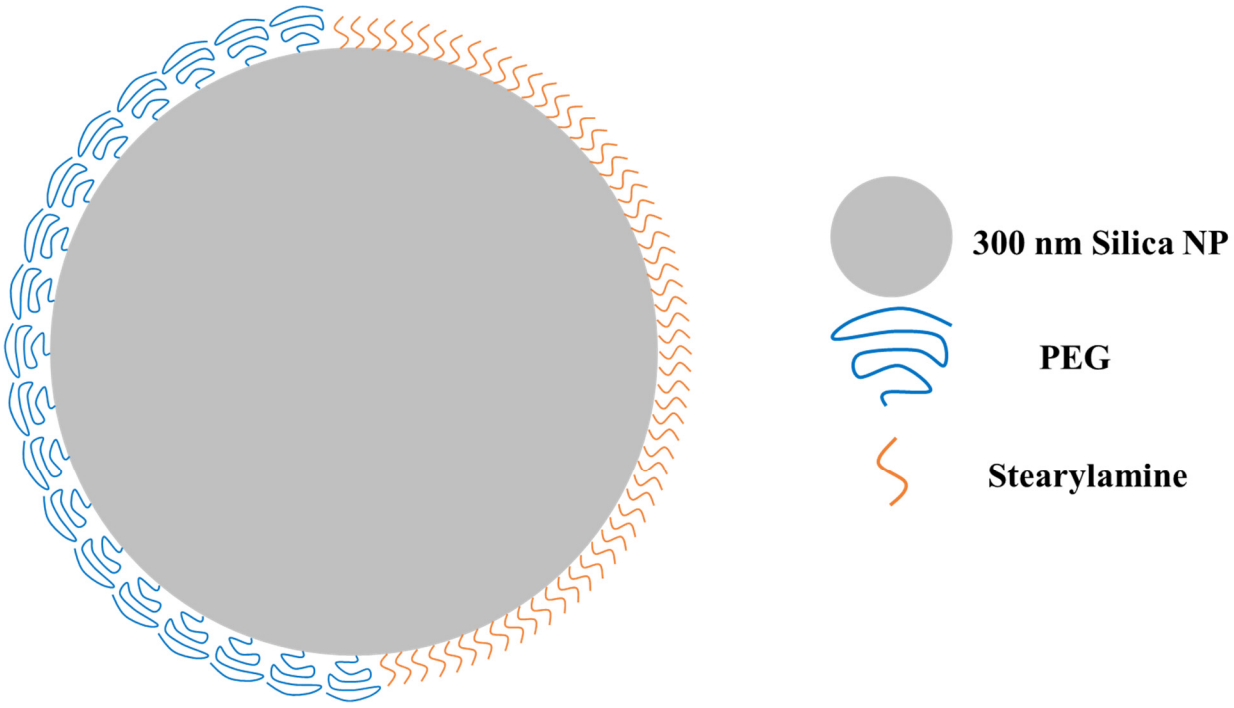

Figure 3.8: Illustration of SA-Si-PEG: silica core with regions composed of stearylamine and mPEG-NHS

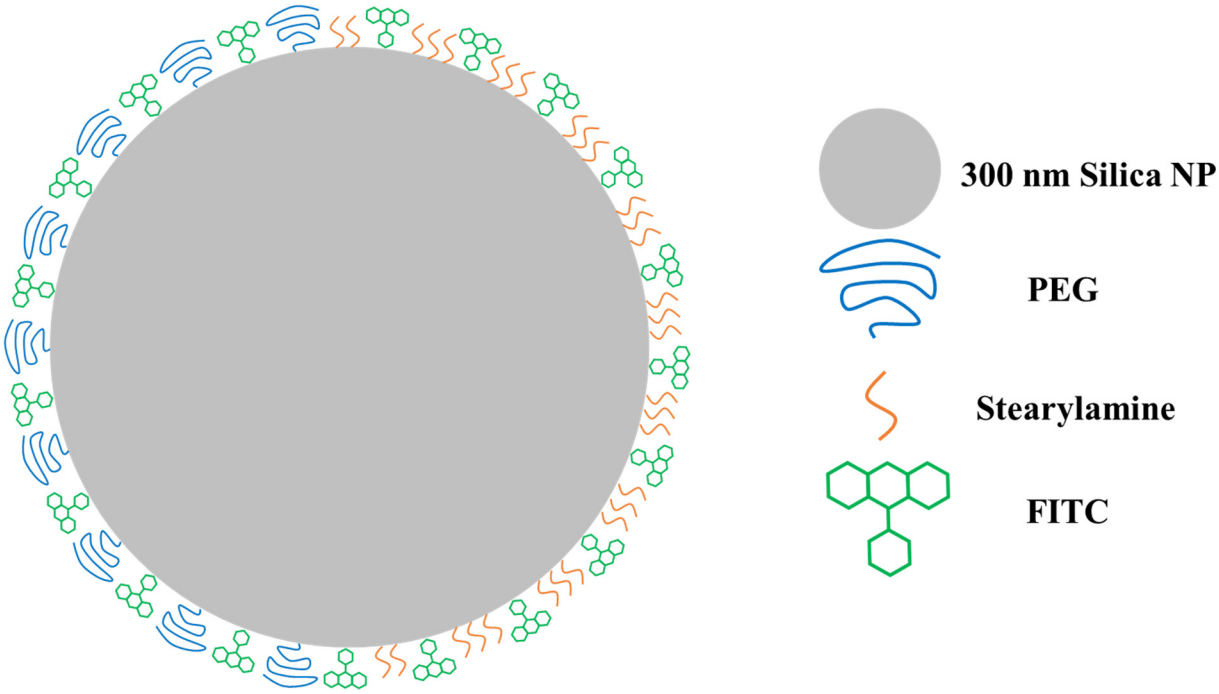

Figure 3.9: Illustration of SA+FITC-Si-PEG+FITC: silica core with regions composed of stearylamine/FITC and mPEG-NHS / FITC

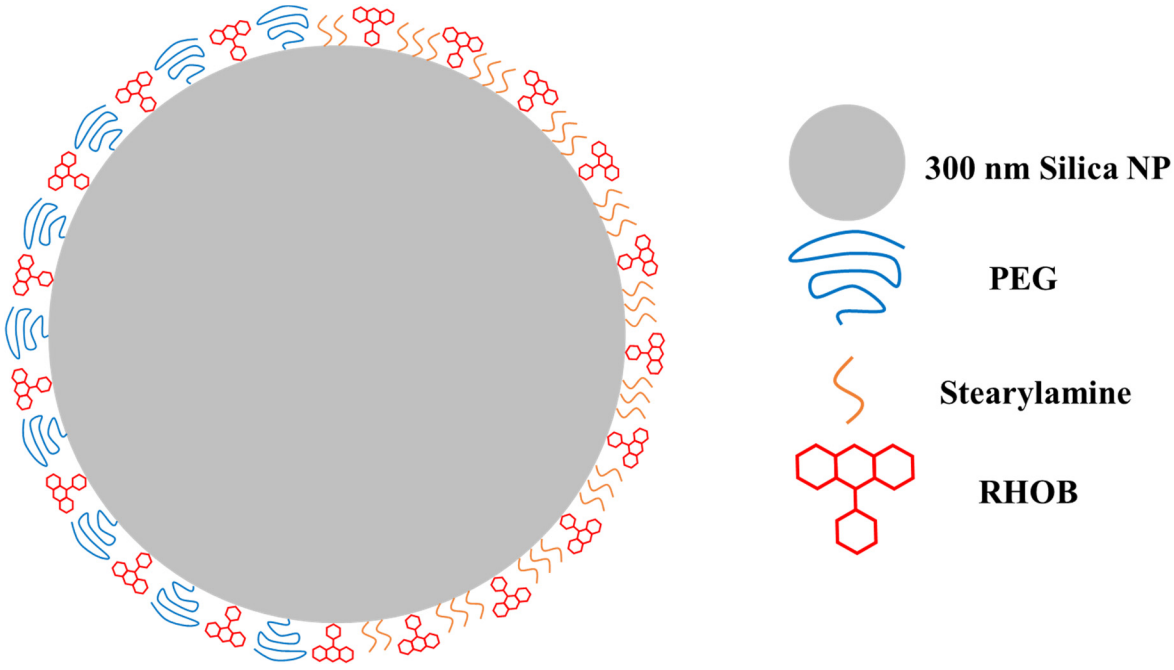

Figure 3.10: Illustration of SA+RHOB-Si-PEG+RHOB: silica core with regions composed of stearylamine/RHOB and mPEG-NHS / RHOB

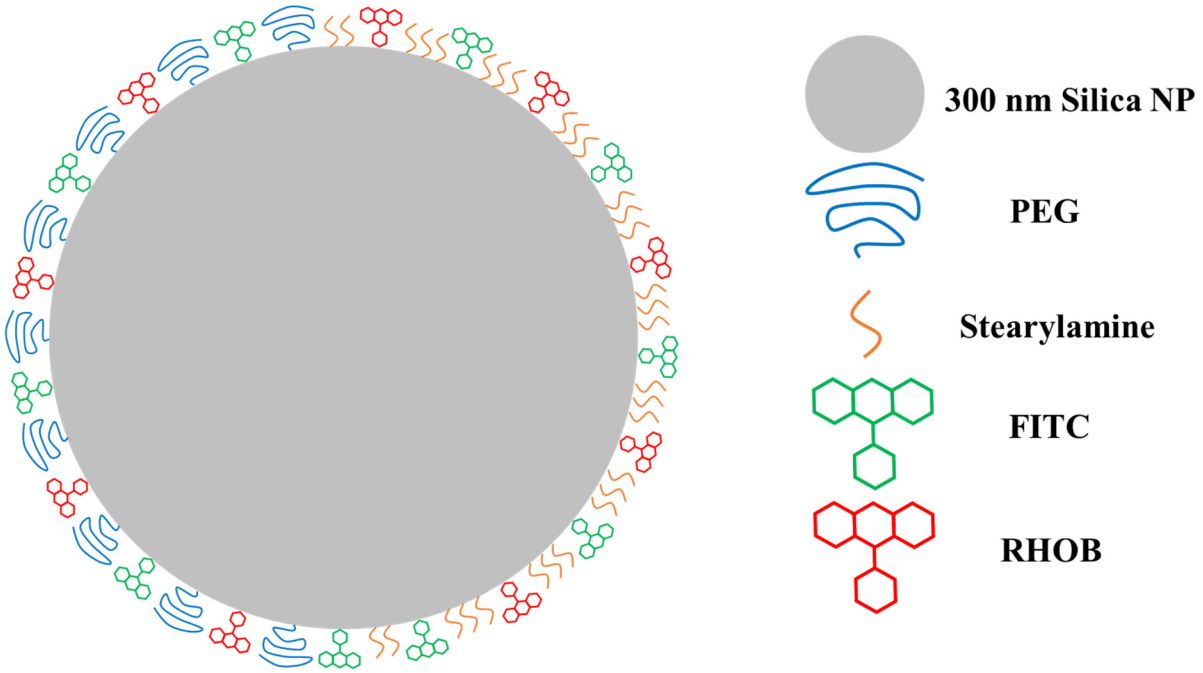

Figure 3.11: Illustration of SA+FITC+RHOB-Si-PEG+FITC+RHOB: silica core with regions composed of stearylamine/FITC/RHOB and mPEG-NHS/FITC/RHOB

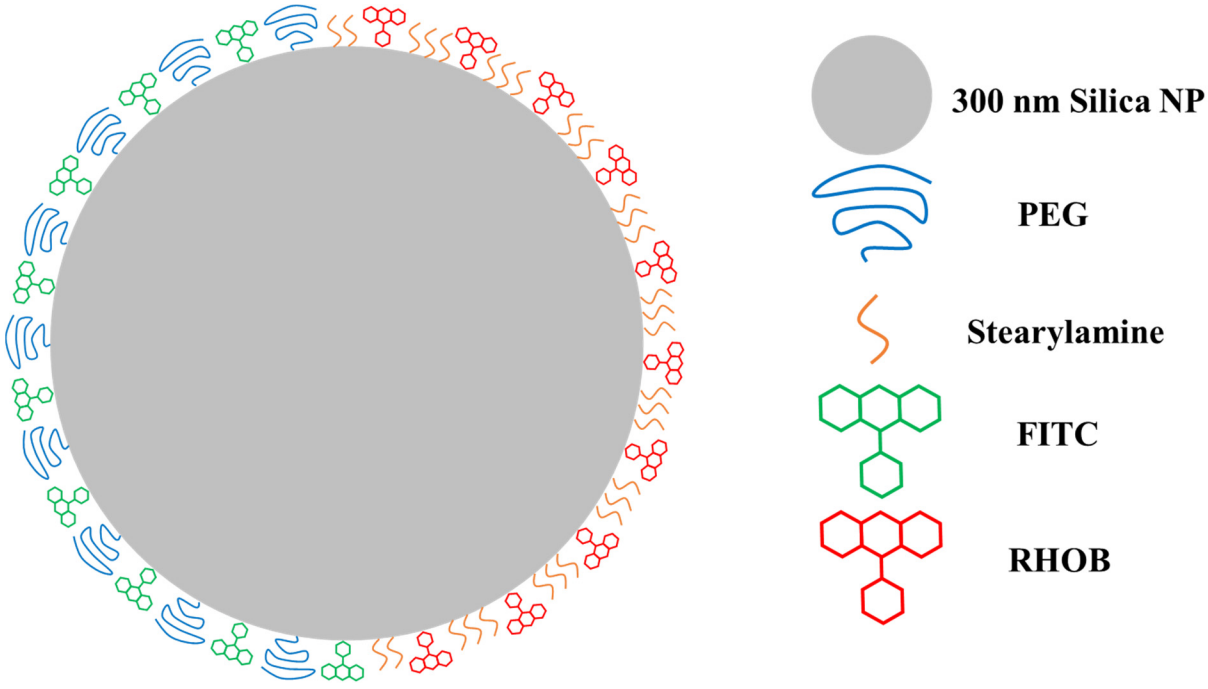

Figure 3.12: Illustration of SA+RHOB-Si-PEG+FITC: silica core with regions composed of stearylamine/RhoB and mPEG-NHS/FITC

3.2.5: Synthesizing Silica CPs

Oleylamine coated Silica Nanoparticles (OLESiCPs): 300 nm Silica nanoparticles were added to 25.0% glutaraldehyde in 20 mM HEPES buffer (pH: 7.5) and allowed to react for 1 hour with agitation. Nanoparticles were removed from the solvent via centrifugation and resuspended in 1 mL of 25.0% glutaraldehyde in 20 mM HEPES buffer for 1 hour with agitation. Nanoparticles were removed from the solvent via centrifugation and resuspended in 1 mL of 10% oleylamine in ethanol for 2 hours with agitation. Nanoparticles were washed in hexane using centrifugation and stored in hexane.

Stearylamine coated Silica Nanoparticles (SASiCPs): 300 nm Silica nanoparticles were added to 25.0% glutaraldehyde in 20 mM HEPES buffer (pH: 7.5) by volume and allowed to react for 1 hour with agitation. Nanoparticles were removed from the solvent via centrifugation and resuspended in 1 mL of 25.0% glutaraldehyde in 20 mM HEPES buffer for 1 hour with agitation. Nanoparticles were removed from the solvent via centrifugation and resuspended in 1 mL of 10% stearylamine in ethanol for 2 hours with agitation. Nanoparticles were washed in hexane using centrifugation and stored in hexane.

PEGylated Silica Nanoparticles (PEGSiCPs): 300 nm silica nanoparticles were combined with 30 mg of mPEG-NHS (MW 5000) in equal parts DMSO and 20 mM HEPES buffer (pH: 7.5). Components were allowed to react for 4 hours. Nanoparticles were washed in water using centrifugation and stored in water.

CAION coated Silica Nanoparticles (CASiCPs): CAIONs in water were activated with NHS and EDC and combined with 300 nm silica nanoparticles in water. The reaction was allowed to occur for 1 hour. Nanoparticles were washed in water using centrifugation and resuspended in water. NHS and EDC were added to the nanoparticles and allowed to react for 15 minutes. mPEG-NH_2 was added to the sample and allowed to react for an additional hour. Nanoparticles were washed in water using centrifugation and stored in water.

CAION/Oleylamine coated Silica Nanoparticles (CAOLESiCPs): 300 nm silica nanoparticles in water were combined with a 25.0% glutaraldehyde in 20 mM HEPES buffer (pH: 7.5) by volume and CAIONs activated with NHS and EDC. The reaction was allowed to occur for 2 hours, then nanoparticles were washed in water using centrifugation. Nanoparticles were

resuspended in chloroform; EDC and NHS were added to the nanoparticles and allowed to react for 15 minutes. Oleylamine and mPEG-NH_2 were added to the nanoparticle sample and allowed to react for 1 hour. Nanoparticles were washed in chloroform using centrifugation and stored in chloroform.

3.2.6: Preparing C_{18} Beads

C_{18} beads were prepared based on the method published by Arslan et al. 25 grams of borosilicate glass beads were washed in KOH. KOH was removed, and the beads were washed in water. Washed beads were dried using nitrogen until bone dry. Beads were submerged in a mixture of 3.928 mL octadecatrimethoxysilane and 200 mL of toluene and allowed 1 hour for reaction in a continuously stirred vessel. Solvent was removed, and beads were washed in toluene. Beads were dried under a nitrogen blanket until bone dry.[105]

3.3: Results and Discussion

3.3.1: Results for OLE-Si-CAION+PEG

Surface modifications on OLE-Si-CAION+PEG nanoparticles and CPs were confirmed using FTIR. A peak between 1000 cm^{-1} and 1200 cm^{-1} was present in all spectrums; this peak indicated a carbon-oxygen bond stretch in previous data, but also refers to a silicon-oxygen bond stretch from the silica nanoparticles.[83] Stronger peaks at this wavelength were seen in PEGSiCPs, CASiCPs, CAOLESiCPs, and OLE-Si-CAION+PEG spectrums. Methyl and methylene peaks (2900 cm^{-1}) were seen in the OLESiCPs, CAOASiCPs, and OLE-Si-CAION+PEG spectrums. Spectrums are found in Figure 3.13:

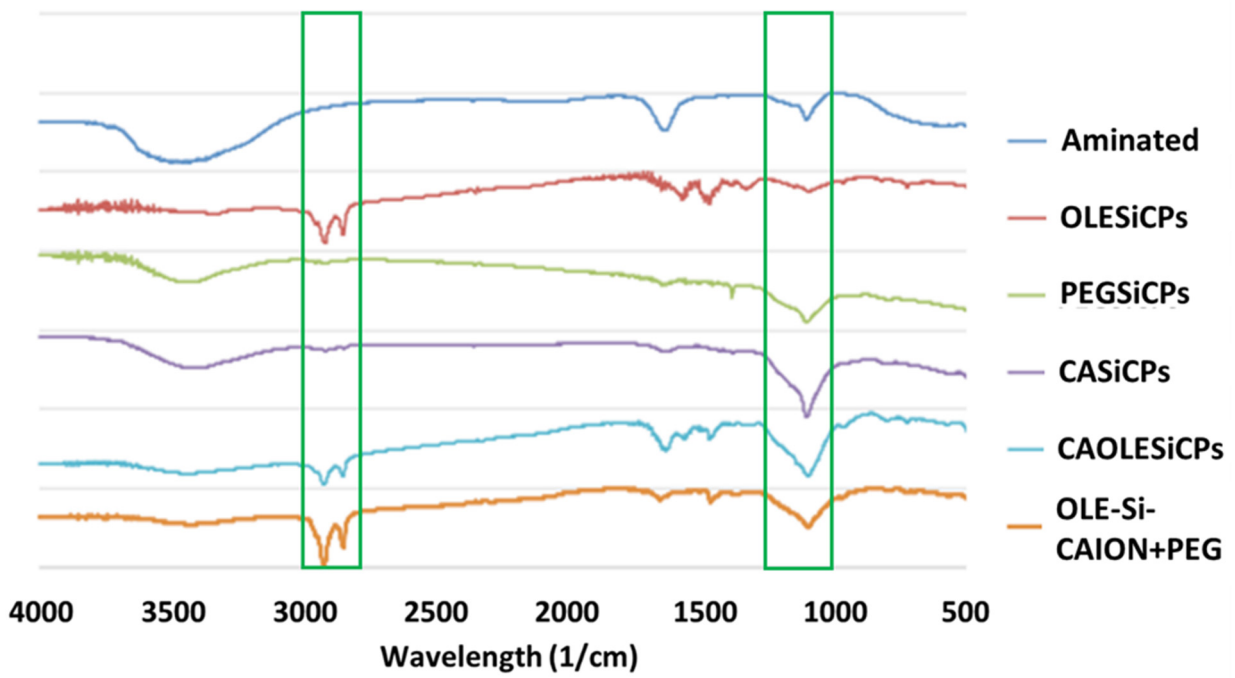

Figure 3.13 FTIR spectrums (wavelength vs. % transmittance) for (top to bottom): unmodified aminated silica nanoparticles (dark blue), OLESiCPs (red), PEGSiCPs (green), CASiCPs (purple), CAOLESiCPs (light blue), and OLE-Si-CAION+PEG (orange)

From Figure 3.1, 20 nm iron oxide nanoparticles and 300 nm silica nanoparticles were both visible when examined using TEM. Considering the size of oleylamine and PEG molecules, it was assumed that these molecules would not be visible on the surface of silica nanoparticles when examined using TEM; this assumption was verified by images of PEGylated silica nanoparticles found in published literature.[106] Due to these factors, it was proposed that regions of oleylamine and CAIONs would be visibly different on silica nanoparticle surfaces when examined using TEM. To test this hypothesis, TEM imaging was used to visually examine individual nanoparticles from samples of PEGSiCPs, OLESiCPs, CASiCPs, CAOLESiCPs, and OLE-Si-CAION+PEG. TEM images of CPs are shown in Figure 3.14; images of OLE-Si-CAION+PEG nanoparticles are shown in Figures 3.15:

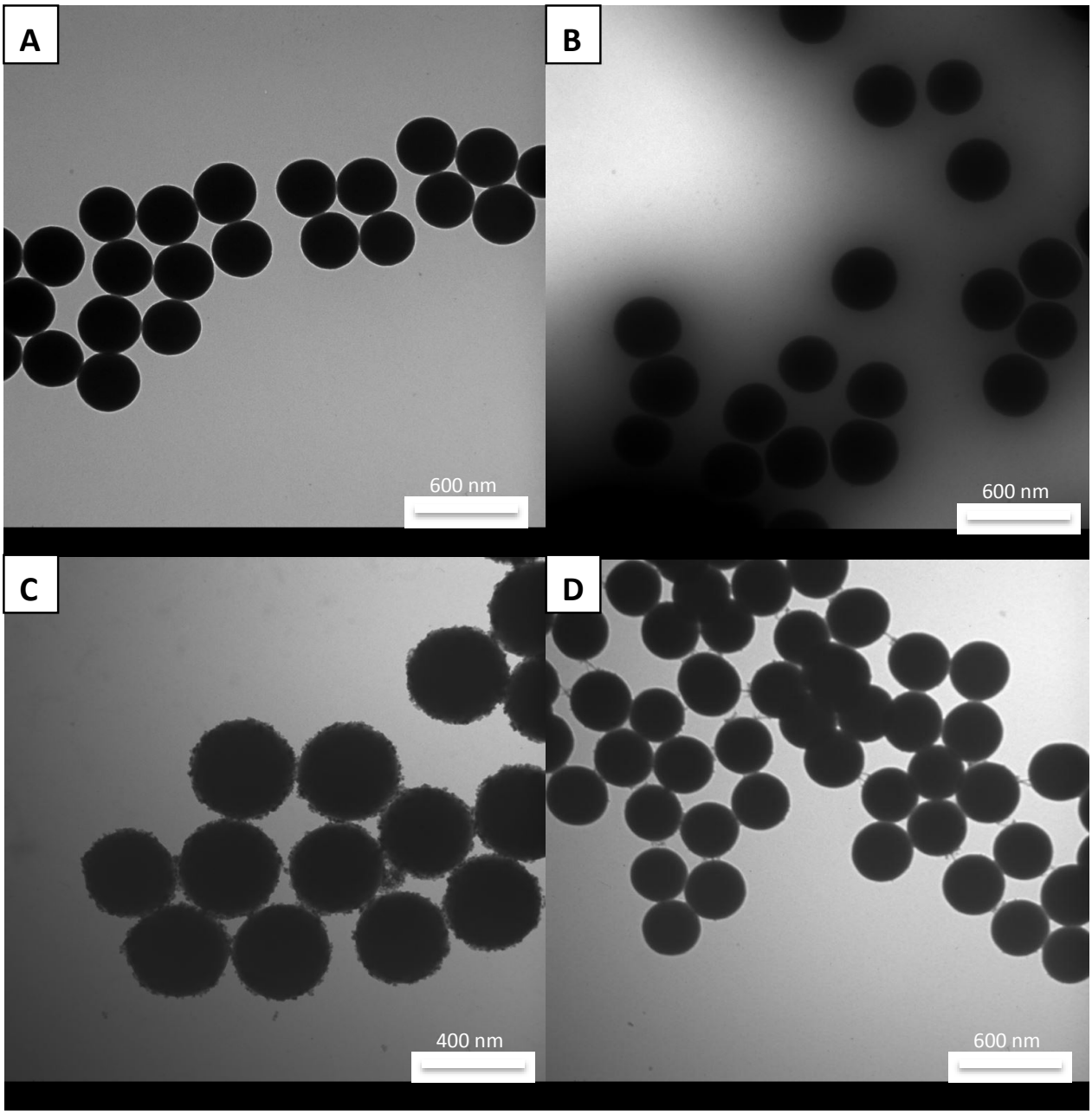

Figure 3.14: TEM images of (A) PEGSiCPs, (B) OLESiCPs, (C) CASiCPs, and (D) CAOLESiCPs

From Figure 3.14, nanoparticles in (A) and (B) have smooth surfaces. Oleylamine and mPEG-NHS 5000 cannot be seen using TEM due to their size even at high magnification[107,108]; nanoparticles with these surface compounds look similar to unmodified silica nanoparticles like the nanoparticles shown in Figure 3.1. CASiCPs in (C) had a visible surface coating of CAIONs;

CAOLESiCPs in (D) also showed CAION surface bonding, but with fewer visible iron oxide nanoparticles on the silica surface. This visual difference between oleylamine coatings and CAION coatings was used to differentiate between regions on the surface of OLE-Si-CAION+PEG nanoparticles.

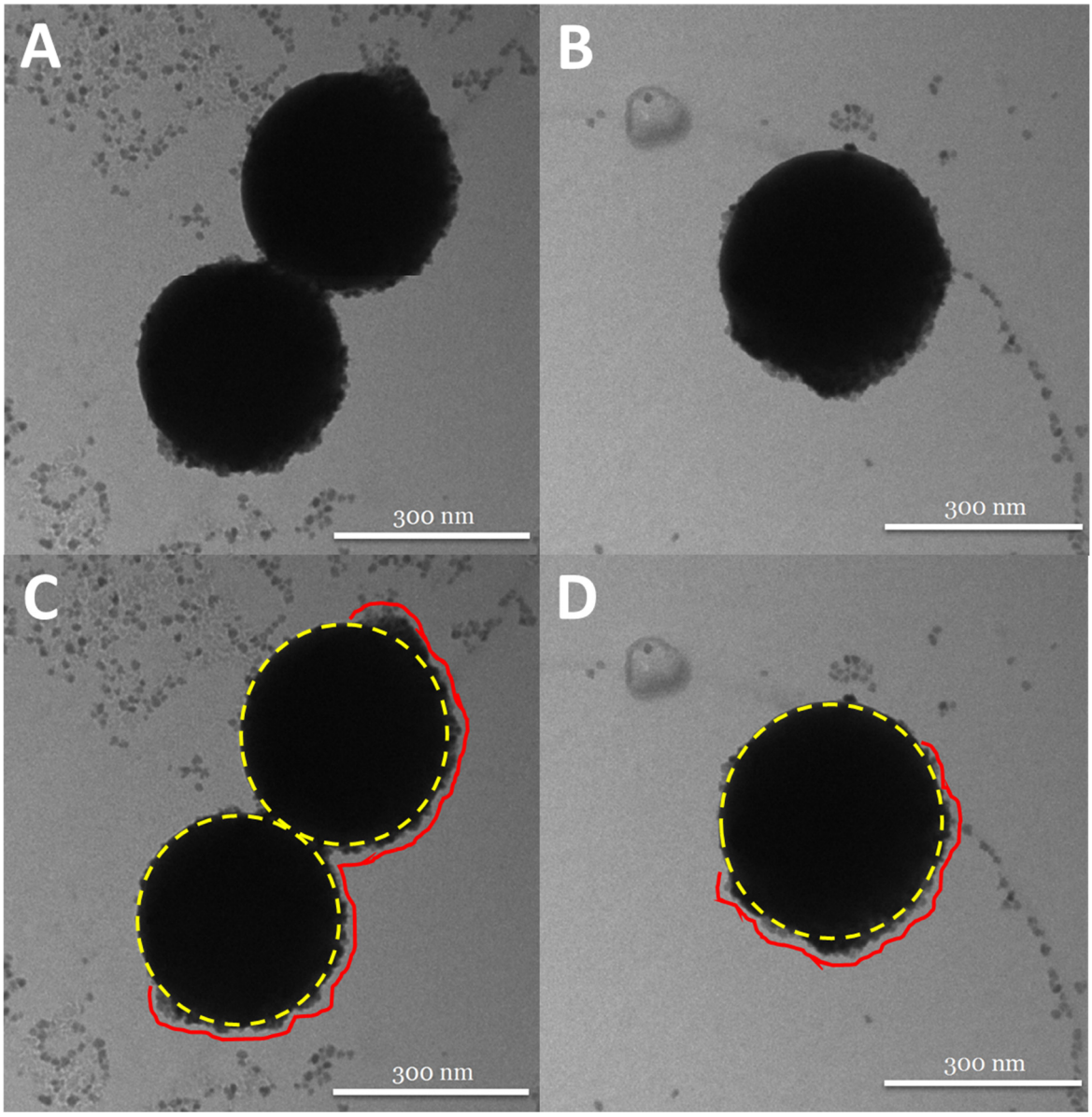

Figure 3.15: A/B: TEM images of OLE-Si-CAION+PEG nanoparticles. C/D: Images A and B with added graphics indicating regions of CAION surface modifications (red) and the circumference of the silica nanoparticle (yellow)

Regions of CAIONs (rough region) and oleylamine (smooth regions) were seen on nanoparticles in Figures 3.15. From Figure 3.15, image A, nanoparticles had rough regions from 30 degrees right of top center position to 210 degrees right of top center. In Figure 3.15, image B, the rough region stretched from 60 degrees right of top center position to 240 degrees right of top center. Perro et al. produced similar TEM images to Figure 3.15; 100 nm and 150 nm silica nanoparticles were selectively modified with 10-20 nm gold nanoparticles.[45] TEM images from Perro et al are shown in Figure 3.16 for comparison. By comparing the nanoparticles seen in Figure 3.15 to CP nanoparticles shown in Figure 3.14 and anisotropic nanoparticles produced by Perro et al. (Figure 3.16), creation of regionally specific surface modifications on OLE-Si-CAION+PEG nanoparticles was confirmed .

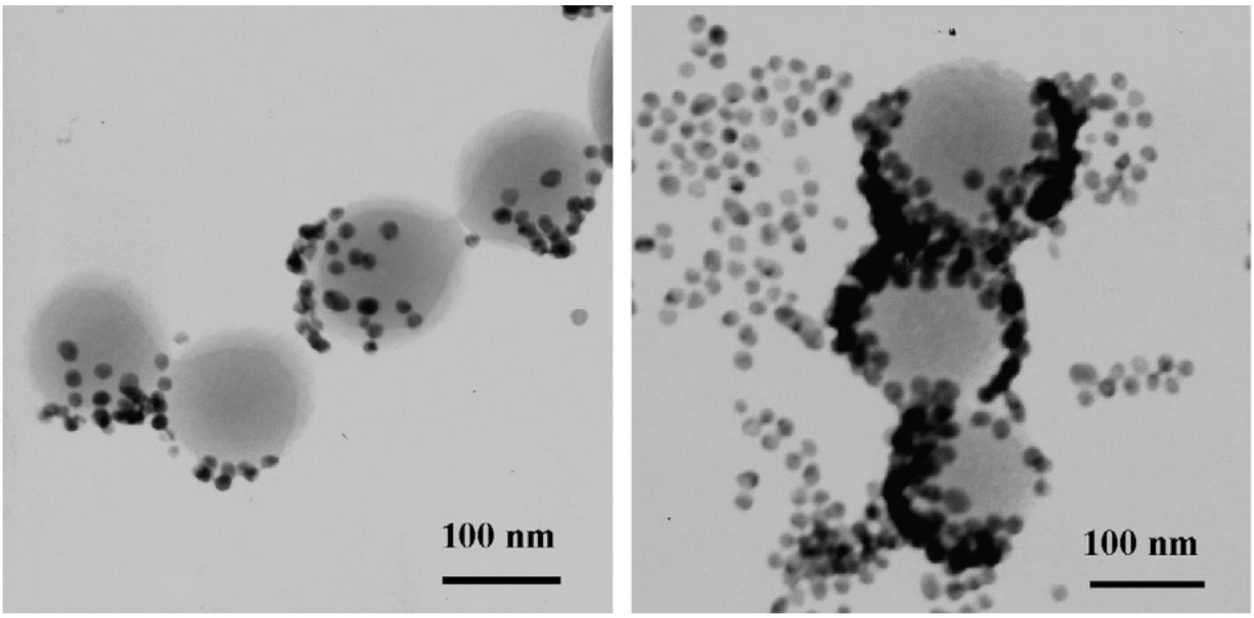

Figure 3.16: TEM images from Perro et al of 100 nm and 150 nm silica nanoparticles selectively modified with 10-20 nm gold nanoparticles. Reprinted with permission from Perro et al, 2009 with permission from Elsevier.

3.3.2: Results for OLE-Si-PEG and OLE-Si-FITC

To verify the results from 3.3.1, it was proposed that differing nanoparticle surface regions could be identified using fluorescent dyes. By reacting a fluorescent dye to a region of the nanoparticle surface, optical fluorescent microscopy could be used to visualize opposing regions. To test this hypothesis, OLE-Si-PEG and OLE-Si-FITC nanoparticles were examined using an optical microscope equipped with fluorescent filters. Recall that OLE-Si-PEG has regions of oleylamine and PEG (no fluorescence) and OLE-Si-FITC has regions of oleylamine and FITC (fluorescent, absorbance peak: 492 nm, emission peak 518 nm)[109]; FITC is detectable when using a Green Fluorescent Protein fluorescent filter (GFP)[110]. Optical microscope images of these nanoparticles are shown in Figures 3.17 and 3.18:

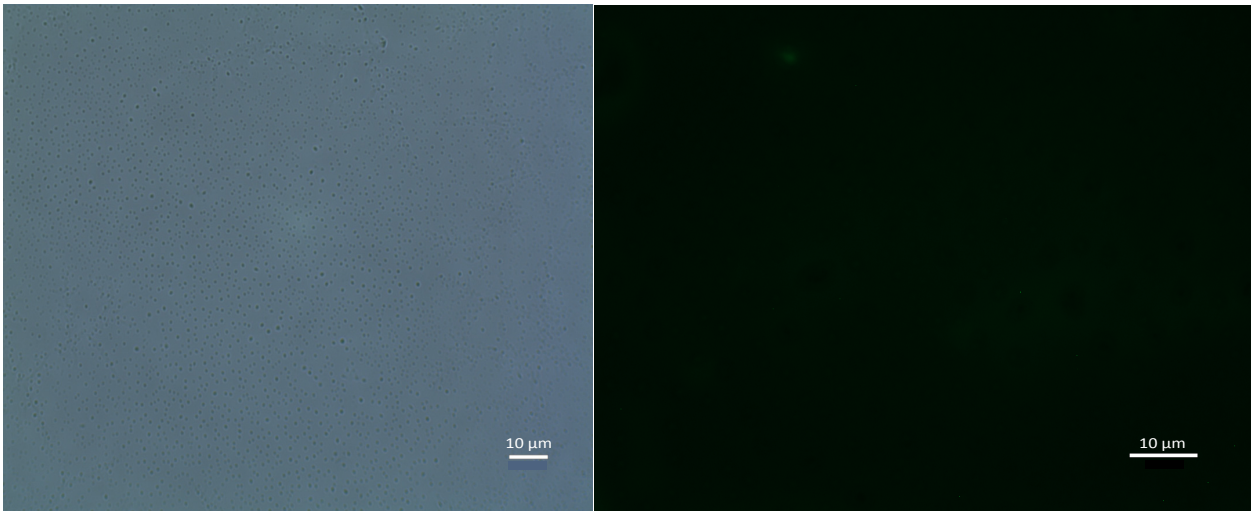

Figure 3.17: (left) Brightfield image OLE-Si-PEG nanoparticles; (right) GFP filtered image of the same OLE-Si-PEG nanoparticles

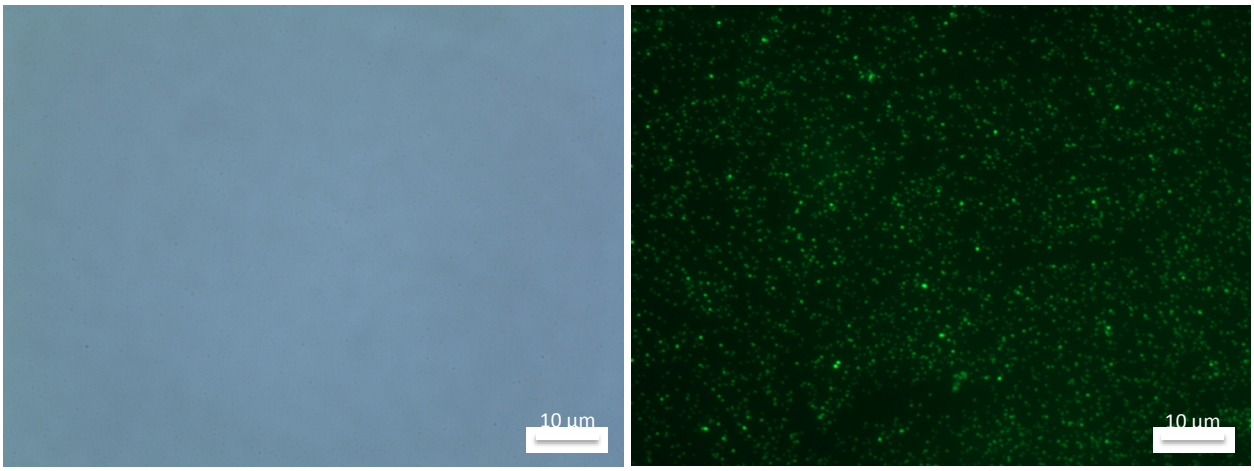

Figure 3.18: (left) Brightfield image OLE-Si-FITC nanoparticles; (right) GFP filtered image of the same OLE-Si-PEG nanoparticles

From Figure 3.17, nanoparticles were visible under brightfield light but not when the fluorescent filter is applied. In Figure 3.18, nanoparticles were clearly visible in both images, confirming attachment of FITC to the nanoparticle surface. With FITC attachment confirmed, the next step was to identify if FITC occupied a specific region of the nanoparticles surface or if it was evenly distributed. Due to these limitations, OLE-Si-PEG and OLE-Si-FITC were examined under a different optical microscope equipped with a dark field condenser. Dark-field condensers increase the contrast of materials by directing unscattered light away from the detector. Scattered light, or specifically light that hits the sample material, is the only light detected; the result is an image with a dark background and bright sample materials.[111] Published literature indicates that the microscope used in our studies can produce clear images of 90 nm structures by using a dark-field condenser in place of the standard bright-field condensor.[112] Dark-field images of OLE-Si-FITC nanoparticles taken with and without a fluorescent filter were overlain to determine if FITC was specific to one region of the nanoparticle surface. Images of OLE-Si-PEG and OLE-Si-FITC using this setup are shown in Figures 3.19-3.20:

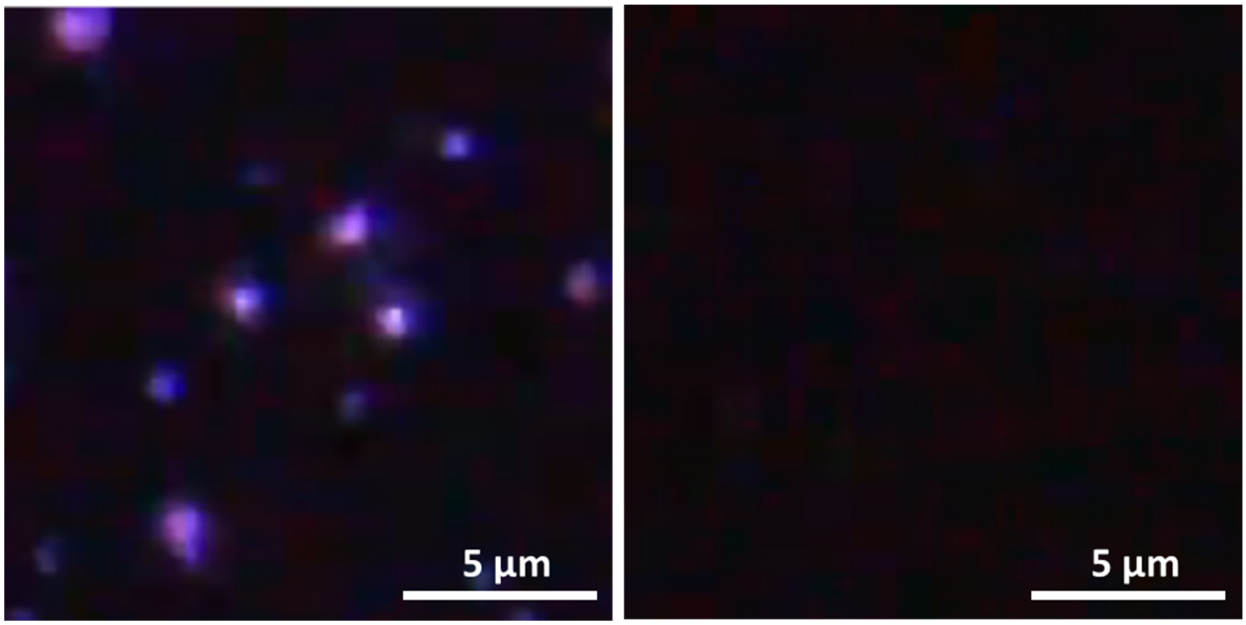

Figure 3.19: Dark-field images of OLE-Si-PEG without a fluorescent filter (left) and with a fluorescent filter (right)

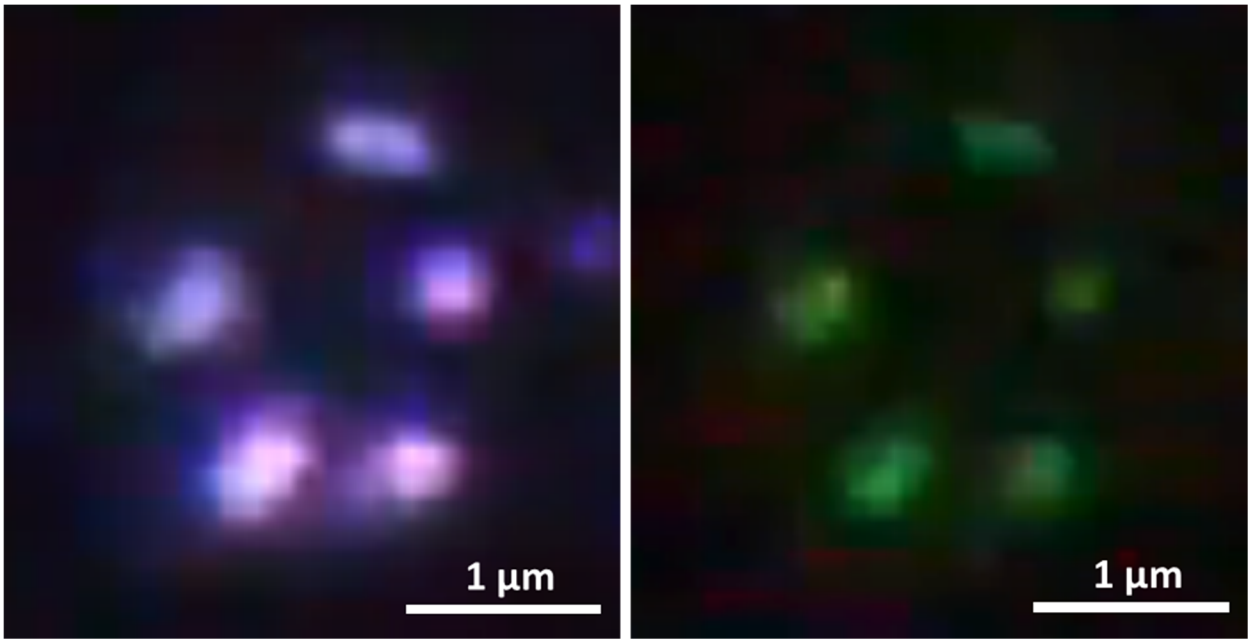

Figure 3.20: Dark-field images of OLE-Si-FITC without a fluorescent filter (left) and with a fluorescent filter (right)

Images that employ the fluorescent filter produced the same results in Figures 3.22 and 3.23 as in Figures 3.20 and 3.21, respectively; OLE-Si-PEG nanoparticles were not visible when the filter was applied. Conversely, OLE-Si-FITC was visible and appears green when using the fluorescent filter. Resolution on this microscope allowed magnifications to single-micron scale before images become overly pixelated. At this magnification, images from Figure 3.23 were overlain to identify differing surface regions. The overlain image is shown in Figure 3.21:

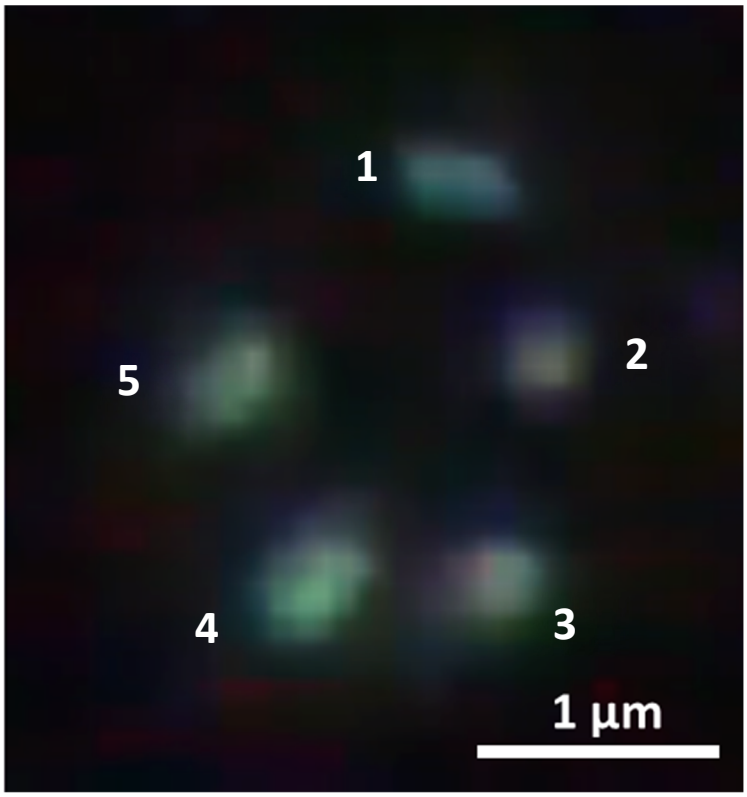

Figure 3.21: Overlain image of dark-field images from Figure 3.20

From the overlay, separation of purple and green color was seen on individual nanoparticles. The best separation was seen on nanoparticle 3 with green color localized to the right side of the nanoparticle. Orientation of the nanoparticles on the slide and the anisotropic surface ratio will alter the visible separation of colors when using this imaging method; these factors explain the variance in color separation between nanoparticles. While some separation was seen in Figure 3.21, this image was not conclusive in confirming different regions of FITC and oleylamine. These

results led to a modification of the hypothesis stated at the beginning of this section; it was proposed that the opposing regions of two-sided nanoparticles could be visualized if regions were modified with two fluorescent dyes with different absorbance and emission peaks using optical fluorescent microscopy. To test this hypothesis, images of nanoparticles with two dyes would be taken using different fluorescent filters (each dye is specific to one filter and not visible when the other filter is utilized); images would then be overlain to examine where certain dyed molecules had reacted to the nanoparticle surface.

3.3.3: Results for SA+FITC-Si-PEG+FITC, SA+RHOB-Si-PEG+ RHOB, SA+FITC+RHOB-Si-PEG+FITC+RHOB, and SA+RHOB-Si-PEG+FITC configurations

SA+FITC-Si-PEG+FITC, SA+RHOB-Si-PEG+ RHOB, SA+FITC+RHOB-Si-PEG+FITC+RHOB, and SA+RHOB-Si-PEG+FITC were examined using an optical microscope. FITC coated configurations and RhoB coated configurations were detectable using GFP and red fluorescent protein (RFP, excitation range: 511-551 nm, emission range: 553-633 nm)[110] filters, respectively. Filtered and overlain images of SA+FITC-Si-PEG+FITC, SA+RHOB-Si-PEG+RHOB and SA+FITC+RHOB-Si-PEG+FITC+RHOB nanoparticles are shown in Figure 3.22:

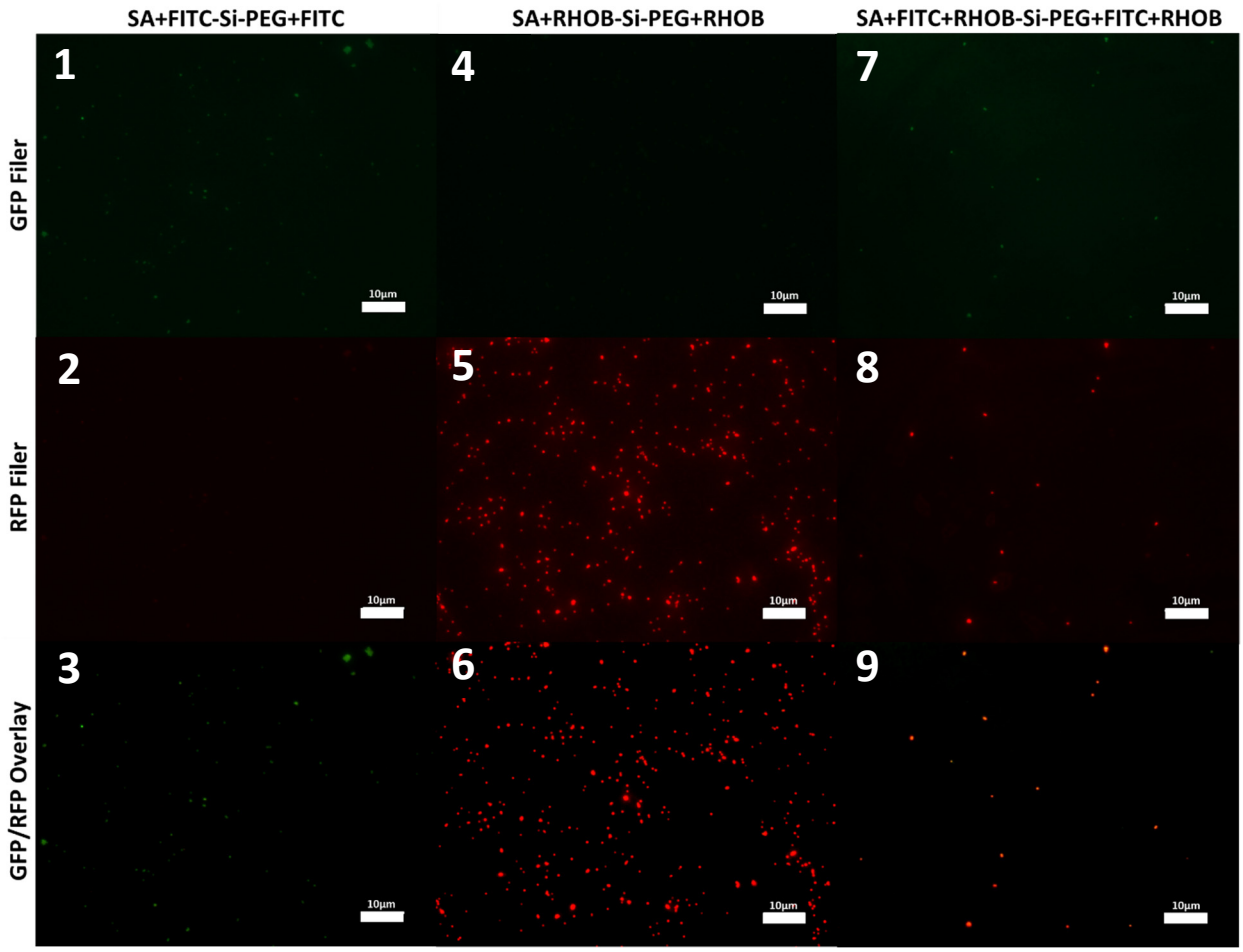

Figure 3.22: Optical microscope images of SA+FITC-Si-PEG+FITC (1,2,3), SA+RHOB-Si-PEG+RHOB (4,5,6), and SA+FITC+RHOB-Si-PEG+FITC+RHOB (7,8,9) using GFP and RFP filters and GFP/RFP Overlay images

From Figure 3.22, SA+FITC-Si-PEG+FITC nanoparticles (images 1-3) were visible when using the GFP filter but not the RFP filter. SA+RHOB-Si-PEG+RHOB nanoparticles (images 4-6) were visible using the RFP filter but not the GFP filter. SA+FITC+RHOB-Si-PEG+FITC+RHOB nanoparticles had FITC and rhodamine B on the surface making nanoparticles visible using either filter. The overlain image for SA+FITC+RHOB-Si-PEG+FITC+RHOB nanoparticles (image 9) showed nanoparticles with yellow centers surrounded by red. The yellow center indicated FITC and RHOB attached to the nanoparticle surface in nonspecific areas (randomly distributed). Red color surrounding the center was either due to a larger quantity of RHOB on the nanoparticle surface or better compatibility between RHOB dye and the RFP filter when compared to FITC dye

and the GFP filter. RHOB has an absorbance peak (543 nm) and emission peak (580 nm) that fall within the RFP filters excitation and emission ranges, respectively.[113] While FITC can be detected using the GFP filter[110], its absorbance peak is above the excitation range for the GFP filter.[109] Essentially, excitation of FITC molecules was not maximized due to removal of certain wavelengths of light be the GFP filter that could have excited FITC. This issue may account for the difference in intensity between FITC and RHOB in Figure 3.22 since this absorbance peak/excitation range difference did not occur between RHOB and the RFP filter. After examining overlain images in Figure 3.22, images of SA+RHOB-Si-PEG+FITC nanoparticles were taken to produce GFP/RFP overlays for comparison. Images of SA+RHOB-Si-PEG+FITC nanoparticles from the optical microscope are shown in Figure 3.23; digitally zoomed in sections of the overlain image (bottom) in Figure 3.23 are shown in Figure 3.24:

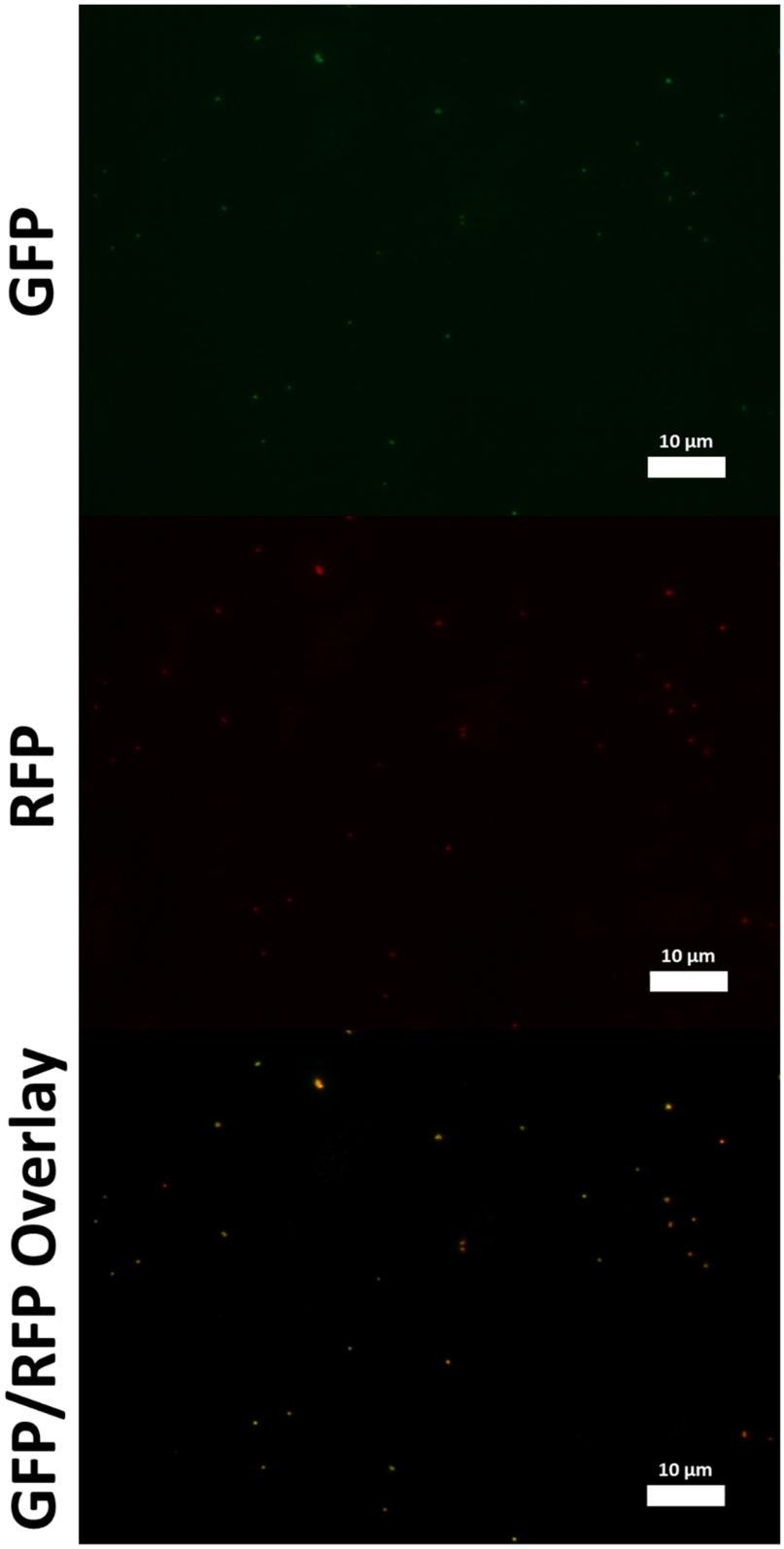

Figure 3.23: Optical microscope images of SA+RHOB-Si-PEG+FITC nanoparticles using GFP (top) and RFP (middle) filters and an overlay of those images (bottom)

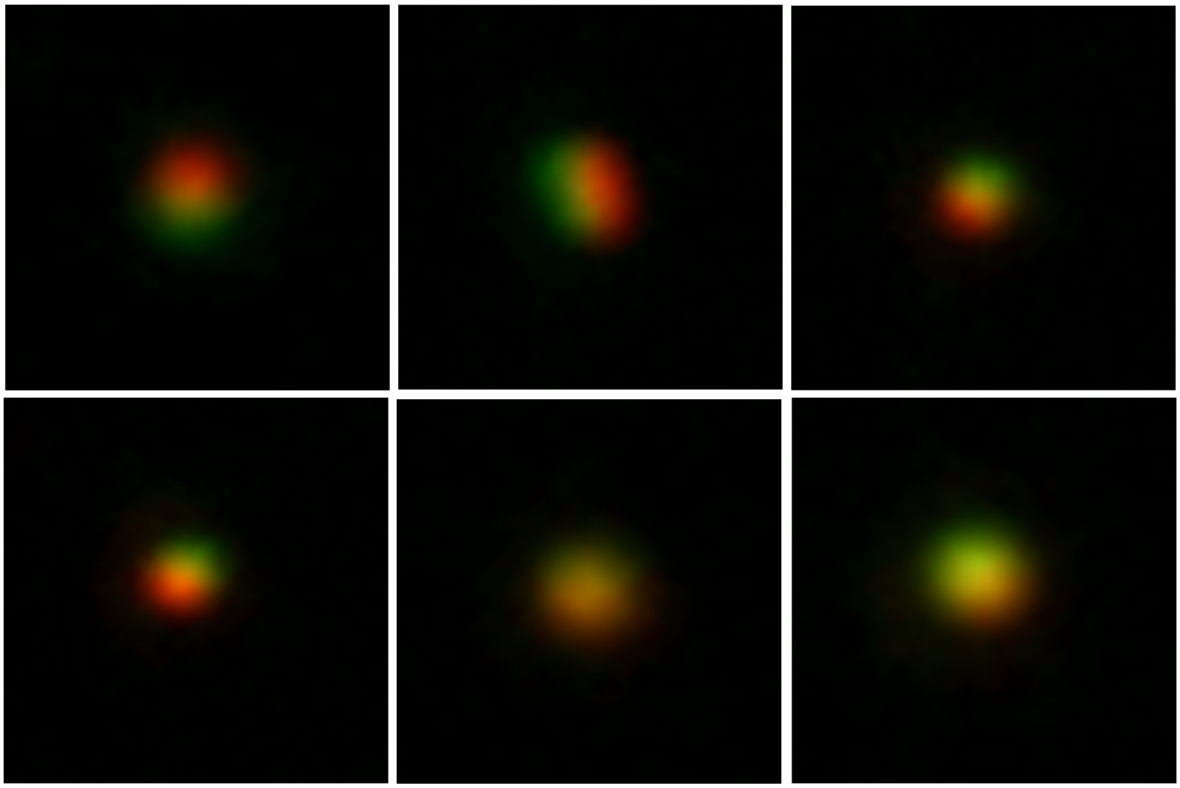

Figure 3.24: Zoomed in sections of overlain images of SA+RHOB-Si-PEG+FITC nanoparticles

Due to the presence of both dyes on the surface, SA+RHOB-Si-PEG+FITC nanoparticles were detectable using GFP and RFP filters. When GFP and RFP images were overlain, nanoparticles composed of green, yellow, and red ae visible (Figure 3.23, bottom image); these colors were seen more clearly in the zoomed in images in Figure 3.24. Unlike the nanoparticles seen in Figure 3.22, image 9, green and red were visible on opposing sides of the nanoparticle. Ratio of red to green color seen on SA+RHOB-Si-PEG+FITC nanoparticles varied; the anisotropic surface ratio and the orientation of the nanoparticles on the slide was likely the reason for this result. Similar images have been reported by Xie et al, who produced polymeric Janus nanoparticles with differing regions of Nile Red and RH-6g dyes. Images of Xie et al.'s nanoparticles are shown in Figure 3.25. Images in Figure 3.24 indicate localization of dyes to opposing regions on the nanoparticles surface and the successful synthesis of JNPs.

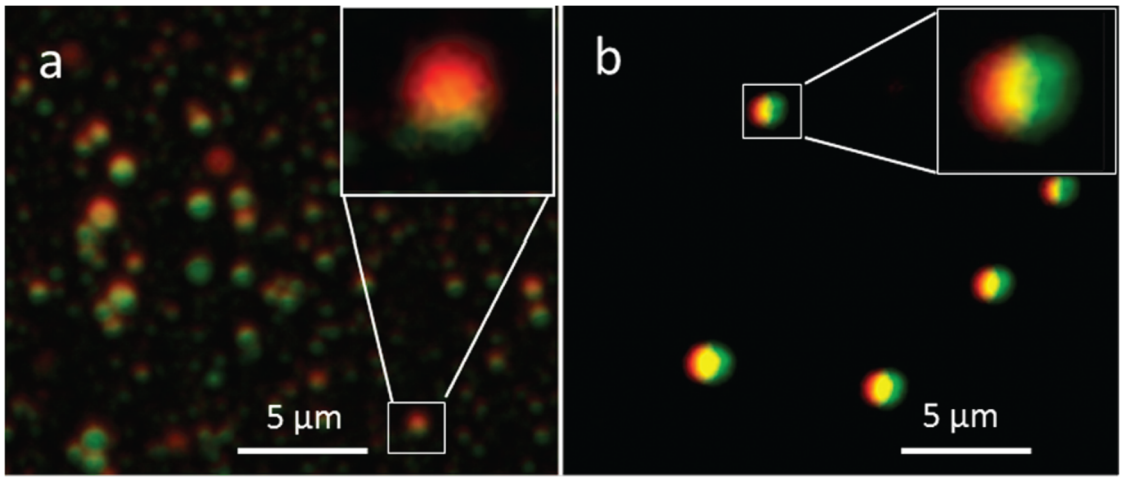

Figure 3.25: Microscope images from Xie et al. of polymeric Janus nanoparticles with differing regions of Nile Red and RH-6g dyes. Reprinted with permission from Xie et al., Copyright 2012 American Chemical Society.

To examine the self-assembling properties of SA+RHOB-Si-PEG+FITC nanoparticles, hydrophobic glass slides were prepared via the method described in section 3.2.6. Glass microscope slides were coated with octadecatrimethoxysilane to produce a hydrophobic surface of 18-carbon chain molecules. It was hypothesized that exposing stearylamine coated or partially stearylamine coated nanoparticles to this surface would cause hydrophobic compounds to align and form an ordered nanoparticle assembly. This concept is shown graphically in Figure 3.26.

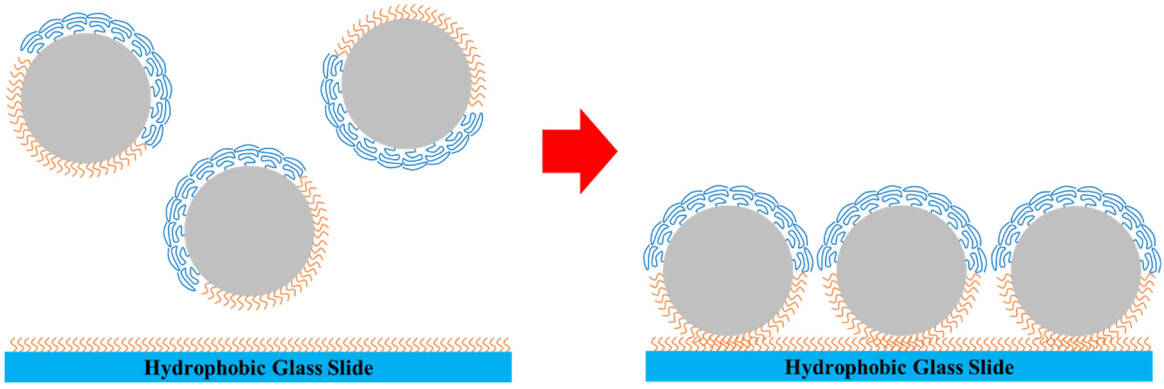

Figure 3.26: Illustration of amphiphilic Janus nanoparticles interacting with a hydrophobic glass slide. The hydrophobic region of the nanoparticle aligns with the hydrophobic surface and creates an ordered layer of nanoparticles.

SA+RHOB-Si-PEG+FITC nanoparticles in chloroform were placed on hydrophobic slides; once the solvent evaporated, cover slips were mounted, and slides were examined using a fluorescent optical microscope. Images were taken in duplicates; one set focused the image with the GFP filter engaged and the duplicate set focused with the RFP filter engaged. Specifically, for GFP focused images, focus on the nanoparticles was established with the GFP filter engaged. The GFP filtered image was taken, then the filter was switched to the RFP to take the second image without changing the focus. Resulting images are shown in Figure 3.27:

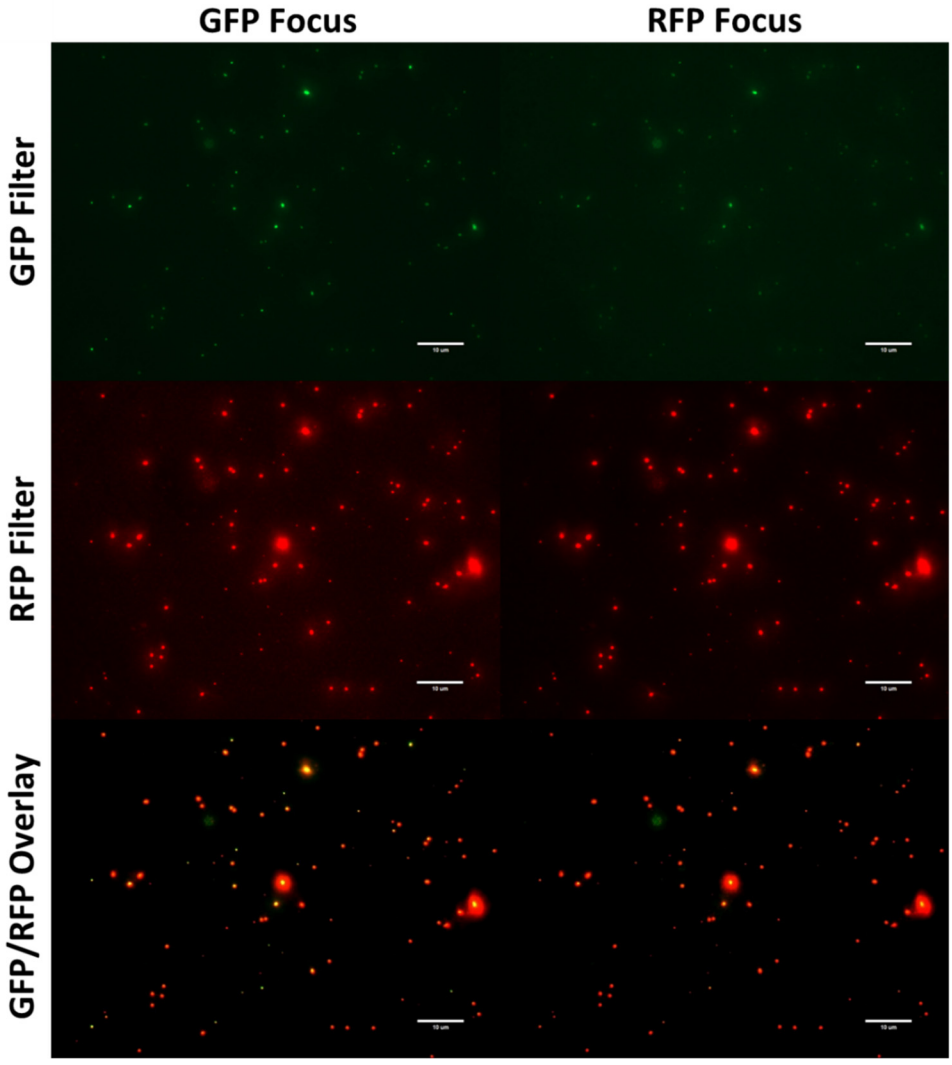

Figure 3.27: Optical microscope images of SA+RHOB-Si-PEG+FITC nanoparticles using a GFP filter (top row), RFP filter (middle row), and a GFP/RFP overlay (bottom row). Left column; focus point for all images was determined with the GFP filter engaged. Right column; focus point for all images was determined with the RFP filter engaged.

Overlain images in Figure 3.27 appeared similar to the images of SA+FITC+RHOB-Si-PEG+FITC+RHOB nanoparticles shown in Figure 3.23. Nanoparticles were visible when using both GFP or RFP filters, and a portion of nanoparticles in the overlain images exhibit yellow cores surrounded by red. After further examination, it was determined that the GFP focused overlain image contained more yellow core nanoparticles than the RFP focused overlay. Zoomed in sections of both overlain images are shown in Figure 3.28 to highlight this difference:

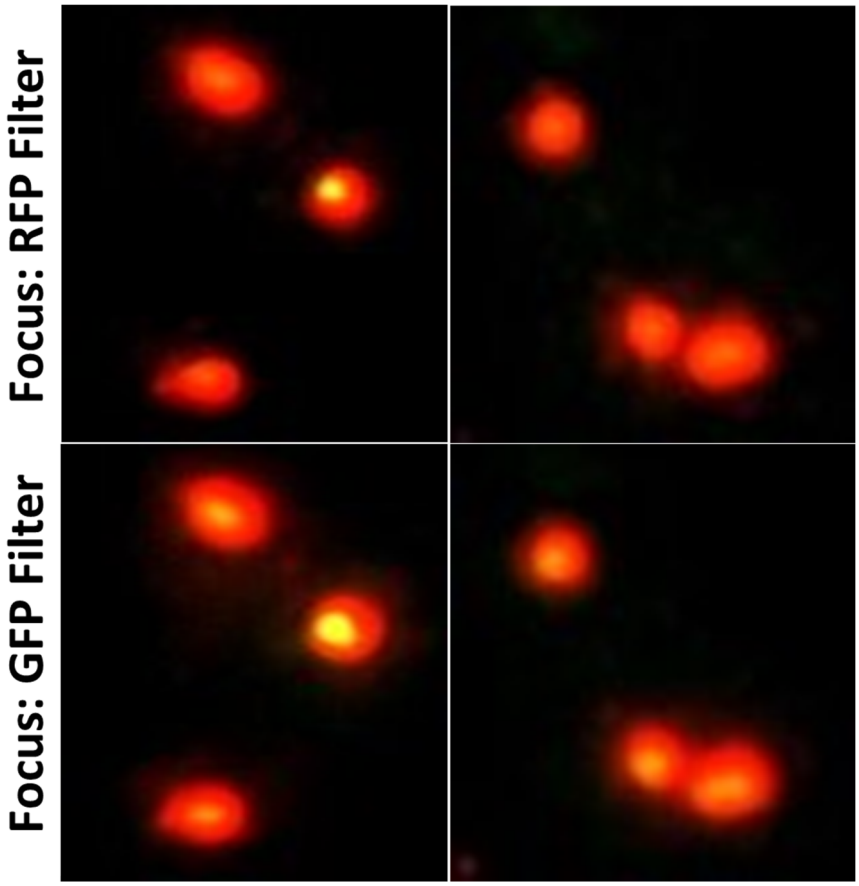

Figure 3.28: Zoomed in images of nanoparticles from overlain images in Figure 3.27

Due to the color difference seen in Figure 3.28, the distance between the GFP and RFP focal points on a single nanoparticle was measured based on the distance between the microscope slide and the optical lens. The process was repeated for multiple nanoparticles to determine and average distance between GFP and RFP focal points. The slide was then inverted on the microscope and the same

measurements were conducted. For comparison, this experiment was conducted a second time using a new hydrophobic slide with SA+FITC+RHOB-Si-PEG+FITC+RHOB nanoparticles, operating under the assumption that a configuration with dyes randomly distributed on the nanoparticle surface would have a smaller or negligible GFP/RFP focal point differential. Results from these experiments are shown in Figure 3.29:

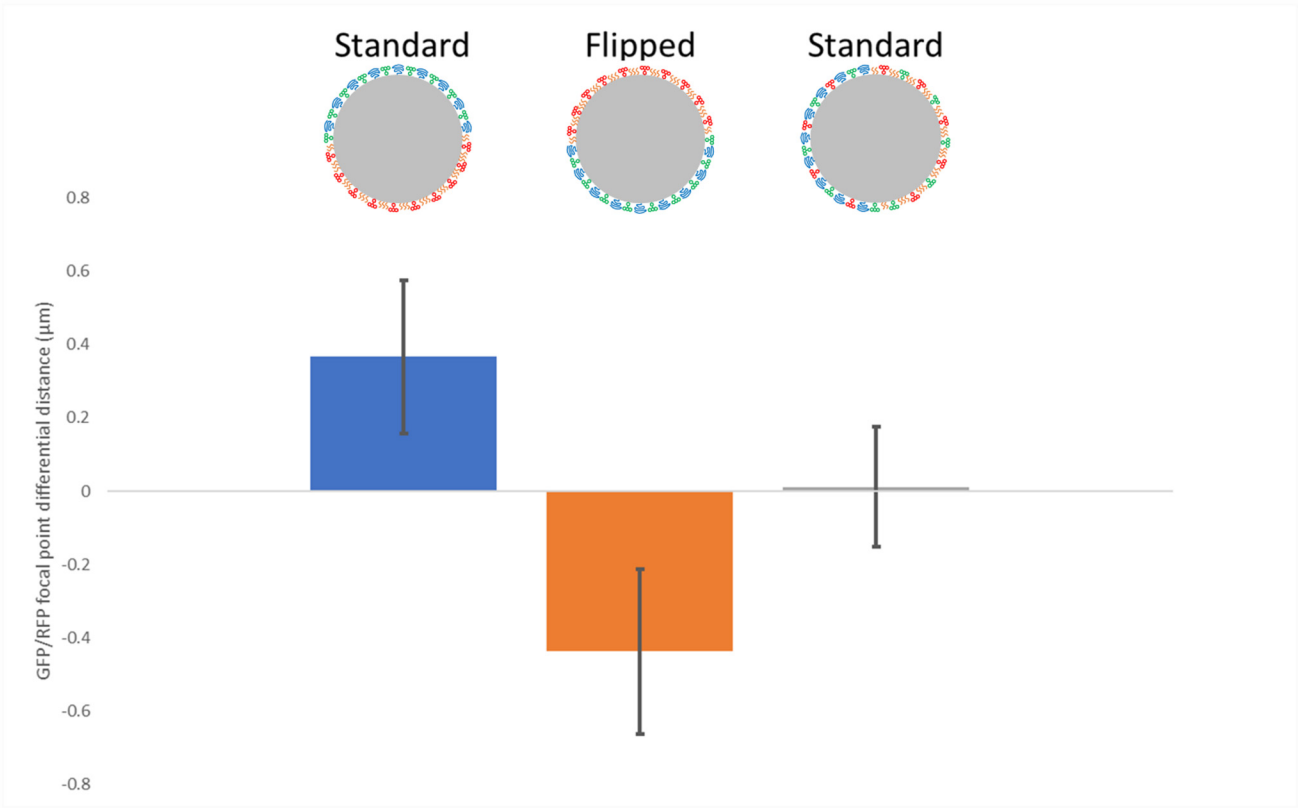

Figure 3.29: Bar graph showing the average distance between GFP and RFP filter focal points for nanoparticles on hydrophobic slides. SA+RHOB-Si-PEG+FITC nanoparticles on a slide set on the microscope in the standard position (cover slip down) is shown in blue. SA+RHOB-Si-PEG+FITC nanoparticles on a slide set on the scope in the inverted position (cover slip up) is shown in orange. SA+FITC+RHOB-Si-PEG+FITC+RHOB nanoparticles on a slide set on the microscope in the standard position (cover slip down) is shown in gray.

Measuring the distance between GFP and RFP focal points for SA+RHOB-Si-PEG+FITC nanoparticles yielded an average distance of 366+/-209 nm for the standard orientation and 438+/-224 nm for the inverted orientation. Negative distances were reported for the inverted orientation

since GFP focal points were determined first in all trials. These distances were reasonable considering the 300 nm diameter of the silica nanoparticles used to create the SA+RHOB-Si-PEG+FITC and SA+FITC+RHOB-Si-PEG+FITC+RHOB configurations. The GFP and RFP focal points for SA+FITC+RHOB-Si-PEG+FITC+RHOB nanoparticles were almost identical (12+/-163 nm). Individual nanoparticle focal point differential distances for SA+FITC+RHOB-Si-PEG+FITC+RHOB nanoparticles were both negative and positive (all starting from the GFP focal point distance). These results reconfirmed the random assortment of dye on the surface of SA+FITC+RHOB-Si-PEG+FITC+RHOB nanoparticles and the regionally specific areas of dye on SA +RHOB-Si-PEG+FITC nanoparticles.

3.4: Summary

Multiple nanoparticle configurations were examined using TEM, dark field microscopy, and optical microscopy on unfunctionalized and functionalized glass slides. TEM images showed nanoparticle configurations with iron oxide nanoparticles selectively modified to one region of silica nanoparticles (OLE-Si-CAION+PEG); these results were similar to images of Janus nanoparticles reported by Perro et. al. Dark field microscopy was used to examine nanoparticles FITC coated regions (OLE-Si-FITC) and optical fluorescent microscopy was used to examine nanoparticles with FITC and RHOB dyes on opposing surface regions (SA+RHOB-Si-PEG+FITC). Xie et. al achieved similar results when imaging dual dyed Janus nanoparticles with multiple fluorescent filters. From the data provided in Chapter 2 and the microscope images presented in this chapter, successful synthesis of two-sided Janus nanoparticles from the packed column method was confirmed. 9 different Janus nanoparticle configurations have been produced, confirming the versatility of the packed column method. Finally, by use of nanoparticle masking, all nanoparticle configurations have a controlled size range. Having addressed two of the challenges mentioned in Chapter 1, Chapter 4 investigates an application for Janus nanoparticles and the initial steps to scale up the packed column method.

Chapter 4: JNP Applications and Scalability for the Packed Column Method

4.1: Introduction to Emulsions and Two-part Polyurethane Foams

4.1.1: Introduction to Emulsions

Emulsions are defined as dispersed systems consisting of two immiscible fluids and are utilized in multiple industries, including agrochemical, pharmaceutical, and cosmetics.[114,115] Most emulsions also contain a surfactant molecule to increase emulsion stability.[116] Historically, emulsions have been categorized into two groups: macroemulsions, which are thermodynamically unstable (though in some cases kinetically stable)[117], with droplet sizes greater than 100 nm, and microemulsions, which are thermodynamically stable with droplet sizes less than 100 nm.[118] The research presented in this chapter focuses on macroemulsions.

Research into particle-stabilized emulsions (Pickering Emulsions) began in 1903.[119,120] Solid particles assemble at the oil-water interface; this phenomenon stabilizes emulsion microdroplets and reduces the rate of emulsion deformation.[121] Success with both amphiphilic surfactant molecules and solid particles on emulsion stability led to investigation into the use of amphiphilic nanomaterials. Researchers determined that amphiphilic particles improved emulsion stability when compared to isotropic-particle stabilized emulsions.[122] Amphiphilic nanoparticles including JNPs have also been investigated as emulsion stabilizers with favorable results.[33,34] Research has also been conducted into control of droplet size and droplet size distribution for Pickering emulsions by modifying the oil/water ratio or using different nanoparticle stabilizers.[123,124]

Based on this data, it was proposed that amphiphilic nanoparticles could produce smaller microdroplets in hexane-water emulsions with smaller size distributions than emulsions prepared without nanoparticles and/or emulsions prepared with isotropic nanoparticles. To test this hypothesis, nanoparticle stabilized emulsions where prepared using hexane and water; stability of

these emulsions was examined to verify that JNPs produced using the packed column method had similar effects on emulsions when compared to JNPs from published literature. Microdroplet size and size distribution was examined in emulsions prepared with isotropic and amphiphilic anisotropic nanoparticles using optical microscopy.

4.1.2: Thermodynamics of Emulsion Formation and Deformation

Stability of an emulsion can be predicted by calculating the free energy change during emulsion formation (ΔG_{EM}):

$$\Delta G_{Em} = \Delta G_I - T\Delta S_{Config} \quad (6)$$

where ΔG_I is the interfacial free energy and $T\Delta S_{Config}$ is the configuration entropy term.[125] ΔG_I is equal to the interfacial tension between liquids (γ_{ab}) multiplied by the area increase between both liquids (ΔA).

$$\Delta G_I = \gamma_{ab}\Delta A \quad (7)$$

For macroemulsions, $\gamma_{ab}\Delta A >> T\Delta S_{Config}$; this means ΔG_{EM} is positive and the formation of the emulsion is nonspontaneous.[125,126] Addition of nanoparticles will improve emulsion stability by adsorption to the liquid-liquid interface, thus reducing the interfacial area A.[125] Free energy change for formation of a Pickering emulsion (ΔG_{Pic}) is shown in equation 8; free energy of adsorption (ΔG_{ads}) of nanoparticles to the liquid-liquid interface is shown in equations 9 and 10:

$$\Delta G_{Pic} = n_d\{A_{drop}\gamma_{ab} + n_p(\Delta G_{ads} - T\Delta S_{ads})\} \quad (8)$$

$$\Delta G_{ads} = -\Delta G_{des} = -\pi r^2\gamma_{ab}(1 - cos\theta)^2 \quad \text{if } \Theta < 90° \quad (9)$$

$$\Delta G_{ads} = -\Delta G_{des} = -\pi r^2\gamma_{ab}(1 + cos\theta)^2 \quad \text{if } \Theta > 90° \quad (10)$$

where n_d is the number of microdroplets in the emulsion, A_{drop} is the surface area of microdroplet with no adsorbed nanoparticles, n_p is the number on nanoparticles adsorbed to one microdroplet, ΔG_{ads} is the free energy of adsorption of nanoparticles to the interface, ΔG_{des} is the free energy of

desorption of nanoparticles from the interface, ΔS_{ads} is the entropy change during adsorption of nanoparticles to microdroplets, T is the temperature, r is the radius of the nanoparticles, and Θ is the contact angle between the nanoparticle surface and the liquid-liquid interface measured through the aqueous phase.[125,127] ΔG_{ads} and $-\Delta G_{des}$ in equation 9 refer to the energy required for a nanoparticle to adsorb to the liquid-liquid interface from the surrounding solvent and desorb from the interface into the surrounding solvent, respectively.[127] ΔG_{ads} and $-\Delta G_{des}$ in equation 10 refer to nanoparticle adsorption and desorption between the interface and the microdroplet solvent.[127] At $\Theta = 90°$, nanoparticles are equally wetted by each liquid phase; ΔG_{des} is at its maximum value and therein provides the most stable emulsion.[125]

4.1.3: Chemistry and Applications of Two-part Polyurethane Foams

Polyurethane is a polymer composed of diol and diisocyanate molecules.[128,129] An exothermic reaction between hydroxyl groups on diol molecules and isocyanate groups on diisocyanate molecules forms long chain polymers.[130] The composition of both molecules can vary greatly since the formation of polyurethane chains is only dependent on the presence of hydroxyl and isocyanate groups. This allows for numerous polyurethane variants with vastly different physical properties.[129] Two-part polyurethane foams are created from mixing binary liquids, one containing diols and the other diisocyanates.[131,132] This research utilized Fibre Glast 2 lb. Polyurethane Mix and Pour Foam for all experiments; this two-component foam utilizes a proprietary diol molecule (undisclosed) and methylene diphenyl diisocyanate.[131] A graphical representation of this reaction in shown in Figure 4.1:

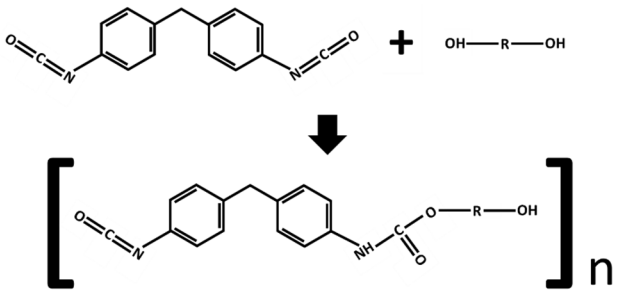

Figure 4.1: Reaction of methylene diphenyl diisocyanate with a diol molecule; the hydroxyl nucleophile bonds to the carbon electrophile in the isocyanate group.

Polyurethane is utilized in multiple industries, including construction, automotive, furniture, and packaging.[133] Production of polyurethanes produces $28.6 billion in revenue worldwide.[134] This project focuses on two-part polyurethane foams which are utilized in the construction industry as sealants and insulation material.[133] Two-part polyurethane foams are graded based on the density of the final foam; high density foams are commonly used as sealants while low density foams are utilized in construction of boats and surfboards.[135,136]

4.2: Emulsions

4.2.1: Materials/Equipment

300 nm Silica nanoparticles were obtained from NanoComposix. Hexane (C_6H_{14}) was obtained from BDH. Ultrapure water was obtained using an ELGA PURELAB Flex water purification system. Sonication is done with a QSonica tip sonicator. An EVOS AMG Optical Fluorescent Microscope was used for microdroplet imaging. Materials for JNPs utilized in these experiments can be found in Chapter 2 and Chapter 3.

4.2.2: Preparing Emulsions with Nanoparticles

2.0 mg of nanoparticles in liquid were added to a 4.0 mL glass vial. The liquid was allowed to evaporate, then 1.0 mL of ultrapure water and 1.0 mL of hexane were added to the vial. The mixture was sonicated for 1 minute at amplitude 10. After sonication, the sample was capped and sealed with parafilm the prevent solvent evaporation.

4.3: Two-part Polyurethane Foams

4.3.1: Materials/Equipment

Fibre Glast 2 lb. Polyurethane Mix and Pour Foam (components 24 and 25) were obtained from Fibre Glast. Chloroform ($CHCl_3$) was obtained from BDH. An EVOS AMG Optical Fluorescent Microscope was utilized for pore imaging. A TA RSA3 Dynamic Mechanical

Analyzer was used for compression experiments. Materials for JNPs utilized in these experiments can be found in Chapter 2 and Chapter 3.

4.3.2: Preparing Foams with Nanoparticles

1.0 mL of component 24 was added to a Styrofoam mold. Nanoparticles were added to the vial in 10 µL of chloroform; the mixture was stirred for 15 seconds with a disposable micro-spatula. 1.0 mL of component 25 was added to the mold and the mixture was stirred for 20 seconds. Foam samples were allowed to form/harden for 4 hours. The Styrofoam molds were removed using razor blades and the foams were cut into four 11x11x7mm rectangular prisms.

4.4: Investigating Scalability of the Packed Column Method

4.4.1: Materials/Equipment

A 100 mL glass chromatography column was obtained from VWR. 300 nm silica nanoparticles were obtained from NanoComposix. mPEG-NHS (MW 5000 and 20,000) were obtained from NANOCS. Glutaraldehyde ($CH_2(CH_2CHO_2)_2$) was obtained Amresco. HEPES ($C_8H_{18}N_2O_4S$) was obtained from Alfa Aesar. Additional materials are noted in Chapter 2 and Chapter 3.

4.4.2: Preparing Scaled-up JNP Syntheses:

The glass chromatography column was attached to a ring stand with the top left open. The bottom outlet tube was attached to a 3-way valve; the second valve position was left open to add materials to the column and the third valve position was attached to tubing that ran to a peristaltic pump. The column was loaded with 50 grams of C_{18} beads (10x increase to syntheses in Chapter 3). Production of JNPs in this column followed the steps for SA-Si-PEG production given in Chapter 3, section 3.2.4. Stearylamine addition was added through the top of column. All fluids removed from the column were pumped out into waste containers from the third 3-way valve position. All washing solvents were added through the top of the column and pumped out in the

same fashion. Glutaraldehyde, nanoparticles, and PEG solutions were added through the second valve position via syringe. A picture of the column used for these experiments is given in Figure 4.2:

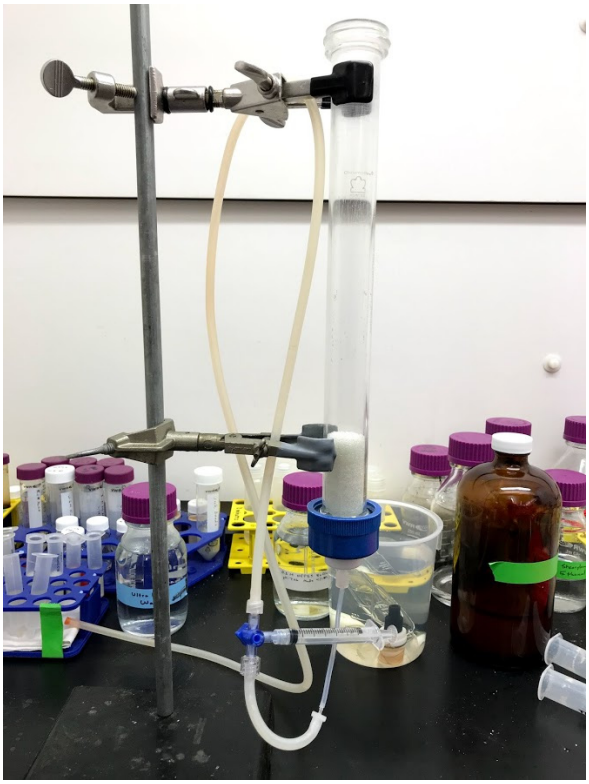

Figure 4.2: Column set up used for scaled up JNP syntheses

4.5: Results and Discussion

4.5.1: Emulsions

Stability of nanoparticles emulsions was determined by comparing the emulsified volume to the total volume for each sample (referred to as the Emulsion Ratio) in hexane/water emulsions. Two versions of SA-SI-PEG nanoparticles were used in this study: one was synthesized with a 5000 Dalton PEG compound (SA-SI-PEG5K) and one with a 20,000 Dalton PEG compound (SA-SI-PEG20K). For comparisons, two versions of PEGylated CPs were prepared using the same materials (PEGSiCPs 5K and PEGSiCPs 20K). Additional comparison samples included an emulsion with no nanoparticles (Blank), one with unreacted aminated silica nanoparticles

(Aminated), and one with stearylamine coated CPs (SASiCPs). Stability was examined over 7 days; the results of this study are shown in Figure 4.3:

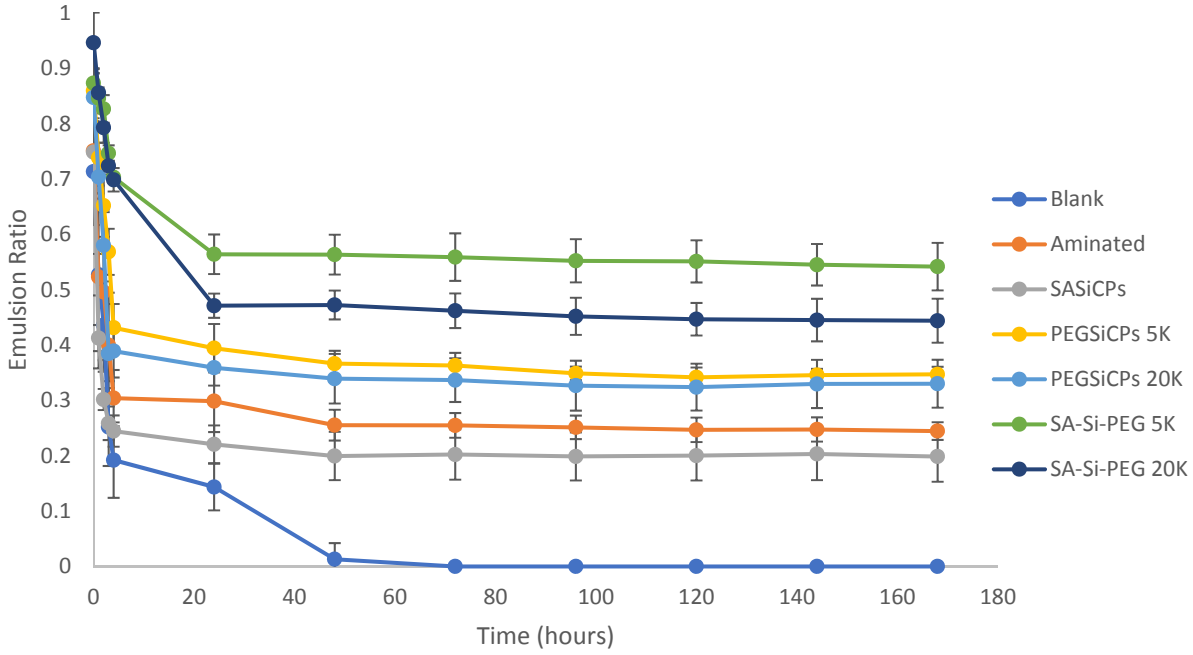

Figure 4.3: Chart showing emulsion ratio over time for nanoparticle stabilized emulsions

From Figure 4.3, SA-Si-PEG nanoparticle stabilized emulsions maintained a larger emulsified volume than all other samples over 7 days. Blank, Aminated, and SASiCPs samples all showed emulsions ratios under 0.3 after 7 days; PEGSiCPs 5K and PEGSiCPs 20K were closer to SA-SI-PEG results with ratios of 0.34 and 0.33, respectively, after 7 days. SA-SI-PEG5K and SA-SI-PEG20K samples showed emulsion ratios of 0.54 and 0.44, respectively. P values from t-tests between PEGylated and SA-Si-PEG stabilized emulsions taken at 7 days indicated significant differences between all samples (SA-Si-PEG 5K vs PEGSiCPs 5K p-value: 0.012, SA-Si-PEG 20K vs PEGSiCPs 20K p-value: 0.044). These findings were comparable to JNP stabilized emulsion studies found in literature; Jiang et al. and Tu also determined that JNPs maintain longer stable emulsions when compared to emulsions without nanoparticles or with isotropic nanoparticles.[122,125]

From Figure 4.3, it was determined that all emulsions prepared without nanoparticles or with isotropic nanoparticles deformed at a faster rate than emulsions prepared with SA-Si-PEG nanoparticles over the first 24 hours. To examine this behavior, the data from Figure 4.3 was normalized; the emulsion ratio at 0 hour indicated the maximum emulsion ratio for a specific sample; the emulsion ratio at 7 days indicated the maximum stable emulsion ratio for that sample. The emulsified volume lost between 0 hour and 7 days was referred to as the unstable emulsion volume. Results shown in Figure 4.4 indicate the percentage of unstable emulsified volume lost between sonication (hour: 0) and stability (hour: 168) at 4 hours and 24 hours:

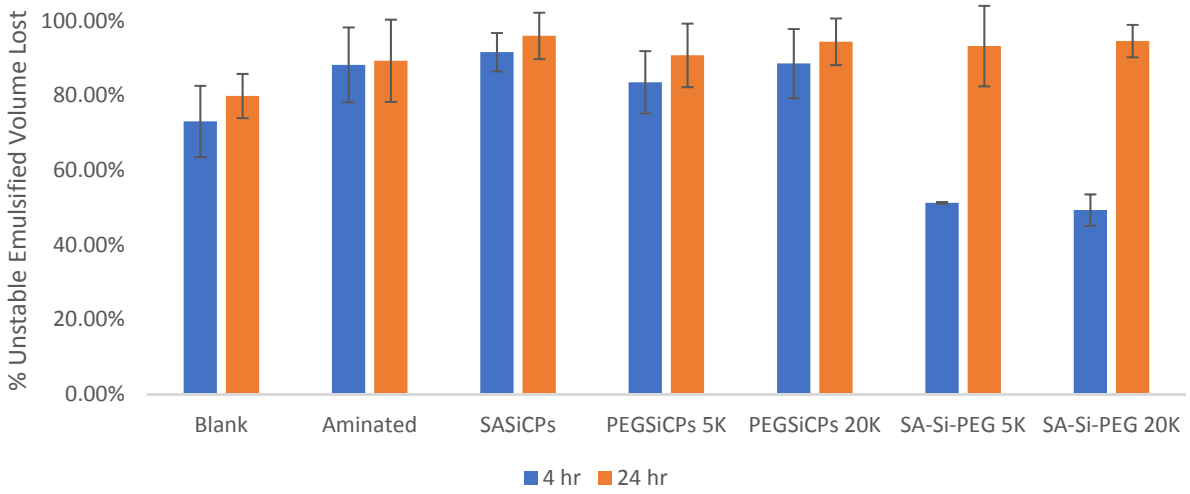

Figure 4.4: Graph showing percent of emulsified area lost as emulsions approach stability for 4 hours (blue) and 24 hours (orange)

From Figure 4.4, emulsions without nanoparticles or containing isotropic nanoparticles lose at least 73% of their unstable emulsified volume in the first 4 hours. Emulsions stabilized with SA-Si-PEG 5K and SA-Si-PEG 20K nanoparticles only lose 51% and 49% of their unstable emulsion volume, respectively, after 4 hours. T-test analysis showed a significant difference between % loss in SA-Si-PEG 5K and SA-Si-PEG 20K nanoparticle stabilized emulsions after 4 hours when compared to emulsions stabilized with isotropic nanoparticles. For emulsified reactions (eg. polymerization reactions) with reaction times less than 24 hours (production of PVC is an example[137]), JNPs like SA-Si-PEG nanoparticles could improve emulsion stability and

concurrently product output per batch. Per these results shown in Figures 4.3 and 4.4, claims made in Jiang et. al. and Tu's work can be confirmed; JNPs can provide superior emulsion stability when compared to isotropic nanoparticles.

The emulsified volume of each sample was examined using an optical microscope to determine the average microdroplet size and size distribution. Microdroplet size was quantified using MATLAB, which detected microdroplets and determined the average microdroplet diameter. Figure 4.5 shows an example of one of these optical microscope images, and Figure 4.6 shows the average microdroplet diameter and standard deviation for each emulsified sample. Due to poor emulsion formation when stabilized with aminated silica nanoparticles, optical microscope measurements could not be done on the "Aminated" sample; this sample is not included in Figure 4.6.

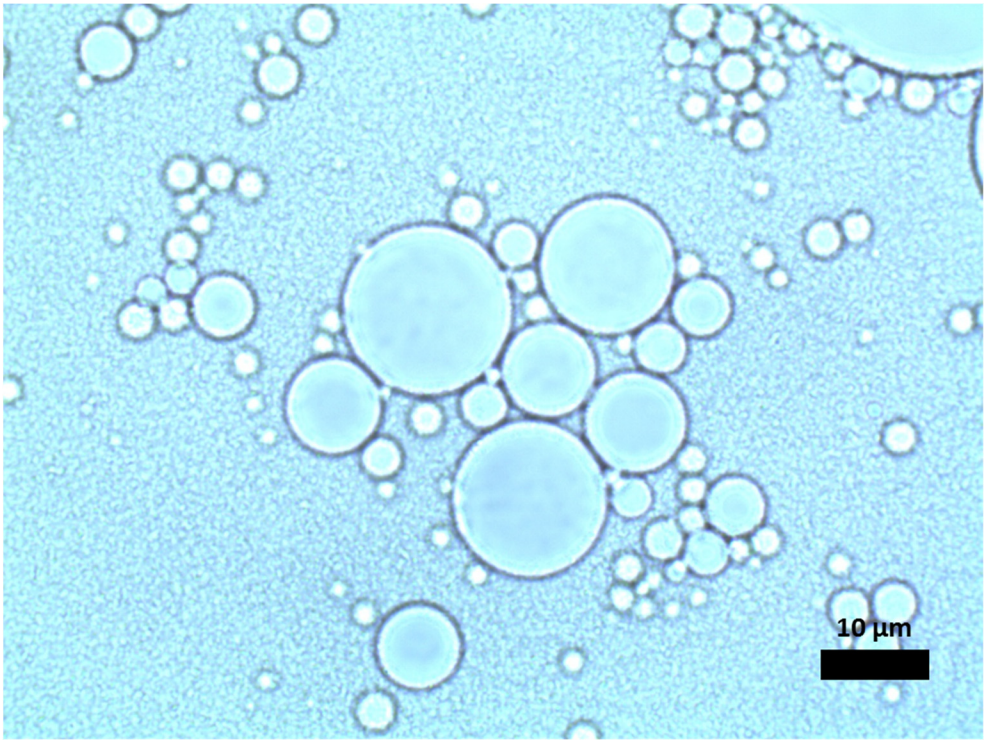

Figure 4.5: Optical microscope images of emulsified area from emulsion stabilized with PEGSiCPs

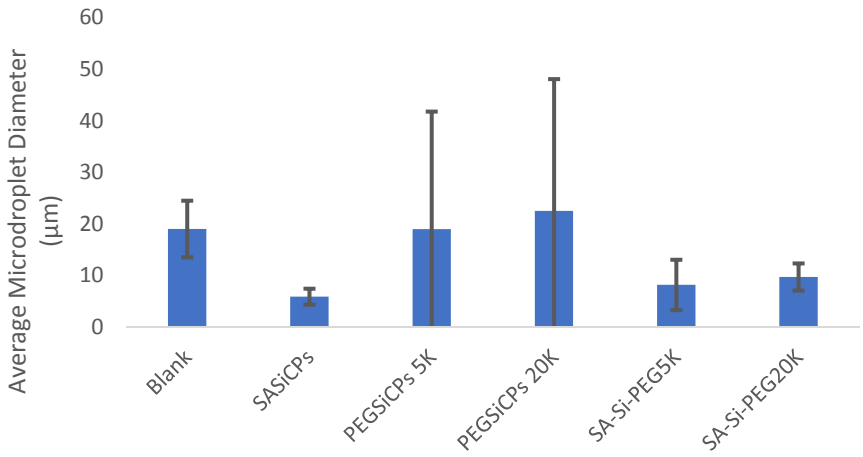

Figure 4.6: Average microdroplet diameter from emulsions stabilized with different nanoparticles

From Figure 4.6, SA-Si-PEG5K and SA-Si-PEG20K nanoparticles produced smaller, more monodispersed microdroplets when compared to PEGylated samples and the blank sample. Significant differences between average microdroplet diameters were confirmed by the t-test (all p-values were less than 0.05). Anova tests can give inaccurate p-values when comparing sample sets of different size[138]; data set sizes were not equivalent in this experiment, so no Anova tests were conducted. SASiCPs stabilized emulsions showed smaller droplet size and size deviation than SA-Si-PEG5K and SA-Si-PEG20K nanoparticles; however, the stability study shown in Figure 4.4 and 4.5 indicated that SASiCPs had the second worst long-term stability (>24 hours) and the worst short-term stability (<24 hours), respectively. The ability to produce monodispersed microdroplets is not useful if nanoparticles cannot maintain a stable emulsified volume. Excluding data on SASiCPs based on poor performance in the stability study, SA-SI-PEG 5K and SA-SI-PEG 20K nanoparticles produced larger stable emulsified volumes with smaller and more monodispersed microdroplets when compared to samples without nanoparticles or isotropic nanoparticles.

4.5.2: Two-part Polyurethane Foams

Results in section 4.5.1 determined that JNPs could successfully reduce the average microdroplet size and microdroplet size distribution in hexane-water emulsions. Success in a

liquid-liquid system led to investigation of JNPs for size control in a liquid-gas system. Based on results from the emulsions studies, it was proposed that amphiphilic nanoparticles could reduce the pore size in two-part polyurethane foams and reduce the pore size deviations. To test this hypothesis, foams were prepared with equal concentrations of either isotropic of anisotropic nanoparticles and examined using the optical microscope.

Polyurethane foams were prepared using 0.5 mg of the following nanoparticle configurations: no nanoparticles (Blank), SASiCPs, PEGSiCPs 5K, PEGSiCPs 20K, SA-Si-PEG5k, and SA-Si-PEG20K. Images of nanoparticles foams were taken using an optical microscope. From these images, average pore size was determined in each foam sample using ImageJ software. Microscope images were converted to an 8-bit grey scale image; the threshold was adjusted to create white pore boundaries on a black background. With the threshold set, ImageJ then created a second image displaying numbered structures and their respective areas measured in pixels^2. Each structure was compared to the original microscope image to determine which structures represented closed pores. Finally, diameters of closed pores were added to a database for averaging. To calculated closed pore diameter, pores were assumed to have a spherical structure. To the authors knowledge, there was not a better method for calculating average pore size for amorphous closed pores without doing individual pore measurements. An example of these images is shown in Figure 4.7, and a bar graph showing the average pore diameter for all foams is shown in Figure 4.8:

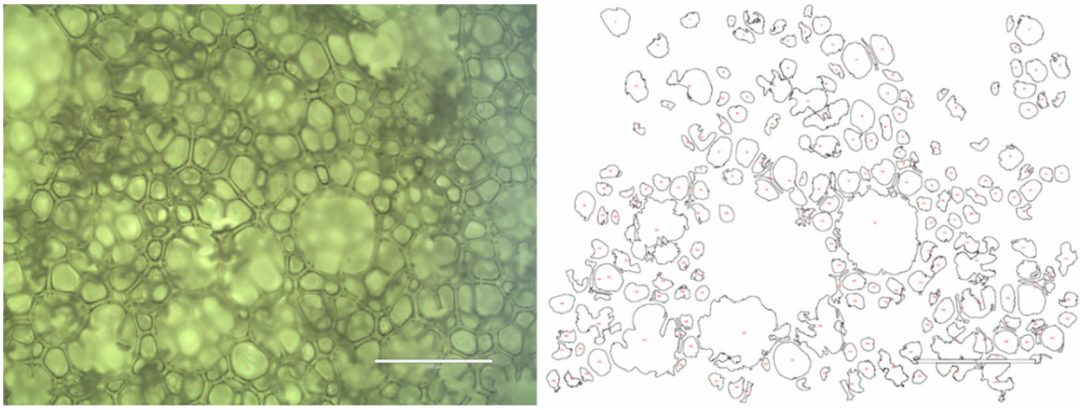

Figure 4.7: (left) Optical microscope image taken of foam sample developed with SA-Si-PEG5K nanoparticles; (right) image of structures developed by ImageJ software from the adjacent microscope image

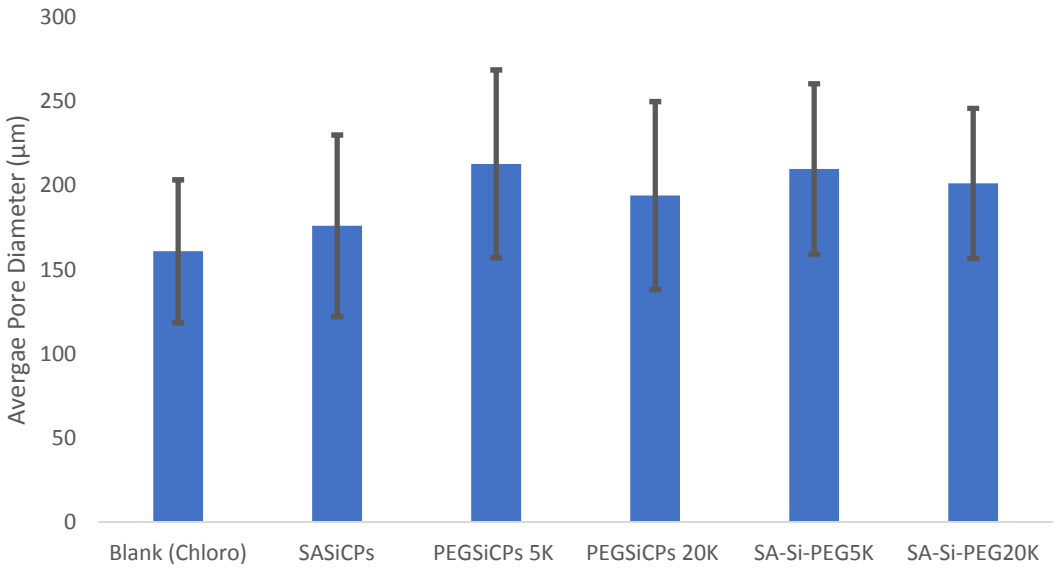

Figure 4.8: Average pore diameter of foams produced with different nanoparticle configurations as determined by ImageJ software

The data in Figure 4.8 showed no significant difference between the average pore sizes or pore size distributions in any of the foams. There are multiple factors that could explain these results, most likely an inadequate number of nanoparticles in the foams to effect average pore structure. It is also possible that this experiment requires more data points to determine statistically significant differences between foam samples. The process of developing this data had a large human component since every image produced by ImageJ must be examined, and as such the number of total data points for each foam sample is limited.

A second attempt to determine pore size distribution was done using compression testing. 11x11x7mm foam samples were compressed using a dynamic mechanical analyzer. During compression, a stress vs strain curve was developed (an example is shown in Figure 4.9); the Young's modulus, or elastic modulus, can be determined by identifying the slope of the linear region of this curve.[139] The relationship between the Young's modulus and porosity of a material was determined by Nielsen:[140]

$$E = E^s \left[\frac{1-p}{1+\frac{p}{\rho}}\right] \quad (11)$$

Where E is the Young's modulus, E^s is the Young's modulus of a non-porous sample of the same material, p is the volume concentration of pores relative to the total volumes of solids and pores (porosity), and ρ is the shape factor for the geometry of the pores.[140] Equation 11 verifies a proportionality between the Young's modulus and porosity; for identical materials, as porosity increases, Young's modulus will decrease. Results from compression testing are shown in Figure 4.10.

Two assumptions were made to compare foam porosity to pore size distribution. The first assumption, as made previously, was that pores have spherical coordinates. The second assumption stated that foams of equal volume had the same number of total pores. In reality, different foam samples likely have various amounts of pores in amorphous shapes. If these assumptions are made, and the average pore size between foams of equal volume is the same, pore size deviation is directly proportional to porosity. These two assumptions generalize the structural properties of these foams; results from this analysis can only give an estimate of pore size distribution. This method was chosen due to a lack of available methods for measuring pore size and pore size distribution in closed pore foams. There is little published literature on investigation of pore size and pore size distribution in closed pore materials; methods are normally limited to microscope imaging and predicative models.[141,142] Results from compression testing are shown in Figure 4.10:

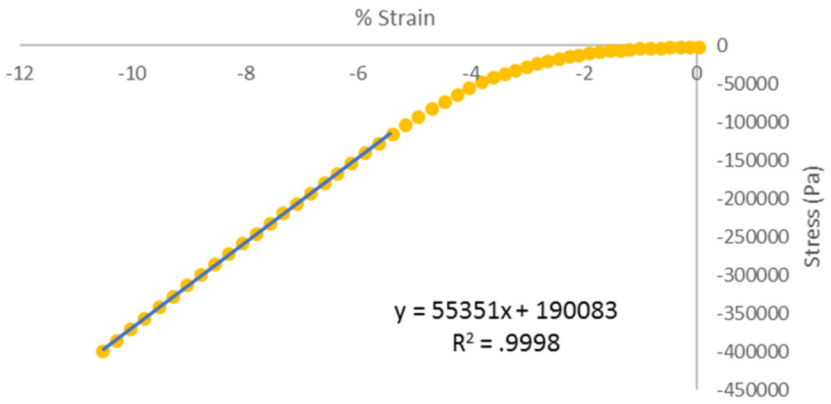

Figure 4.9: Stress vs. strain curve developed from compressing foam samples produced with SA-Si-PEG5K nanoparticles. The slope of the linear region of the stress vs. strain curve is the Young's Modulus

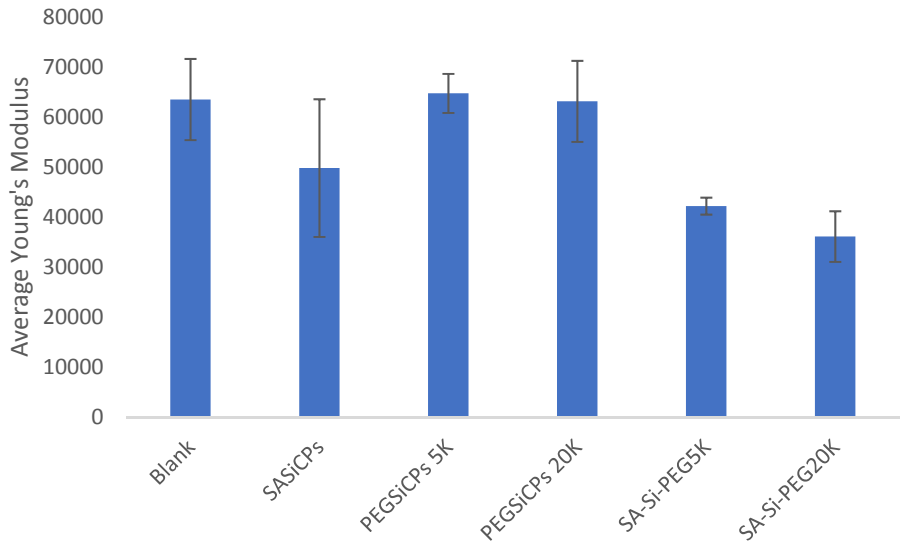

Figure 4.10: Average Young's Modulus for foam samples

From Figure 4.10, no statistical significance was determined when comparing the average Young's Modulus in different foam samples. T-tests were done between each foam sample; all p-values were greater than 0.05. Anova tests were not performed due to differences in data set size. These results indicated no significant difference in pore size distribution between foam samples, similar to the results found from optical microscope analysis (Figure 4.8). As stated previously, it is possible that larger concentrations on nanoparticles in foams could produce significant differences in pore size and pore size distribution. However, based on the results in Figure 4.8 and Figure 4.10, it is possible that 2-part polyurethane foams are not a good model system to test JNP interfacial assembly. The only method for measuring pore size for these foams was optical microscopy; without additional methods, microscope results cannot be verified. Microscopy and compression testing were used to measure pore size distribution, but compression testing can only give a crude estimate of the pore size distribution due to the assumptions required to relate the Young's Modulus to pore size distribution. Unless additional methods for measuring pore size and pore size distribution in closed-cell foams are identified, effects of nanoparticles on the formation of pores cannot be quantified.

4.5.3: Scaling of Synthesis Method

SA-Si-PEG nanoparticles were produced using the method described in 4.4.2. This synthesis utilized 10 times more C_{18} beads, and thusly had 10 times more surface area for nanoparticle masking. It was predicted that this synthesis would yield 10 times more JNPs than the syntheses run in Chapter 3. For comparison, SA-Si-PEG nanoparticles were also prepared using the quantities described in Chapter 3, 3.2.4. The final mass of JNPs from the scaled-up synthesis and the average masses of all SA-Si-PEG syntheses are shown in Table 4.1. FTIR analysis was done on 10x and 1x samples for comparison. Nanoparticles from the 10x sample were also added to a 50/50 hexane water emulsion (concentration of nanoparticles in emulsion was the same as experiments from 4.5.1) to examine emulsion stability. FTIR results are shown in Figure 4.11 and emulsion stability results are shown in Figure 4.12:

Table 4.1: Mass of Nanoparticles from 1x and 10x SA-Si-PEG5K Syntheses

Nanoparticle Config.	Synthesis Scale	Mass (mg)	Standard Deviation
SA-Si-PEG5K	1x	0.47	+/- 0.06
SA-Si-PEG5K	10x	4.8	---------

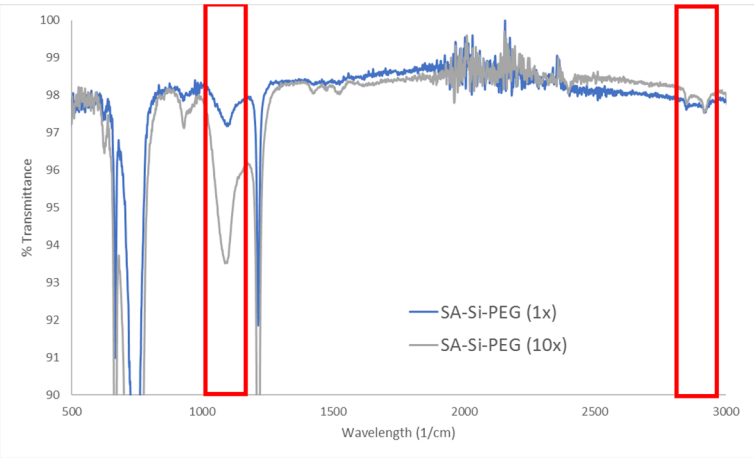

Figure 4.11: FTIR analysis of SA-Si-PEG5K nanoparticles from 1x and 10x syntheses. The left red box indicates peaks in both spectrums at 2900-3000 cm^{-1}; the right red box indicates peaks in both spectrums at 1000-1200 cm^{-1}

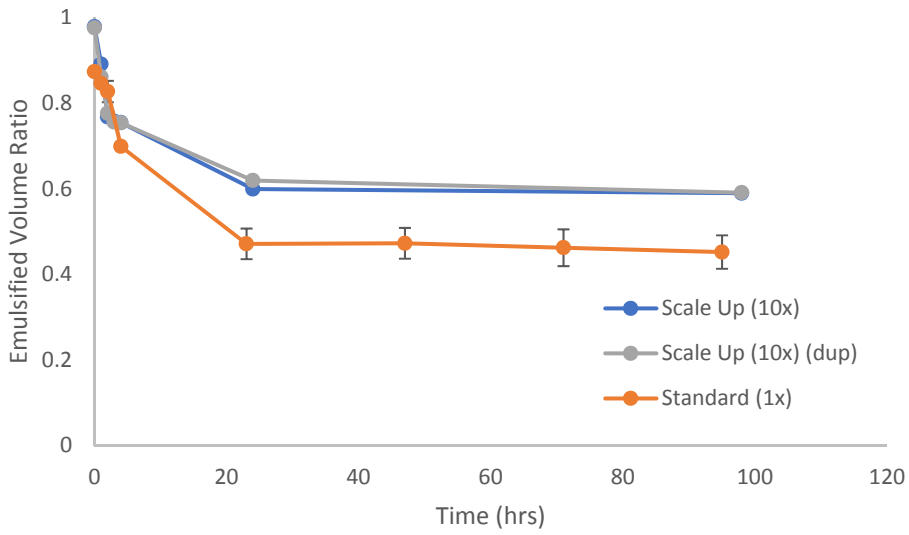

Figure 4.12: Emulsions Stability Curves for SA-Si-PEG5K nanoparticles from 1x (orange) and 10x (blue and gray) syntheses.

From Table 4.1, the scaled-up synthesis produced roughly 10x more nanoparticles (10.2x) than the 1x synthesis. In Figure 4.9, peaks were seen at 1000-1200 cm^{-1} (carbon-oxygen bond stretching and silica-oxygen bond stretching) and 2900-3000 cm^{-1} (methyl and methylene bond stretching) similar to peaks seen for OLE-SI-PEG nanoparticles in Figure 3.13. Higher nanoparticle concentrations from the 10x synthesis led to the more intense FTIR peaks. When emulsified in the presence of hexane and water, SA-Si-PEG5K nanoparticles from the 10x synthesis perform similarly to SA-Si-PEG5K from the 1x synthesis (SA-Si-PEG5K from 10x stabilize at emulsion ratio 0.589 and 5.90, SA-Si-PEG5K from 1x stabilize at emulsion ratio 0.452). The most likely cause for the discrepancy between 1x and 10x emulsion ratios is a difference in nanoparticle concentration. Long evaporation times were allowed and multiple weight measurements were conducted to determine accurate dry weights for JNPs synthesized at 1x scale, but it is possible that these measurements were skewed due measuring small masses of nanoparticles and the limitations of the weighing equipment. While the results for the 10x sample from the emulsion study were advantageous from an application standpoint, more syntheses need to be run at this scale to identify the reason for the increased long-term emulsion stability.

4.6 Summary

In this section, an application for JNPs produced using the packed column method has been investigated; initial investigation into the scalability of the packed column method was also done. Stability studies showed that our JNP emulsions out perform all other emulsions (with and without nanoparticles) for long and short-term stability. Microdroplets with small deviations in diameter were produced in the emulsions that utilized JNPs, further indicating the advantage of JNPs over isotropic nanoparticles for improved emulsion stability. The conclusions presented in this dissertation agree with other published studies utilizing JNPs as emulsion stabilizers.[33,34,125,143] Experiments using 2-part polyurethane foams did not yield significant results with regards to any effect of JNPs on final pore distribution. These results were likely due to an insufficient number of nanoparticles added to the foam components, a lack of sufficient data points to develop statistically significant results, and inaccuracy in the methods for measuring pore size and pore size distribution in closed cell foams.

Finally, JNPs of SA-Si-PEG configurations were prepared in a column with 10x the standard amount of stationary phase material. This synthesis produced 10.2x more nanoparticles than our standard syntheses; FTIR analysis indicated that the surface modifications to these nanoparticles were similar to modifications produced in Chapter 3. Hexane-water emulsions showed increased emulsion stability with nanoparticles produced at 10x scale. Additional 10x syntheses need to be conducted to determine if this characteristic is consistent between reactions. Despite the discrepancy between emulsion stability for 1x and 10x JNPs, overall results indicate that the packed column method could be scaled-up to produce larger quantities of nanoparticles. The next step for scalability investigation is to increase the column capacity to pilot plant scale; JNPs produced in these larger quantities will need to be compared to JNPs from lab scale syntheses to confirm similar structure and performance. The transition point between lab scale and pilot scale differs depending on the industry and product; this concept will be discussed further in Chapter 5.

Chapter 5: Overall Conclusions and Future Work for the Janus Project

5.1: Conclusions

In this work, a method for synthesizing JNPs that addresses all three major challenges has been developed. Controlled size ranges of JNPs can be produced via a masking method using monodispersed isotropic nanoparticles. Masking nanoparticles onto spherical surfaces in a packed column increases final JNP yield without large increases in reactor volume. Finally, using hydrophobic stationary phase material as the masking surface, different JNP configurations can be produced without making changes to the synthesis method or equipment.

Multiple characterization techniques were employed to examine JNPs and confirm the development of different surface regions. Using optical and electron microscopy, differences on the nanoparticle surfaces could be identified based on roughness (OLE-Si-CAION+PEG) or fluorescence (SA+RHOB-Si-PEG+FITC). Examining JNP behavior at the liquid-liquid interface of immiscible solvents and the solid-gas interface on hydrophobic microscope slides allowed for the study of JNP self-assembly, and further confirmed the presence of different regions on JNP surfaces. Once proper JNP structure was confirmed, JNPs were utilized in hexane-water emulsions and 2-part polyurethane foams to improve stability and control pore size, respectively. Results confirmed that JNPs maintained a larger emulsified volume over time in hexane/water emulsions when compared to emulsions stabilized by isotropic nanoparticles.

Results from experiments with a liquid-gas environment (2-part polyurethane foams) were inconclusive, likely due to either an inadequate number of nanoparticles in foam samples, insufficient data points in data analysis, or a lack of accurate methods for measuring pore size. Referring to the images in Figure 4.7, using ImageJ software to identify pore areas requires user verification to remove non-pore structures. It is possible that more data points could be determined by automating the ImageJ process described previously, which could lead to smaller pore size deviations. Regarding the concentrations of nanoparticles in foam samples, based on the average

foam pore sizes reported in Figure 4.8, over 100 mgs of nanoparticles per foam sample would be required to totally coat the liquid-gas interface in each foam sample. With the standard JNP synthesis outlined in Chapter 3 producing 0.5 mgs of nanoparticles, the expense of preparing foams with even a 10% coating (both JNP and control particles) was outside the scope of this project. Finally, methods used to measure pore size and pore size distribution required assumptions that greatly generalized the structure of the foam. More accurate measurement methods that do not require such broad assumptions need to be determined before investigation of JNPs on foam pore structure can continue.

Finally, initial investigation into scalability was done by increasing the size of the stationary phase by 10x (from 5 grams to 50 grams of C_{18} beads). Results showed that 10.2x more JNPs were produced in the scaled-up column. Surface compounds on JNPs produced from the 10x reaction were examined using FTIR, and JNP behavior in hexane/water emulsions was also investigated. Results from these experiments showed that JNPs produced in 10x reaction were similar to JNPs prepared in 1x reaction. The only difference between these two JNP samples was the long-term emulsion ratio, where JNPs from a 10x reaction outperformed JNPs from the 1x reaction. Long-term emulsion ratios for JNP produced at this scale need to be confirmed through running additional scale-up syntheses. Despite the difference in long term emulsion ratio, overall results indicate that the packed column method can produce larger quantities of nanoparticles by increasing the amount of stationary phase material, and as such is potentially scalable. The next step for scaling this process involves the production and analysis of JNPs on larger pilot plant-scale columns. Scalability will be addressed in more detail later in the chapter.

5.2: Future Work

5.2.1: Improvements/Possible Changes to the Packed Column Method

JNP yield from the packed column method could be increased by improving the hydrophobic coating on C_{18} beads. Based on the diameters for C_{18} beads and silica nanoparticles used in Chapter 3 and Chapter 4, our standard column for JNP synthesis (5 grams of C_{18} beads) could produce 6.5 mgs of JNPs if nanoparticle coverage of the stationary phase is maximized. It is likely that quantities of JNP less than 6.5 mgs reported in Chapter 4 were due to incomplete

coatings of octadecatrimethoxysilane on the C_{18} bead surface. To improve these coatings, octadecatrimethoxysilane coated glass slides could be prepared with varied reaction times and octadecatrimethoxysilane concentrations. Water contact angle measurements could be done on each slide to determine the reaction conditions for an optimal hydrophobic coating.[144] These reaction conditions could then be applied to glass beads. If JNP yields are still significantly lower than the theoretical maximum, other methods such as chemical vapor deposition could be attempted to improve coatings on hydrophobic beads.[145]

Versatility of JNP configurations produced via the packed column method could be improved by utilizing different stationary phase materials. The work presented in this document discusses columns that use hydrophobic materials normally utilized in reversed-phase chromatography; materials from ion-exchange chromatography could be used in a similar manner. Ion-exchange chromatography utilizes either a cation (negatively charged) or anion (positively charged) exchange stationary phase to separate charged molecules.[146] For the production of JNPs, positively charged nanoparticles (like the 300 nm aminated silica used in Chapters 3 and 4) could be adsorbed onto a cation exchange column. Nanoparticles would be partially masked by the stationary phase, allowing a regionally specific reaction of an M2 compound to the nanoparticles. Finally, the JNPs are eluted from the column by passing a high ionic strength buffer through the column.[147] Different JNP configurations could be developed by changing the nanoparticles or M2 compounds. The process of producing JNPs on an ion exchange column is depicted in Figure 5.1:

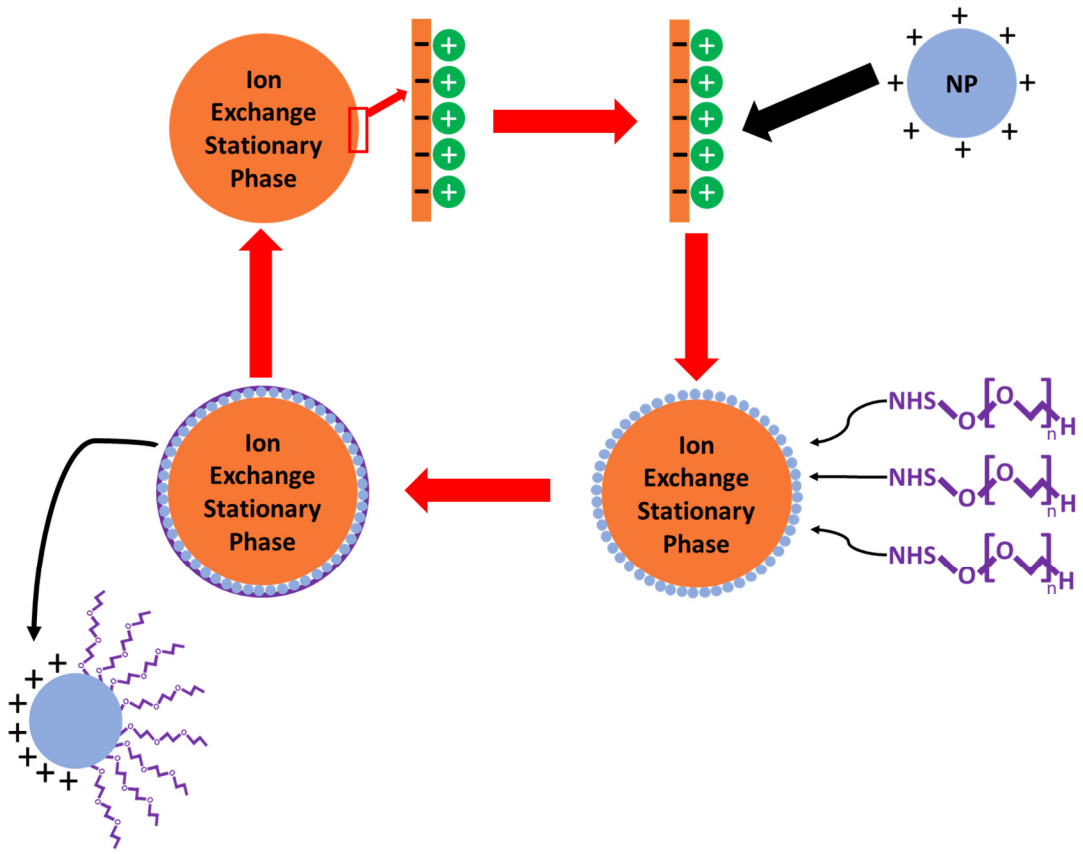

Figure 5.1: Illustration of JNP synthesis strategy using a cation exchange stationary phase. The negatively charged stationary phased is equilibrated with buffer solution (ex. sodium phosphate)[148]; sodium ions from the buffer equilibrate the negatively charged stationary phase surface. Addition of positively charged nanoparticles will displace the sodium ions and adsorb to the stationary phase. The unmasked region of the nanoparticles can be reacted with an M2 compound (ex. mPEG-NHS shown in purple). Nanoparticles are eluted from the column by passing a buffer with high ionic strength through the stationary phase[148]

5.2.2: Applications for JNPs from the Packed Column Method

The versatility of the packed column method leads to production of numerous JNP configurations for various applications. Emulsion stability and pore size control were examined in Chapter 4; theoretical applications for JNPs including drug delivery vehicles and hydrophobic coatings were discussed briefly in Chapter 1. Development of an antimicrobial JNP has been

discussed since preliminary investigations into this project; continued investigation of the packed column method will likely involve synthesis of an antimicrobial JNP. Initial studies will involve one of two JNP configurations: a silica nanoparticle with regions of stearylamine and small silver nanoparticles (similar to the OLE-Si-CAION+PEG configuration) or silver nanoparticles with a region of oleylamine and an unreacted region. Hydrophobic surfaces (similar to the hydrophobic microscope slides in Chapter 3) would be produced to form self-assembled nanoparticle layers. Nanoparticles layers will be coated with solutions of bacteria cells to test their antimicrobial ability. A graphic of the interaction between a bacteria cell and a JNP surface is shown in Figure 5.2. LIVE/DEAD assays would be used to determine the effect of the nanoparticles on the cells. If the e. coli cells are chosen for this experiment, the LIVE/DED assay will use SYTO 9 and propidium iodide fluorescent dyes to differentiate between living and dead cells. SYTO 9 will affect all cells (alive or dead) and causes the cells to fluoresce green when examined with an optical microscope with the appropriate fluorescent filter. Propidium iodide will affect cells with damaged cell membranes (dead cells) and fluoresce red (propidium iodide fluorescence will overpower any remaining SYTO 9 fluorescence in dead cells).[149,150] An image of dyed cells from this assay is shown in Figure 5.3. Optical fluorescent microscopy and flow cytometry would be used to quantify living vs dead cells. Additional studies would include the use of non-antimicrobial JNPs in place of antimicrobial JNPs to confirm that JNPs are the cause of cellular death. Surfaces prepared with antimicrobial JNPs would also be exposed to foreign compounds (dirt, dust, etc.) before exposure to cells to determine if antimicrobial activity is effective for unclean surfaces.

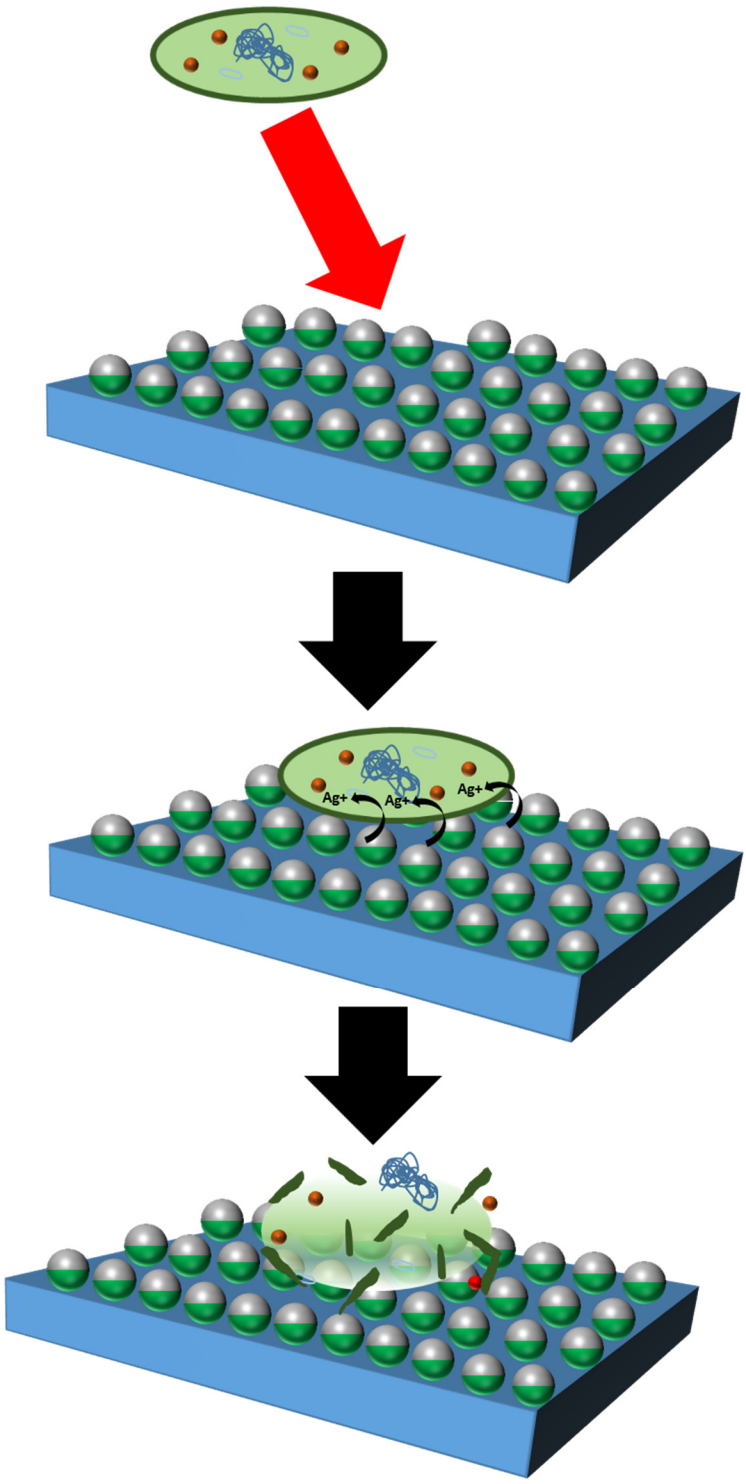

Figure 5.2: Interaction of a bacteria cell with an antimicrobial JNP surface. In this illustration, the green region of the JNPs aligns with the blue surface. A silver region is assembled upward and interacts with the cell. Transfer of silver ions causes the cell membrane to rupture and eventually causes cell death.[151–154]

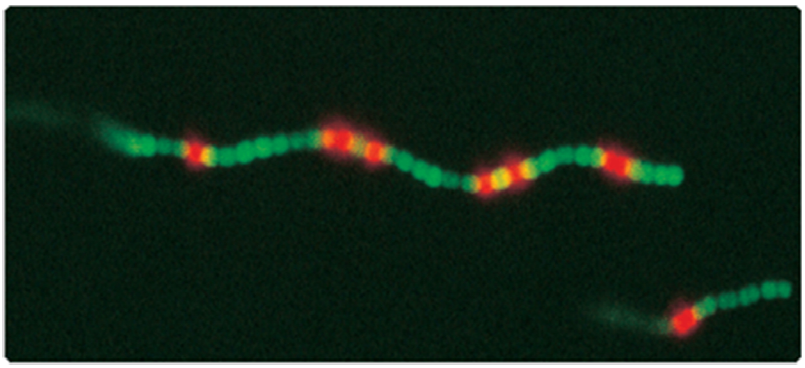

Figure 5.3: Living (green) and dead (red) e. coli cells dyed with SYTO 9 or propidium iodide from the LIVE/DEAD Assay[149]

5.2.3: Scale-up for Packed Column Method

To confirm scalability of the packed column method, JNP production will need to be increased from lab scale (bench scale) to pilot scale.[155] Differences between bench and pilot scale can be measured in mass/volume of product yielded or reactor volume; the ratios vary depending on the type of process (batch or continuous) and the industry.[155] For batch processes in the pharmaceutical industry, bench scale reactions yield between 1-20 kg of product; pilot scale reactions yield between 20-100 kg.[156] Based on this ratio, JNPs/batch would need to increase 5-20x to reach pilot scale. In commercial nanoparticle synthesis, NanoComposix produces batches of silica nanoparticles from 10-150 grams/batch.[157,158] Assuming the improvements discussed in section 5.2.1 can maximize nanoparticle coverage of stationary phase material, Table 5.1 shows the scale increase required and the resulting JNP yield (in grams) to meet pilot scale/match commercial processes:

Table 5.1: Mass of JNPs Produced based on Scale-Up of the Column

Scale Up	none	5x	20x	154x	2308x
JNP Yield (grams)	0.065	0.325	1.3	10	150

Base on Table 5.1, a 2308x larger column would be required (compared to the lab scale columns discussed in Chapter 3) to match NanoComposix silica production. The FDA's Scale-UP and Post-Approval Changes (SUPAC) guidelines for scale-up of pharmaceutical processes stipulates that a process must be validated every time it is scaled-up by a factor of 10.[159] To match NanoComposix's yield, structure of JNPs from the packed column method would need to be re-evaluated 3 times (10x, 100x, and 1000x) using the methods from section 4.5.3 to confirm scalability.

JNP yield increases can be achieved by using larger columns and/or running multiple parallel columns. 150 grams of JNPs could be synthesized in a packed column with a bed height of 138 cm and a 30 cm diameter. A flow diagram for a large scale packed column is shown in Figure 5.4:

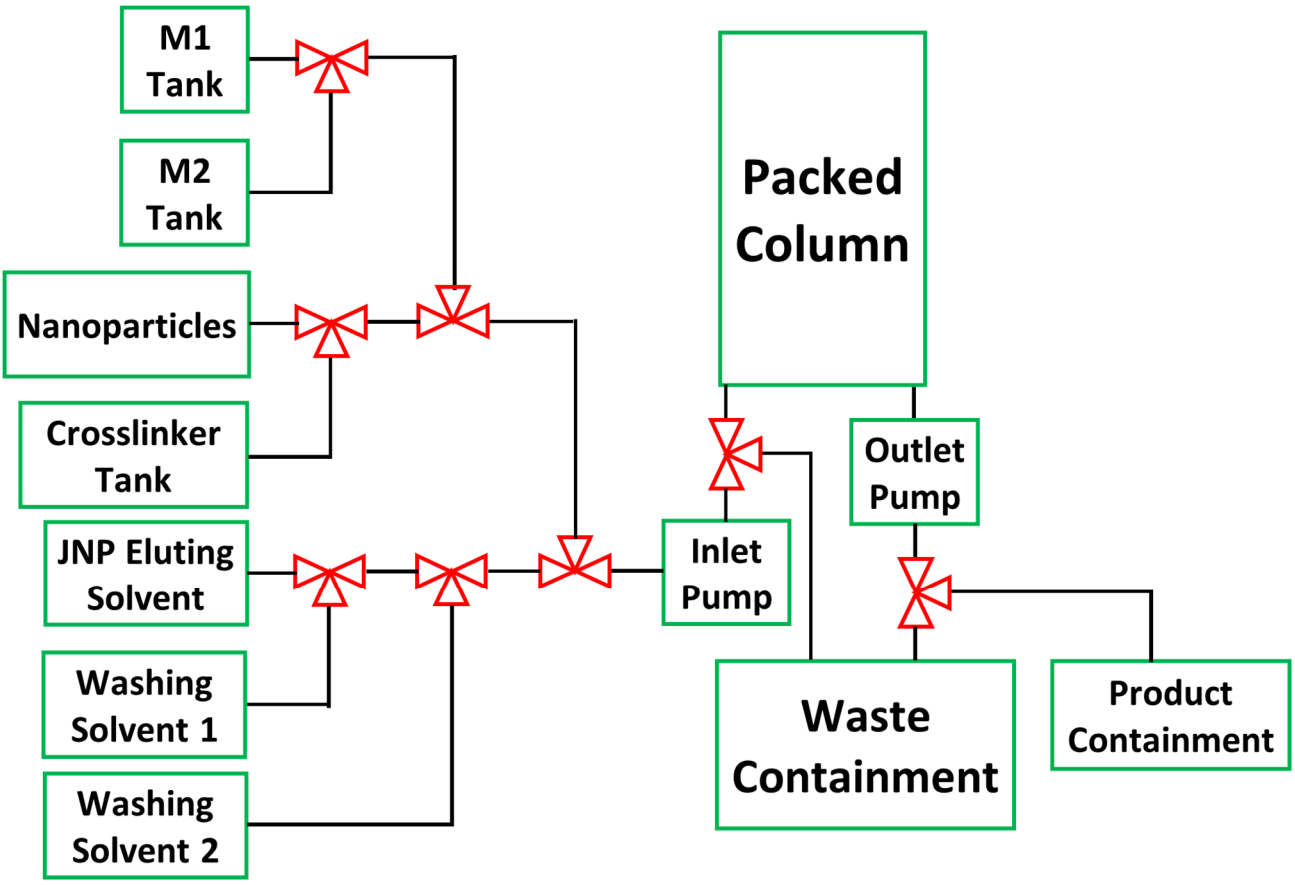

Figure 5.4: Flow diagram for producing JNPs using the packed column method

Figure 5.4 shows a packed column with an inlet and outlet pumps. Inlet pumps load nanoparticles, M1 and M2 compounds, crosslinking molecules, and solvents into the column; an additional valve is placed between the inlet pump and the column for cleaning the pump between steps. The outlet pump can either pump to waste containment or to product containment for finished JNPs. This setup will change depending on JNP configuration.

References

1. Granqvist CG, Buhrman RA, Wyns J, Sievers AJ. Far-infrared absorption in ultrafine Al Particles. *Phys Rev Lett*. 1976;37(10):625-629. doi:10.1103/PhysRevLett.37.625.

2. Drexler EK. *Engines of Creation: The Coming Era of Nanotechnology*. Garden City, NY: Anchor Press/Doubleday; 1986.

3. Drexler EK. *Nanosystems: Molecular Machinery, Manufactoring, and Computation*. New York: John WIley & Sons, Inc.; 1992.

4. Strambeanu N, Demetrovici L, Dragos D, Lungu M. *Nanoparticles: Definition, Classification and General Physical Properties*. Springer; 2015.

5. Buzea C, Pacheco II, Robbie K. Nanomaterials and nanoparticles: Sources and toxicity. *Biointerphases*. 2007;2(4):MR17-MR71. doi:10.1116/1.2815690.

6. Science: The importance of nanotechnology. *BBC*. 2014. http://www.bbc.co.uk/schools/gcsebitesize/science/21c/materials_choices/nanotechnologyrev1.shtml. Accessed January 5, 2018.

7. Henglein A. Small-Particle Research: Physicochemical Properties of Extremely Small Colloidal Metal and Semiconductor Particles. *Chem Rev*. 1989;89(8):1861-1873. doi:10.1021/cr00098a010.

8. Alivisatos AP. Perspectives on the physical chemistry of semiconductor nanocrystals. *J Phys Chem*. 1996;100(31):13226-13239. doi:10.1021/jp9535506.

9. Burda C, Chen X, Narayanan R, El-Sayed MA. *Chemistry and Properties of Nanocrystals of Different Shapes*.; 2005. doi:10.1021/cr030063a.

10. Requejo-Isidro J, del Coso R, Solis J, Gonzalo J, Afonso CN. Role of surface-to-volume ratio of metal nanoparticles in optical properties of Cu : Al2O3 nanocomposite films. *Appl Phys Lett*. 2005;86(19):193104. doi:10.1063/1.1923198.

11. Rock ME. Nanotehcnology: A Key Trend in the Pharmaceutical and Biotech Industries. *Carolina-South Atl Chapter Newsl*. 2007.

12. Nantional Nanotechnology Initiative: Benefits and Applications. 2018. https://www.nano.gov/you/nanotechnology-benefits.

13. Nanoparticles in Sunscreen. 2018. https://www.ewg.org/sunscreen/report/nanoparticles-in-sunscreen/#.WzOaQlUzrcs.

14. De Volder MFL, Tawfick, Sameh H, Baughman RH, Hart AJ. Carbon Nanotubes: Present and Future Commerical Applications. *Science (80-)*. 2013;339(6119):535-539. doi:10.1126/science.1222453.

15. DeLuca MJ, Felker CJ, Heider D, et al. (12) United States Patent. 2016. doi:10.1145/634067.634234.

16. Pagni J. Armoy aims to become nano-leader. *Eur Plast News*. 2010:1. http://www.plasticsnewseurope.com/headlines2.html/id=1267781513. Accessed January 7, 2018.

17. Bradley P. Everyday Applications of Nanotechnology. 2011. http://ccweek.com/article-2630-everyday-applications-of-nanotechnology.html. Accessed October 4, 2018.

18. Lattuada M, Hatton TA. Synthesis, properties and applications of Janus nanoparticles. *Nano Today*. 2011;6(3):286-308. doi:10.1016/j.nantod.2011.04.008.

19. Walther A, Muller AHE. Janus Particles: Synthesis, Self-Assembly, Physical Properties, and Applications. *Soft Matter*. 2008;4(4):663-668.

20. Xie H, She ZG, Wang S, Sharma G, Smith JW. One-step fabrication of polymeric Janus nanoparticles for drug delivery. *Langmuir*. 2012;28(9):4459-4463. doi:10.1021/la2042185.

21. Dong B, Li B, Li CY. Janus nanoparticle dimers and chains via polymer single crystals. *J Mater Chem*. 2011;21(35):13155-13158. doi:10.1039/c1jm12866c.

22. Cho I, Lee K-W. Morphology of latex particles formed by poly(methyl methacrylate)-seeded emulsion polymerization of styrene. *J Appl Polym Sci*. 1985;30(5):1903-1926.

23. de Gennes Pi-G. Soft Matter (Nobel Lecture). *Angew Chemie Int Ed English*. 1992;31(7):842-845.

24. Zhang JZ, Wang Z, Liu Ju, Chen S, Liu G. *Self-Assembled Nanostructures*. New York: Kluwer Academic/Plenum; 2003.

25. Isaacs L, Chin DN, Bowden N, Xia Y, Whitesides GM. *Supramolecular Materials and Technologies*. (Reinhoudt DN, ed.). New York: Jon Wiley & Sons; 1999.

26. Zhang J, Zhao Y, Han S, Chen C, Xu H. Self-assembly of surfactant-like peptides and their applications. *Sci China Chem*. 2014;57(12):1634-1645. doi:10.1007/s11426-014-5234-4.

27. Diudea M. *Nanostructures: Novel Architecture*. 17th ed. New York: Nova Science; 2005.

28. Kotov N. *Introduction to Nanoscale Science and Technology*. Boca Raton: Dekker/CRC; 2006.

29. Synytska A, Khanum R, Ionov L, Cherif C, Bellmann C. Water-repellent textile via decorating fibers with amphiphilic janus Particles. *ACS Appl Mater Interfaces*. 2011;3(4):1216-1220. doi:10.1021/am200033u.

30. Zhang L, Luo Q, Zhang F, et al. High-performance magnetic antimicrobial Janus nanorods decorated with Ag nanoparticles. *J Mater Chem*. 2012;22(45):23741. doi:10.1039/c2jm35072f.

31. Gao Y, Yu Y. How half-coated janus particles enter cells. *J Am Chem Soc*. 2013;135(51):19091-19094. doi:10.1021/ja410687z.

32. Li X, Zhou L, Wei Y, El-Toni AM, Zhang F, Zhao D. Anisotropic growth-induced synthesis of dual-compartment janus mesoporous silica nanoparticles for bimodal triggered drugs delivery. *J Am Chem Soc*. 2014;136(42):15086-15092. doi:10.1021/ja508733r.

33. Zahn N, Kickelbick G. Synthesis and aggregation behavior of hybrid amphiphilic titania Janus nanoparticles via surface-functionalization in Pickering emulsions. *Colloids Surfaces A Physicochem Eng Asp*. 2014;461(1):142-150.

doi:10.1016/j.colsurfa.2014.07.039.

34. Yi F, Xu F, Gao Y, Li H, Chen D. Macrocellular polymer foams from water in oil high internal phase emulsion stabilized solely by polymer Janus nanoparticles: preparation and their application as support for Pd catalyst. *RSC Adv*. 2015;5(50):40227-40235. doi:10.1039/C5RA01859E.

35. Sánchez A, Díez P, Martínez-Ruíz P, Villalonga R, Pingarrón JM. Janus Au-mesoporous silica nanoparticles as electrochemical biorecognition-signaling system. *Electrochem commun*. 2013;30:51-54. doi:10.1016/j.elecom.2013.02.008.

36. Naoi K, Ohko Y, Tatsuma T. TiO2 Films Loaded with Silver Nanoparticles: Control of Multicolor Photochromic Behavior. *J Am Chem Soc*. 2004;126(11):3664-3668. doi:10.1021/ja039474z.

37. Majetich SA, Sachan M. Magnetostatic interactions in magnetic nanoparticle assemblies: Energy, time and length scales. *J Phys D Appl Phys*. 2006;39(21). doi:10.1088/0022-3727/39/21/R02.

38. Perro A, Reculusa S, Ravaine S, Bourgeat-Lami EB, Duguet E. Design and synthesis of Janus micro- and nanoparticles. *J Mater Chem*. 2005;15(35-36):3745-3760. doi:10.1039/b505099e.

39. Jiang S, Schultz MJ, Chen Q, Moore JS, Granick S. Solvent-free synthesis of janus colloidal particles. *Langmuir*. 2008;24(18):10073-10077. doi:10.1021/la800895g.

40. Pradhan S, Xu LP, Chen S. Janus nanoparticles by interfacial engineering. *Adv Funct Mater*. 2007;17(14):2385-2392. doi:10.1002/adfm.200601034.

41. Sardar R, Heap TB, Shumaker-Parry JS. Versatile solid phase synthesis of gold nanoparticle dimers using an asymmetric functionalization approach. *J Am Chem Soc*. 2007;129(17):5356-5357. doi:10.1021/ja070933w.

42. Li J, Wang L, Benicewicz BC. Synthesis of Janus nanoparticles via a combination of the reversible click reaction and “grafting to” strategies. *Langmuir*. 2013;29(37):11547-11553. doi:10.1021/la401990d.

43. Hein C, Liu X-M, Wang D. Click Chemistry, a Powerful Tool for Pharmaceutical Sciences. *Pharm Res*. 2009;25(10):2216-2230. doi:10.1007/s11095-008-9616-1.Click.

44. Zhang T, Davidson D, Bryant S, Huh C. Nanoparticle-Stabilized Emulsions for Applications in Enhanced Oil Recovery. *Proc SPE Improv Oil Recover Symp*. 2010. doi:10.2118/129885-MS.

45. Perro A, Meunier F, Schmitt V, Ravaine S. Production of large quantities of "Janus" nanoparticles using wax-in-water emulsions. *Colloids Surfaces A Physicochem Eng Asp*. 2009;332(1):57-62. doi:10.1016/j.colsurfa.2008.08.027.

46. Gu H, Yang Z, Gao J, Chang CK, Xu B. Heterodimers of nanoparticles: Formation at a liquid-liquid interface and particle-specific surface modification by functional molecules. *J Am Chem Soc*. 2005;127(1):34-35. doi:10.1021/ja045220h.

47. Glaser N, Adams DJ, Böker A, Krausch G. Janus particles at liquid-liquid interfaces. *Langmuir*. 2006;22(12):5227-5229. doi:10.1021/la060693i.

48. Perry MC. *Langmuir-Blodgett Films*. 1st ed. (Barlow WA, ed.). Cambridge: Cambridge University Press; 1996.

49. Hadjichristidis N, Pispas S, Floudas GA. *Block-Copolymers: Synthetic Strategies, Physical Properties, and Applications*. Hoboken: John Wiley & Sons, Inc.; 2003.

50. Poggi E, Bourgeois J-P, Ernould B, Gohy J-F. Polymeric Janus nanoparticles templated by block copolymer thin films. *RSC Adv*. 2015;5(55):44218-44221. doi:10.1039/C5RA05290D.

51. Deng R, Li H, Zhu J, et al. Janus Nanoparticles of Block Copolymers by Emulsion Solvent Evaporation Induced Assembly. *Macromolecules*. 2016;49(4):1362-1368. doi:10.1021/acs.macromol.5b02507.

52. Erhardt R, Böker A, Zettl H, et al. Janus micelles. *Macromolecules*. 2001;34(4):1069-1075. doi:10.1021/ma000670p.

53. Fu X, Liu J, Yang H, et al. Arrays of Au-TiO2 Janus-like nanoparticles fabricated by block copolymer templates and their photocatalytic activity in the degradation of

methylene blue. *Mater Chem Phys*. 2011;130(1-2):334-339. doi:10.1016/j.matchemphys.2011.06.054.

54. Tian L, Zhang B, Li W, et al. Facile fabrication of Fe3O4@PS/PGMA magnetic Janus particles via organic–inorganic dual phase separation. *RSC Adv*. 2014;4(52):27152. doi:10.1039/c4ra03140g.

55. Saito N, Kagari Y, Okubo M. Effect of colloidal stabilizer on the shape of polystyrene/poly(methyl methacrylate) composite particles prepared in aqueous medium by the solvent evaporation method. *Langmuir*. 2006;22(22):9397-9402. doi:10.1021/la061298v.

56. Roh K, Martin DC, Lahann J. Biphasic Janus particles with nanoscale anisotropy. *Nat Mater*. 2005;4(10):759-763. doi:10.1038/nmat1486.

57. Taylor G. Disintegration of Water Drops in an Electric Field. *Proc R Soc A Math Phys Eng Sci*. 1964;280(1382):383-397. doi:10.1098/rspa.1964.0151.

58. Rahmani S, Ashraf S, Hartmann R, et al. Engineering of nanoparticle size via electrohydrodynamic jetting. *Bioeng Transl Med*. 2016;1(1):82-93. doi:10.1002/btm2.10010.

59. Fessi H, Puisieux F, Devissaguet JP, Ammoury N, Benita S. Nanocapsule formation by interfacial polymer depostion folowwing solvent displacement. *Int J Pharm*. 1989;55(1):R1-R4.

60. Miladi K, Sfar S, Fessi H, Elaissari A. *Polymer Nanoparticles for Nanomedicines*.; 2016. doi:10.1007/978-3-319-41421-8.

61. Zhao N, Gao M. Magnetic janus particles prepared by a flame synthetic approach: Synthesis, characterizations and properties. *Adv Mater*. 2009;21(2):184-187. doi:10.1002/adma.200800570.

62. Gu H, Zheng R, Zhang X, Xu B. Facile One-Pot Synthesis of Bifunctional Heterodimers of Nanoparticles: A Conjugate of Quantum Dot and Magnetic Nanoparticles. *J Am Chem Soc*. 2004;126(18):5664-5665. doi:10.1021/ja0496423.

63. Rosen MJ, Kunjappu JT. *Surfactants and Interfacial Phenomena*. 4th ed. Hoboken: Wiley-Interscience; 2004.

64. Sprung MM. A summary of the reactions of aldehydes with amines. *Chem Rev*. 1940;26(3):297-338. doi:10.1021/cr60085a001.

65. Caravajal GS, Leyden DE, Quinting GR, Maciel GE. Structural Characterization of (3-Aminopropyl)triethoxysilane-Modified Silicas by Silicon-29 and Carbon-13 Nuclear Magnetic Resonance. *Anal Chem*. 1988;60(17):1776-1786. doi:10.1021/ac00168a027.

66. McMurry J. *Orgnaic Chemistry with Biological Applications*. 2nd ed. Belmont: Brooks/Cole; 2011.

67. Harvey D. The Vocabulary of Analytical Chemistry. *Anal Chem 20*. 2009:1-65.

68. HPLC Separation Modes. 2018. http://www.waters.com/waters/en_US/HPLC-Separation-Modes/nav.htm?cid=10049076&locale=en_US. Accessed July 1, 2018.

69. Mehta A. Principle of Reversed-Phase Chromatography HPLC/UPLC (with Animation). 2012. https://pharmaxchange.info/2012/12/principle-of-reversed-phase-chromatography-hplcuplc-with-animation/.

70. Molnar I, Horvath C. Reverse phase chromatography of polar biological substances: separation of catechol compounds by high performance liquid chromatography. *Clin Chem*. 1976;22(9):1497-1502.

71. Editors L. The LCGC Blog: Back to Basics: The ROle of Thermodynamics in Chromatographic Separations. 2013. http://www.chromatographyonline.com/lcgc-blog-back-basics-role-thermodynamics-chromatographic-separations.

72. The LC Handbook: Guide to LC Column and Method Development. 2017. https://www.agilent.com/cs/library/primers/Public/LC-Handbook-Complete-2.pdf.

73. Reversed Phase Chromatography. 1999:1-93. http://www.chromacademy.com/.../Theory_Of_HPLC_Reverse_Phase_Chromatography.pdf. Accessed July 1, 2018.

74. Lodish H, Berk A, Zipursky S. *Molecular Cell Biology*. 4th ed. New York: W.H.

Freeman; 2000.

75. Williams LD. Molecular Interactions. 2017. https://ww2.chemistry.gatech.edu/~lw26/structure/molecular_interactions/mol_int.html.

76. Garrett RH, Grisham CM. *Biochemistry*. 6th ed. Boston: Cengage Learning; 2017.

77. Bird RB, Stewart WE, Lightfoot EN. *Transport Phenomenon*. 2nd ed. New York: John WIley & Sons, Inc.; 2007.

78. Zhang Y, Wang S, Zhou J, et al. Interfacial Activity of Nonamphiphilic Particles in Fluid − Fluid Interfaces. *Langmuir*. 2017;33:4511-4519. doi:10.1021/acs.langmuir.7b00599.

79. McMichael K. Amine Reactions. 2017. http://chemistry2.csudh.edu/rpendarvis/index.html.

80. Sun S, Zeng H, Robinson DB, et al. Monodisperse MFe 2 O 4 (M) Fe , Co , Mn) Nanoparticles. 2004;4(1):126-132.

81. Hatakeyama M, Kishi H, Kita Y, et al. A two-step ligand exchange reaction generates highly water-dispersed magnetic nanoparticles for biomedical applications. *J Mater Chem*. 2011;21(16):5959. doi:10.1039/c0jm04381h.

82. Horiba Scientific - Dynamic Light Scattering. 2016. http://www.horiba.com/scientific/products/particle-characterization/technology/dynamic-light-scattering/. Accessed July 1, 2018.

83. Smith BC. *Infrared Spectral Interpretation: A Systematic Approach*. 1st ed. Boca Raton, Fl: CRC Press; 1998.

84. Nakanishi K. Infrared Absorption Spectroscopy. *J Pharm Sci*. 1963;52(7):716.

85. Cheraghipour E, Javadpour S, Mehdizadeh AR. Citrate capped superparamagnetic iron oxide nanoparticles used for hyperthermia therapy. *J Biomed Sci Eng*. 2012;5(December):715-719. doi:10.4236/jbise.2012.512089.

86. Richardson J. IR Spectroscopy Tutorial: Amines. 2011. https://orgchemboulder.com/Spectroscopy/irtutor/aminesir.shtml. Accessed July 1, 2018.

87. Surbhi S. Difference Between T-test and ANOVA. 2016. https://keydifferences.com/difference-between-t-test-and-anova.html. Accessed July 16, 2018.

88. Lane DM. Online Statistics Education: An Interactive Multimedia Course of Study. http://onlinestatbook.com/2/analysis_of_variance/intro.html. Accessed July 16, 2018.

89. 3.2 - Hypothesis Testing (P-value approach). 2018. https://onlinecourses.science.psu.edu/statprogram/node/138/. Accessed July 1, 2018.

90. Moore JW, Stanitski CL, Jurs PC. *Chemistry: The Molecular Science*. 4th ed. Belmont: Brooks Cole; 2005.

91. Fanchi JR. *Principles of Applied Reservoir Simulation*. 3rd ed. Gulf Professional Publishing; 2005.

92. Du K, Glogowski E, Emrick T, Russell TP, Dinsmore AD. Adsorption Energy of Nano- and Microparticles at Liquid - Liquid Interfaces. *Langmuir*. 2010;26(23):12518-12522. doi:10.1021/la100497h.

93. Bhuiyan MHU, Saidur R, Amalina MA, Mostafizur RM, Islam AKMS. Effect of nanoparticles concentration and their sizes on surface tension of nanofluids. *Procedia Eng*. 2015;105:431-437. doi:10.1016/j.proeng.2015.05.030.

94. Härtel A, Oettel M, Rozas RE, Egelhaaf SU, Horbach J, Löwen H. Tension and stiffness of the hard sphere crystal-fluid interface. *Phys Rev Lett*. 2012;108(22):1-5. doi:10.1103/PhysRevLett.108.226101.

95. Bush JWM. Surface tension module. *URL http//web mit edu/163/www/Lec-notes/ ...*. 2004:1-4. doi:10.13040/IJPSR.0975-8232.7(2).531-42.

96. Chang H-C, Wang L-C. A Simple Proof of Thue's Theorem on Circle Packing. 2010:1-4. https://arxiv.org/abs/1009.4322.

97. Chinnam J, Das DK, Vajjha RS, Satti JR. Measurements of the surface tension of nanofluids and development of a new correlation. *Int J Therm Sci*. 2015;98:68-80. doi:10.1016/j.ijthermalsci.2015.07.008.

98. Ophardt CE. Virtual Cehmbook - Fatty Acids. 2003. http://chemistry.elmhurst.edu/vchembook/551fattyacids.html. Accessed February 5, 2018.

99. Seader JD, Henley EJ. *Seperation Process Principles*. 2nd ed. (Welter J, McFadden P, Kulesa T, eds.). Hoboken: John Wiley & Sons; 2006.

100. Hill S, P FI. Channeling in packed columns. *Chem Eng Sci*. 1952;1(6):247-253. doi:10.1016/0009-2509(52)87017-4.

101. Stichlmair J, Bravo JL, Fair JR. General model for prediction of pressure drop anc capacity of countercurrent gas/liquid packed column. *Gas Sep Purif*. 1989;61(12):19-28. doi:10.1016/0950-4214(89)80016-7.

102. Gao XM, Rhodes J. An essential role for constitutive Schiff base-forming ligands in antigen presentation to murine T cell clones. *J Immunol*. 1990;144(8):2883-2890.

103. Migneault I, Dartiguenave C, Bertrand MJ, Waldron KC. Glutaraldehyde: Behavior in aqueous solution, reaction with proteins, and application to enzyme crosslinking. *Biotechniques*. 2004;37(5):790-802. doi:10.2144/3705A0790.

104. Jamir L, Ali AR, Ghosh H, Chipem F a S, Patel BK. The thiocarbonyl “S” is softer than thiolate “S”: a catalyst-free one-pot synthesis of isothiocyanates in water. *Org Biomol Chem*. 2010;8(7):1674-1678. doi:10.1039/b923336a.

105. Arslan G, Özmen M, Gündüz B, Zhang X, Ersöz M. Surface modification of glass beads with an aminosilane monolayer. *Turkish J Chem*. 2006;30(2):203-210. doi:10.1016/j.jhazmat.2009.06.045.

106. Kim HL, Lee SB, Jeong HJ, Kim DW. Enhanced tumor targetability of PEGylated mesoporous silica nanoparticles on in vivo optical imaging according to their size. *RSC Adv*. 2014;4(59):31318-31322. doi:10.1039/c4ra03905j.

107. Oleylamine. 2018. http://www.chemspider.com/Chemical-Structure.4512354.html. Accessed July 1, 2018.

108. Ethylene Glycol. 2018. http://www.chemspider.com/Chemical-Structure.13835235.html. Accessed July 1, 2018.

109. Fluorescein (FITC). 2018. https://www.thermofisher.com/us/en/home/life-science/cell-analysis/fluorophores/fluorescein.html. Accessed January 7, 2018.

110. EVOS Light Cube Selection Guide for EVOS and Countess II FL Instruments. 2018. https://www.thermofisher.com/us/en/home/life-science/cell-analysis/cellular-imaging/cell-imaging-systems/evos-led-light-cubes/evos-dye-compatibility.html. Accessed January 5, 2018.

111. Chambers W, Fellers TJ, Davidson MW. Darkfield Illumination. https://www.microscopyu.com/techniques/stereomicroscopy/darkfield-illumination. Accessed January 5, 2018.

112. Vainrub A, Pustovyy O, Vodyanoy V. Resolution of 90 nm in an Optical Transmission Microscope with an Annular Condenser. *Opt Lett*. 2006;31(19):2855-2857.

113. Rhodamine B Isothiocyanate. 2018. https://www.sigmaaldrich.com/catalog/product/sigma/r1755?lang=en&region=US. Accessed July 1, 2018.

114. Becher P. *Encyclopedia of Emulsion Technology*. 4th ed. New York: Marcel Dekker, Inc.; 1996.

115. Chappat M. Some applications of emulsions. *Colloids Surfaces A Physicochem Eng Asp*. 1994;91(C):57-77. doi:10.1016/0927-7757(94)02976-8.

116. Bibette J, Leal-Calderon F. Surfactant-stabilized emulsions. *Curr Opin Colloid Interface Sci*. 1996;1(6):746-751. doi:10.1016/S1359-0294(96)80076-8.

117. Pichot R. Stability and Characterisation of Emulsions in the presence of Colloidal Particles and Surfactants. 2010;(November).

118. Sharma MK, Shah DO. Introduction to Macro- and Microemulsions. *Macro- and Microemulsions*. 1985;272:1-18. doi:10.1021/bk-1985-0272.

119. Ramsden W. Separation of Solids in the Surface-Layers of Solutions and "Suspensions" (Observations on Surface-Membranes, Bubbles, Emulsions, and Mechanical Coagulation). -- Preliminary Account. *Proc R Soc London*. 1903;72(477-486):156-164.

doi:10.1098/rspl.1903.0034.

120. Pickering SU. Emulsions. *J Chem Soc Trans*. 1907;127:2001-2021.

121. Yang Y, Fang Z, Chen X, et al. An overview of pickering emulsions: Solid-particle materials, classification, morphology, and applications. *Front Pharmacol*. 2017;8(MAY):1-20. doi:10.3389/fphar.2017.00287.

122. Jiang S, Chen Q, Tripathy M, Luijten E, Schweizer KS, Granick S. Janus Particle Synthesis, Self-Assembly. 2010:1060-1071. doi:10.1039/9781849735100.

123. Thompson KL, Armes SP, York DW. Preparation of pickering emulsions and colloidosomes with relatively narrow size distributions by stirred cell membrane emulsification. *Langmuir*. 2011;27(6):2357-2363. doi:10.1021/la104970w.

124. Priest C, Herminghaus S, Seemann R. Generation of monodisperse gel emulsions in a microfluidic device. *Appl Phys Lett*. 2006;88(2):1-3. doi:10.1063/1.2164393.

125. Tu F. Emulsion Stabilization with Janus Particles. 2015.

126. Tadros TF. *Emulsion Science and Technology: A General Introduction*. 1st ed. (Tadros TF, ed.). Weinheim: Wiley-VCH; 2009.

127. Chevalier Y, Bolzinger Ma-A. Emulsions stabilized with solid nanoparticles - Pickering emulsions. *Elsevier*. 2013:23-34.

128. Diisocyanates: Fast Facts and Figures. *Am Chem Counc*. 2018. https://dii.americanchemistry.com/. Accessed January 7, 2018.

129. Polyurethane. *Essent Chem Ind - Online*. 2016. http://www.essentialchemicalindustry.org/polymers/polyurethane.html. Accessed July 1, 2018.

130. Van Gheluwe P, Leroux J. Sequential nature of the exothermic reactions leading to the formation of flexible polyurethane foams. *J Appl Polym Sci*. 1983;28(6):2053-2067. doi:10.1002/app.1983.070280618.

131. 2 lb. Polyurethane Mix and Pour Foam. *Fibre Glas*. 2018. https://www.fibreglast.com/product/2_Lb_Polyurethane_Mix_and_Pour_Foam_24_25/Fo

am.

132. Wel IC, Rowley RL. Ternary Liquid Mixture Viscosities and Densities. *J Chem Eng Data*. 1984;29(3):336-340. doi:10.1021/je00037a033.

133. Polyurethane Applications. *Am Chem Counc*. 2005. https://polyurethane.americanchemistry.com/Applications/. Accessed July 1, 2018.

134. The Economic Benefits of Polyurethane. 2015;(September):1-16. https://polyurethane.americanchemistry.com/Full-Report-Economic-Benefits-of-Polyurethane.pdf. Accessed July 1, 2018.

135. Polyurethane for Marine Applications. *Am Chem Counc*. 2005. https://polyurethane.americanchemistry.com/Polyurethane-for-Marine-Applications/. Accessed July 1, 2018.

136. Why Use Polyurethane Foam. 2018. https://www.generalplastics.com/why-polyurethane. Accessed July 1, 2018.

137. Kiparissides C, Shah SL. Self-tuning and stable adaptive control of a batch polymerization reactor. *Automatica*. 1983;19(3):225-235. doi:10.1016/0005-1098(83)90099-7.

138. Grace-Martin K. When Unequal Sample Sizes Are and Are NOT a Problem in ANOVA. 2018. https://www.theanalysisfactor.com/when-unequal-sample-sizes-are-and-are-not-a-problem-in-anova/. Accessed July 16, 2018.

139. Young's Modulus - Tensile and Yield Strength for Common Materials. *Eng ToolBox*. 2003. https://www.engineeringtoolbox.com/young-modulus-d_417.html. Accessed January 5, 2018.

140. Nielsen LF. Elasticity and Damping of Porous Materials and Impregnated Materials. 1983:1-6.

141. Advanced Porosity Analysis. 2018:1-17. http://umanitoba.ca/faculties/health_sciences/medicine/units/cacs/sam/media/MN011_Advanced_Porosity_Analysis.pdf. Accessed July 1, 2018.

142. Lawrence M, Jiang Y. *Bio-Aggregates Based Building Materials*. (Amziane S, Arnaud La,

eds.). Bath: Wiley; 2017. doi:10.1007/978-94-024-1031-0_2.

143. Pham BTT, Such CH, Hawkett BS. Synthesis of polymeric janus nanoparticles and their application in surfactant-free emulsion polymerizations. *Polym Chem*. 2015;6(3):426-435. doi:10.1039/C4PY01125B.

144. Fuji M, Fujimori H, Takei T, Watanabe T, Chikazawa M. Wettability of Glass-Bead Surface Modified by Trimethylchlorosilane. *J Phys Chem B*. 1998;102(51):10498-10504. doi:10.1021/jp981983d.

145. Chandler DL. Explained: Chemical Vapor Deposition. 2015. http://news.mit.edu/2015/explained-chemical-vapor-deposition-0619. Accessed January 5, 2018.

146. Principles of Ion Exchange Chromatography. 2018. https://www.separations.us.tosohbioscience.com/service--support/technical-support/resource-center/principles-of-chromagraphy/ion-exchange. Accessed January 5, 2018.

147. ZORBAX Ion Exchange. 2018. https://www.agilent.com/en/products/liquid-chromatography/lc-columns/biomolecule-separations/zorbax-ion-exchange. Accessed January 5, 2018.

148. Simunyu F. Animations. 2015. http://www.simunyubiomedvisuals.com/animations/. Accessed January 5, 2018.

149. Thermo-Fisher Scientific - LIVE/DEAD Cell Viability Assays. 2016.

150. Davis R, Deering A, Burgula Y, Mauer LJ, Reuhs BL. Differentiation of live, dead, and treated cells of E. coli O157:H7 using FT-IR spectroscopy. *J Appl Microbiol*. 2011. doi:10.1111/j.1365-2672.2011.05215.x.

151. Piao MJ, Kang KA, Lee IK, et al. Silver nanoparticles induce oxidative cell damage in human liver cells through inhibition of reduced glutathione and induction of mitochondria-involved apoptosis. *Toxicol Lett*. 2011;201(1):92-100. doi:10.1016/j.toxlet.2010.12.010.

152. Ahamed M, AlSalhi MS, Siddiqui MKJ. Silver nanoparticle applications and human health. *Clin Chim Acta*. 2010;411(23-24):1841-1848. doi:10.1016/j.cca.2010.08.016.

153. Roe D, Karandikar B, Bonn-Savage N, Gibbins B, Roullet J baptiste. Antimicrobial surface functionalization of plastic catheters by silver nanoparticles. *J Antimicrob Chemother*. 2008;61(4):869-876. doi:10.1093/jac/dkn034.

154. Kim JS, Kuk E, Yu KN, et al. Antimicrobial effects of silver nanoparticles. *Nanomedicine Nanotechnology, Biol Med*. 2007;3(1):95-101. doi:10.1016/j.nano.2006.12.001.

155. Scaling up step by step. 2012. http://www.zeton.com/site/pdf_articles/Zeton_Scaling_Up.pdf. Accessed January 5, 2018.

156. Zlokarnik M. *Scale-up in Chemical Engineering*. 2nd ed. Wiley-VCH; 2003.

157. Petrin EM. Email Conversation with NanoComposix. 2018.

158. Frequently Asked Questions. 2018. https://nanocomposix.com/pages/frequently-asked-questions. Accessed January 5, 2018.

159. Pharmaceutical Process Scale-Up and Technology Trasnfer. 2016. https://www.quadro.com/blog/pharmaceutical-process-scale-and-technology-transfer/. Accessed January 5, 2018.